1994

Physical Factors Influencing The Quality Of Megavoltage Radiographs

David Anthony Jaffray

Physical Factors Influencing the Quality of Megavoltage Radiographs

by

David Anthony Jaffray

Department of Medical Biophysics

Submitted in partial fulfilment
of the requirements for the degree of
Doctor of Philosophy

Faculty of Graduate Studies
The University of Western Ontario
London, Ontario
December 1993

ISBN 0-315-90558-1

ABSTRACT

It has been recognized that improved methods of verifying radiation field placement in external beam radiotherapy are required in order to make frequent checks of field placement feasible. As a result, a large number of electronic portal imaging systems have been developed as possible replacements for film. These developments have produced digital systems with faster acquisition and display (few seconds), but the quality of the images acquired with such systems is still disappointing. The reasons for this are not well known, possibly because relatively few studies of the fundamental physics of imaging at megavoltage energies have been made.

This thesis examines many of the fundamental factors which limit the quality of radiographs obtained with a megavoltage radiotherapy beam. The size and shape of the radiation sources in ten radiotherapy machines were measured using a CT reconstruction technique. A novel technique was also developed to measure the extra-focal source in medical linear accelerators. It was found that the focal spots of modern medical linear accelerators should not influence significantly image quality if reasonable radiographic magnifications (1.2-1.4) are used. The extra-focal source measurements demonstrate that the x-ray source of a medical linear accelerator is composed of two components: a small focal spot surrounded by a large extra-focal component. While the extra-focal source does not influence significantly image quality, it does have important implications for radiotherapy dosimetry. In addition, a detailed Monte Carlo simulation of x-ray interactions within the patient determined that a significant fraction of the x-ray scatter generated in the patient is due to bremsstrahlung and positron annihilation and that the scatter fractions found in megavoltage imaging are lower (0.3-0.5) than those found in diagnostic imaging

(0.8-0.9). The impact of the scatter fluence on the contrast and the signal-to-noise characteristics of a therapy image is presented for a variety of therapy imaging detectors. Finally, the interaction of x-rays within typical fluoroscopic imaging detectors (metal plate/phosphor screen) is examined using Monte Carlo techniques. This study shows that failure to include electron transport in determining the quantum absorption efficiency of metal plate/phosphor detectors can lead to gross(factor of 2) inaccuracies. In addition, our study demonstrates that x-ray absorption noise at megavoltage energies can reduce the detective quantum efficiency of these detectors by a factor of 2.

ACKNOWLEDGEMENTS

I wish to acknowledge the many people who have influenced me during my Ph.D. studies.

First of all, I would like to thank the members of my advisory committee, Drs. Jerry Battista, Peter Munro, Aaron Fenster, and Trevor Cradduck. I thank Jerry for getting me involved in this field over seven years ago, and for his constant support, guidance and encouragement. I thank Peter for teaching me to be thorough and 'pithy'. I hope that I can develop the attention to detail and completeness that you have demonstrated.

To my fellow students in the physics labs at the London Regional Cancer Centre, thanks for making it fun. In chronological order, Darcy Mason, Mike Sharpe, Joanne Moseley, Miller Macpherson, Crystal Plume, Daryoush Sheikh-Bagheri, John MacLellan, Jean-Pierre Bissonnette, Steve Sawchuk, Steven Breen, and Rob Meeder. An Angelo's cookie will always mean a lot.

To my friends in the Department of Medical Biophysics, with whom I have spent a lot of good times during the five and one-half years of my Ph.D. studies.

To my parents and family for their endless support, love and guidance.

And finally, I would like to thank Stasia, for her patience, her support, and her laughter.

The financial support of the Ontario Graduate Studentship Program, the Medical Research Council, and the London Regional Cancer Centre is greatly appreciated.

TABLE OF CONTENTS

LIST OF FIGURES

LIST OF TABLES

LIST OF APPENDICES

Chapter 1. INTRODUCTION

Cancer is one of the leading causes of death and a disease which reduces the quality of life in the elderly population of western society. Of the several treatment options for cancer, external beam radiotherapy is the most common method of controlling this disease. In western society, 50 - 60% of all patients treated for malignant cancers received external beam radiation treatments as their primary therapy.[1] In external beam radiotherapy, the goal is to deliver a specified dose of ionizing radiation to the tumourous region, while minimizing radiation-induced damage of the surrounding normal tissues.

1.1 External Beam Radiotherapy

The following typical procedures are used to plan and deliver external beam radiation therapy. Several days before treatment begins, the treatment is planned using a device known as a radiotherapy simulator (Fig. 1.1a). This device simulates the mechanical geometry of a radiotherapy treatment machine but has a diagnostic (rather than therapeutic) x-ray source. All modern radiation treatment machines (Fig. 1.1b) employ an isocentric geometry, where the x-ray source is mounted on a gantry which can be rotated 360° around the patient. The point of intersection between the central axis of the radiation beam and the gantry axis of rotation is known as the isocentre. Thus, by placing the tumour at the isocentre, the x-ray beam will always be directed towards the tumour regardless of the orientation of the gantry. Using the simulator, the radiation oncologist determines the gantry angles as well as the sizes and shapes of the radiation beams which maximize dose to the tumour region while minimizing dose to the surrounding normal tissues. Once the desired orientation of the gantry and position of the

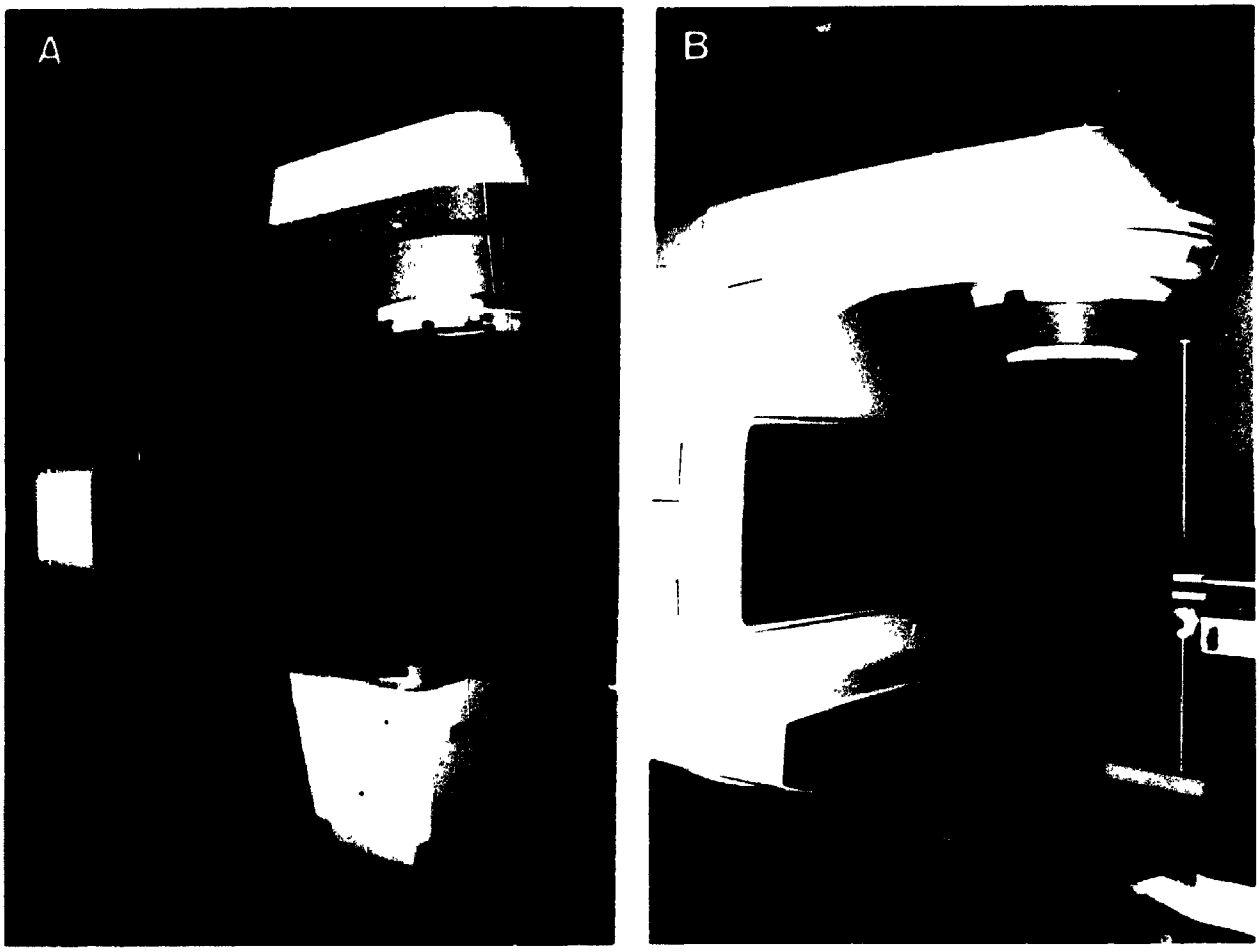

Figure 1.1 Photographs of (a) a Varian Ximatron radiotherapy simulator, and (b) a Varian Clinac 2100c medical linear accelerator. A portal film cassette and holder are also shown in (b).

patient are determined, diagnostic radiographs of the patient are taken and the sizes and shapes of the radiation beams are indicated on these films. These radiographs are referred to as 'simulator films' and they carry the geometric prescription to be used in positioning the radiation field(s) at the start of each treatment. Once the simulation is complete, marks are placed on the patients' skin which correspond to points illuminated by a set of orthogonally-oriented laser beams. The laser beams provide a reference

frame which is duplicated in the treatment room. In principle, aligning the marks on the patients' skin with the laser beams in the treatment room should ensure that the patient is properly positioned during each treatment.

The radiation dose delivered in an external beam radiotherapy treatment is typically fractionated into a large number (20-30) of daily irradiations (Fig. 1.2). To verify the placement of the radiation field for a given daily irradiation, a small fraction of the daily treatment dose can be used to form a radiograph of the patient using the treatment beam. These radiographs are referred to as portal, therapy, or localisation images/films. (A portal film cassette is shown in Fig. 1.1b; it is held just below the treatment couch by an articulating arm.) The portal image can then be compared to the simulator film to verify that the field placement complies with the prescribed geometry.

1.2 Geometric discrepancies in radiation therapy

Many studies have shown that accuracy of dose delivery in radiation therapy is crucial to the success of radiation treatments. Failure of some radiotherapy treatments

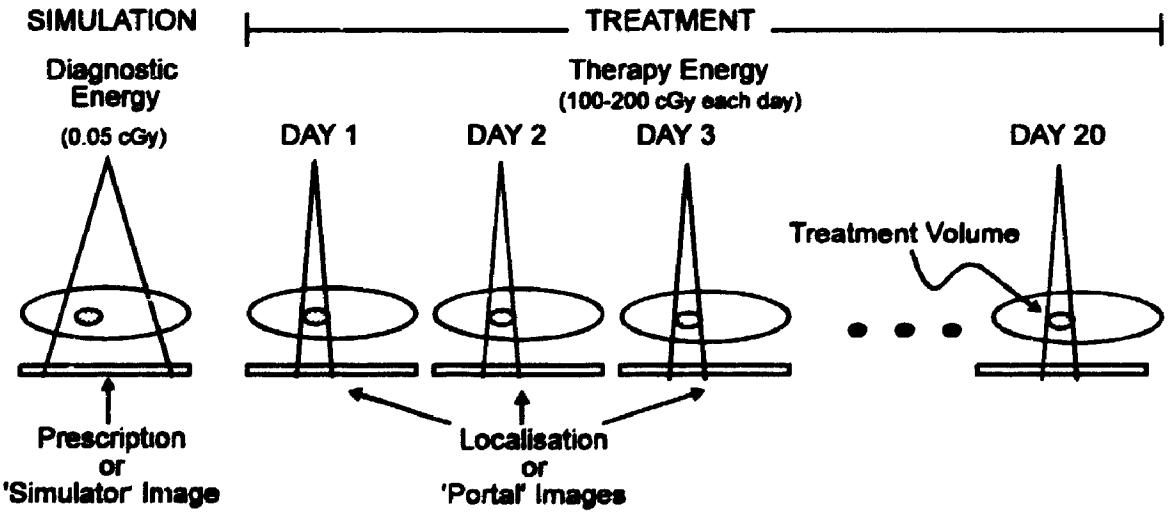

Figure 1.2 External beam radiotherapy treatment. The treatment is first simulated with diagnostic x-rays, the resulting image is then compared with the portal image acquired before each treatment

has been correlated with technical errors or inaccuracies in dose delivery.[2,3] Other studies of accidental misadministrations which occurred during radiation treatment have shown that clinical symptoms such as changes in local tumour control and normal tissue complication can be detected for dose variations of as little as 7 to 15%.[4,5,6] For this reason, a number of authors have recommended that dosimetric accuracy be maintained within 5%.[7] Maintaining this accuracy throughout the entire treatment volume requires that each factor contributing to the dose uncertainty has an accuracy of much better than 5%. Inaccuracies can arise from uncertainties in the absolute dose calibration, calculation of relative dose distribution, and ultimately, execution of the treatment (i.e., positioning of the patient so that the treatment beam irradiates only the prescribed volumes). [8,9,10,11,12]

Discrepancies in field placement arise from several sources,[13] such as, errors in beam settings (field size, collimator rotation), variability in shielding block placement,[14] use of patient skin markings as landmarks for the internal anatomy, and patient movement.[15] Furthermore, errors which result in discrepancies in field placement can be divided into three categories: mistakes, systematic errors and random errors. Mistakes are gross errors which are usually independent of patient position. For example, these include incorrect field size settings or use of an incorrect beam accessory. Systematic and random errors usually refer to discrepancies in patient positioning. Those errors which occur consistently are systematic errors; these are attributed to mechanical offsets between the simulator and treatment geometries, or a preferred patient position during setup, possibly due to patient discomfort. On the other hand, random errors vary inconsistently from treatment setup to treatment setup; these errors result from a variety sources - including, for example, daily variations in patient weight or fluctuations in the placement of a shielding block. The magnitude, frequency of occurrence, and impact of

field placement discrepancies has been examined by number of investigators.

Studies using portal films have shown that discrepancies in radiation field placement can be quite large (> 5 mm) and that they occur frequently. Marks et al. have reported that 36% of the treatments studied in their investigation of extended mantle (thoracic) field placement had significant localisation errors (i.e. sufficient to exclude known or expected sites of disease from the treatment volume).[16] Rabinowitz et al. compared simulator and portal films for 71 patients to determine the magnitude of inter-treatment and simulator-to-treatment variations.[3] They reported the deviations in the inter-treatment variation to be distributed normally with an average deviation of 3 mm. The discrepancies between the simulator and portal films were greater and depended on the treatment site, yielding a worst-case discrepancy of 7.7 mm averaged over all sites. The smallest discrepancy corresponded to head and neck irradiations (3.5 mm) and the largest to the thoracic irradiations (9.2 mm). Huizenga et al. have performed a similar study of 22 patients.[17] They found the average discrepancies in field edge placement between simulator and portal films to be 5 mm, with a standard deviation of 5 mm. In addition, most of these discrepancies were determined to be the result of field *placement* as opposed to gross errors in field *size or shape*. Dunscombe et al. demonstrated that for immobilized head and neck treatments, shifts between the geometric prescription and the delivered geometry were as large as 8.9 mm (95 percentile) with a median of approximately 4.4 mm. Furthermore, they demonstrated that the majority of shifting occurred between the patient and the immobilization shell, as opposed to shifting between the radiation beam and the immobilization shell.[18] In addition, a study by Griffiths et al. of complex fields (head and thorax) in 19 patients showed it necessary to correct 21% of the initial field setups. In their study, the decision to correct field placement was made

when the treatment volume was incorrectly shielded by a margin of 1 cm or larger.[19] Finally, in a study of 35 patients, Kihlen et al. reported that the average standard deviation between the prescription and treatment field was 3.5 mm, despite the use of laser alignment and good patient immobilization.[20]

Several authors have shown that the occurrence of these discrepancies can alter the outcome of treatment. Marks et al.[16] have correlated local recurrence of Hodgkin's disease or malignant lymphoma in specific patients with field placement discrepancies in the axillae. Two of the patients in their study had enough documented discrepancies at the site of recurrence to cause a dose reduction sufficient to explain the recurrence. Kinzie et al.[21] report on 155 patients treated for Hodgkin's disease in their *Patterns of Care* study. They found an overall relapse rate of 54% for patients with inadequate field margins. Furthermore, a third of the relapses were due to a recurrence within the field or near to the field margins. For patients with adequate margins, the overall relapse rate dropped significantly from 54% to 14% (1/4) and the in-field or marginal rate decreased from 33% to 7% (1/5). In a more recent study, Perez et al.[22] reported on factors influencing local tumour control and long term survival for 738 patients treated for cancer of the prostate between 1967 and 1988. It was found that the actuarial 5-year local tumour failure rates were 0% for Stage A2, 18% for Stage B, and 20% for Stage C when the inferior field margin was at or inferior to the ischial tuberosity, compared to failure rates of 60% for Stage A2, 27% for Stage B and 38% for Stage C when the inferior margin was superior to the ischial tuberosity. However, the increase from 20% to 38% for Stage C was the only stage with a large enough population to prove statistical significance.

Fortunately, it has been shown that frequent monitoring of the treatment field position allows intervention and reduces the magnitude of the field placement

discrepancies. Marks et al. demonstrated a reduction in the incidence of localization errors from 50% to 29% over a two year period and attributed it to technical refinements and more frequent use of localization films.[23] Furthermore, they suggest that the required frequency of verifying field placement depends on the treatment site and field margins, with complex fields to be monitored more frequently. Griffiths et al. also recommend frequent monitoring of treatment fields, particularly over the first few treatments.[24] They argue that large systematic errors introduced by transferring patients from the simulator to the treatment machine can be corrected by frequent monitoring during the first few treatment sessions. The remaining random variations are shown to be less significant, requiring less frequent checks. Ezz et al. report the early use of a prototype 'on-line' portal imaging system for verifying radiation field placement.[25] In a pilot study of five patients, it was deemed necessary to correct the initial patient setup in 60% of the fields. A retrospective comparison between the initial and adjusted field position revealed an improvement in the accuracy of field placement, after correction of patients' position.

Unfortunately, radiation field placement is not verified frequently in the clinical setting.[26] Studies indicate that portal films are used to check field placement much less frequently than is considered desirable. This is due to a number of factors: (i) the use of film is time consuming and labour intensive and can reduce throughput in a busy radiation therapy department; (ii) quantitative interpretation of geometric discrepancies is difficult and tedious with a non-digital imaging system,[3] and finally, (iii) the fixed display contrast of film makes detection of low-contrast bony landmarks difficult, resulting in most portal films having unsatisfactory image quality.[27] This last factor is one of the major reasons why portal films are used infrequently. As an example of how poor image quality can be at therapy energies, images acquired from a simulator (100 kVp, diagnostic x-ray source)

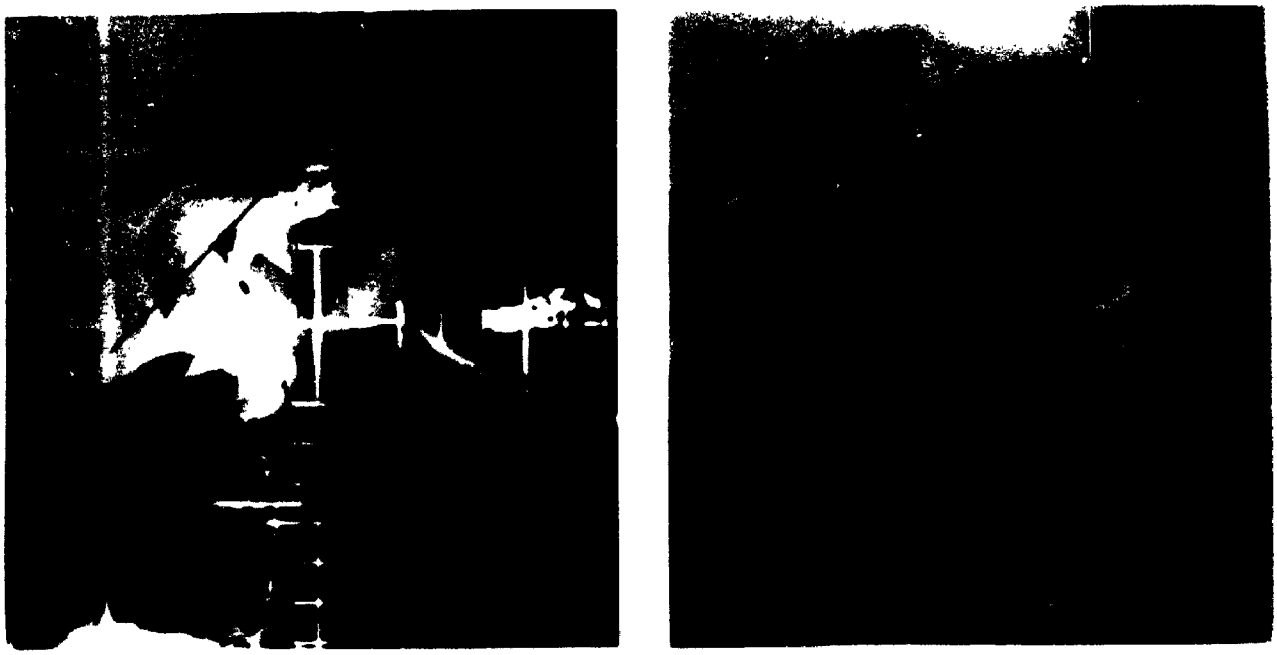

Figure 1.3 Comparison of radiographs taken on (a) a simulator (100 kVp) and (b) a medical linear accelerator (6 MV). The images are of the same patient (site: lateral head).

and a medical linear accelerator (6 MV, therapy x-ray source) are shown in Fig. 1.3a and 1.3b, respectively. Clearly, even though the same region of the patient has been imaged, the anatomic features are much more difficult to visualize in the portal image (Fig. 1.3b).

1.3 X-ray energy and image quality

The formalism of Motz and Danos[28] can be used to explore why image quality decreases as the energy of the x-ray beam increases. Figure 1.4 shows the radiographic imaging task used in the Motz and Danos formalism - the detection of a small anatomical feature (e.g. bone) embedded within a homogeneous phantom (water). Using this simple model, we can define two quantities which give a measure of image quality; contrast and signal-to-noise.

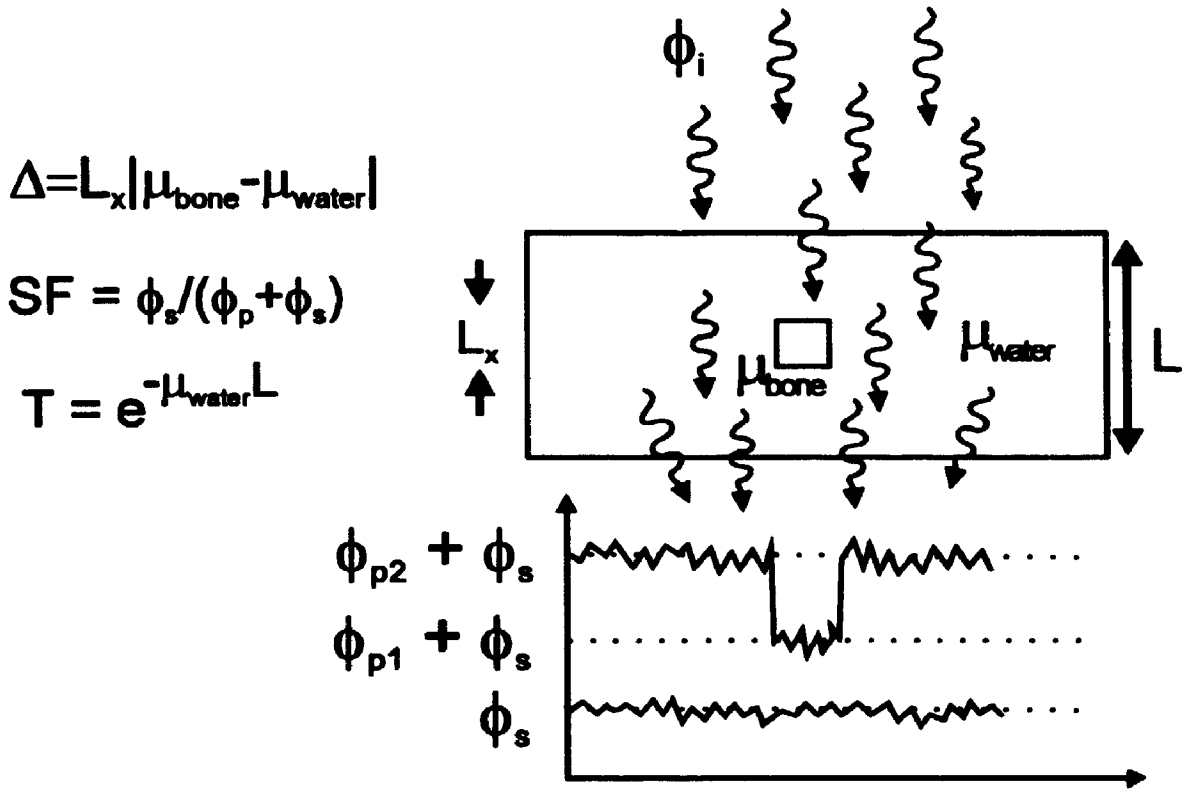

Figure 1.4 Simple model of an imaging task, the detection of a bone (L_x, μ_{bone}) in a water phantom (L, μ_{water}). (see text for symbols)

1.3.1 Contrast

Contrast, C, describes how much an object stands out from its surroundings and is defined as[28]

$$C = \frac{signal}{mean\ signal} = \frac{\phi_{p2}-\phi_{p1}}{(\phi_{p2}+\phi_{p1}+2\cdot\phi_s)/2}, \qquad (1.1)$$

where ϕ_{p1}, ϕ_{p2}, and ϕ_s are the primary and scatter photon fluences reaching the image receptor (Fig. 1.4). Motz and Danos have shown that this expression can be re-written as[28]

$$C = \frac{2(1 - e^{-\Delta})}{1 + e^{-\Delta} + \frac{2 \cdot SF}{1 - SF}}, \qquad (1.2)$$

where: Δ is the difference in attenuation between the object and the background (i.e. $\Delta = L_x|\mu_{bone} - \mu_{water}|$), μ_{bone} and μ_{water} are the x-ray attenuation coefficients for bone and water, respectively, L_x is the thickness of the anatomic structure, and SF is the scatter fraction [$SF = \phi_s/(\phi_s + \phi_p)$]. Equation 1.1 shows that the contrast is increased by increasing the difference in attenuation along the x-ray path and is decreased by the addition of a scatter fluence.

Figure 1.5a shows the subject contrast of 1 cm thick bone or air objects embedded within 20 cm of water as a function of x-ray energy. For simplicity, the contrast has been calculated assuming that no x-ray scatter occurs (i.e., SF = 0). The attenuation coefficients used in these calculations were taken from the XCOM computer program[29] and are shown in Fig. 1.6(a & b). The x-ray energy spectra used to generate the simulator image (100 kVp, diagnostic energy)[30] and that used to generate the portal image (6 MV, therapy energy)[31] are shown in Fig. 1.5c. The mean energy of these two spectra are approximately 50 keV and 2 MeV, respectively.

Examining the subject contrast at these two x-ray energies shows the subject contrast decreases from 0.5 to 0.037 (a factor of 13) for the bone and from 0.2 to 0.05 for the air pocket (only a factor of 4). This explains the enhanced visibility of the air passages seen in the therapy image (Fig. 1.3b) as compared to the simulator image.

Contrast is the result of differences in x-ray attenuation within the patient. At low energies, the photoelectric process dominates (Fig. 1.6). Since the photoelectric cross-

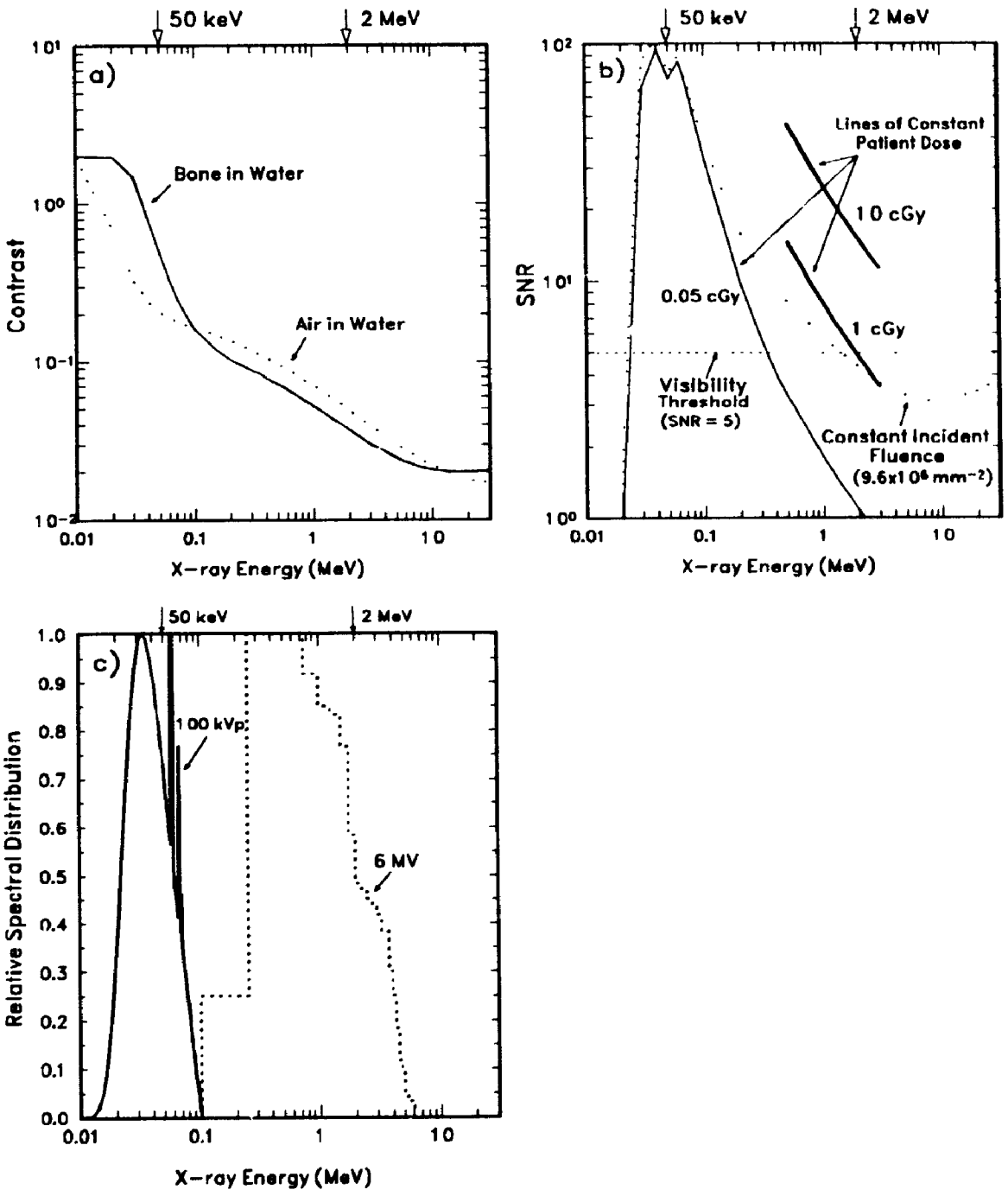

Figure 1.5 (a) Contrast and (b) SNR vs x-ray energy for a 1cm bone embedded within 20cm of water (c) Typical diagnostic (100kVp, 50keV mean) and therapeutic (6MV, 2MeV mean) x-ray energy spectra.

section is proportional to the atomic number raised to the third power (Z^3), the higher atomic number of bone results in a larger attenuation coefficient compared to that of water. However, the photoelectric cross-section is also inversely proportional to the energy cubed ($1/E^3$). Therefore, at higher energies(>100keV), Compton scattering becomes the dominant interaction process. The Compton scattering cross-section is dependent on the electron density of a material, which, except for hydrogen, varies only slightly with atomic number. The electron density of water (ρ_e(water) = 3.34×10^{23} e/cm^3) is comparable to that of bone (ρ_e(bone) = 5.81×10^{23} e/cm^3) (less than a factor of 2 difference).[32] Therefore, the difference in attenuation, and hence the contrast, reduces significantly at megavoltage energies.

1.3.2 Signal-to-Noise Ratio

The production and detection of x rays is a stochastic process and as a result, there is an inherent variation or uncertainty in the number of x rays that interact with a detector. Therefore, the detected fluences shown in Fig. 1.4 have some uncertainty; this is represented by the fluctuations in the fluence profiles. It can be shown that the number of x-ray quanta detected in some time interval follows Poisson counting statistics. For a Poisson process, the variance in the number of detected x-ray quanta is equal to the mean. Therefore, if the mean fluences are known, a signal-to-noise ratio can be calculated. The signal-to-noise ratio of the bone signal shown in Fig. 1.4 is calculated as

$$SNR = \frac{\textit{image signal}}{\textit{noise}} = \frac{\Phi_{p2} - \Phi_{p1}}{\sqrt{\Phi_{p1} + \Phi_{p2} + 2 \cdot \Phi_s}}. \qquad (1.3)$$

Rewriting in terms of the geometry shown in Fig. 1.4, we obtain[28]

$$SNR = A \cdot \phi_i \cdot T \cdot \eta \frac{1 - e^{-\Delta}}{\sqrt{1 + e^{-\Delta} + \frac{2 \cdot SF}{1 - SF}}}, \qquad (1.4)$$

where: A is the area of the detector element, ϕ_i is the incident fluence, T is the patient transmission, and η is the detector efficiency of the x-ray detector. For the calculations presented here, we assumed the area of the detector element to be 1 mm x 1 mm, the patient transmission was calculated assuming water only (i.e. $T = e^{-\mu_{water} L}$), the detection efficiency of the detector ($N_{detected}/N_{incident}$) was calculated for each x-ray energy assuming a 0.5 mm thick gadolinium oxysulfide phosphor ($\rho_{phosphor\ with\ binder} = 3.67\ g/cm^3$) layer, and the scatter fraction was assumed to be zero. The attenuation coefficients for the gadolinium oxysulfide were also taken from the XCOM program.[29] Realistic estimates of the incident fluence, ϕ_i, were calculated using Rogers' fluence-to-maximal dose equivalence conversion tables (see Table 1.1).[33]

The SNR is influenced by many factors. Equation 1.4 shows that the SNR, like the contrast, decreases as the difference in attenuation between the object and the background (Δ) decreases, however, unlike the contrast, the SNR is proportional to the number of x-rays detected ($A \phi_i T \eta$ = the area X fluence X transmission X collection efficiency = number of detected x-rays). In addition, scatter reduces the SNR by adding noise without contributing to the signal.

Using Eq. 1.4, we have plotted the SNR versus x-ray energy for an image of a 1 cm thick bone structure acquired using an incident x-ray fluence of $9.6 \times 10^6\ mm^{-2}$ (dotted

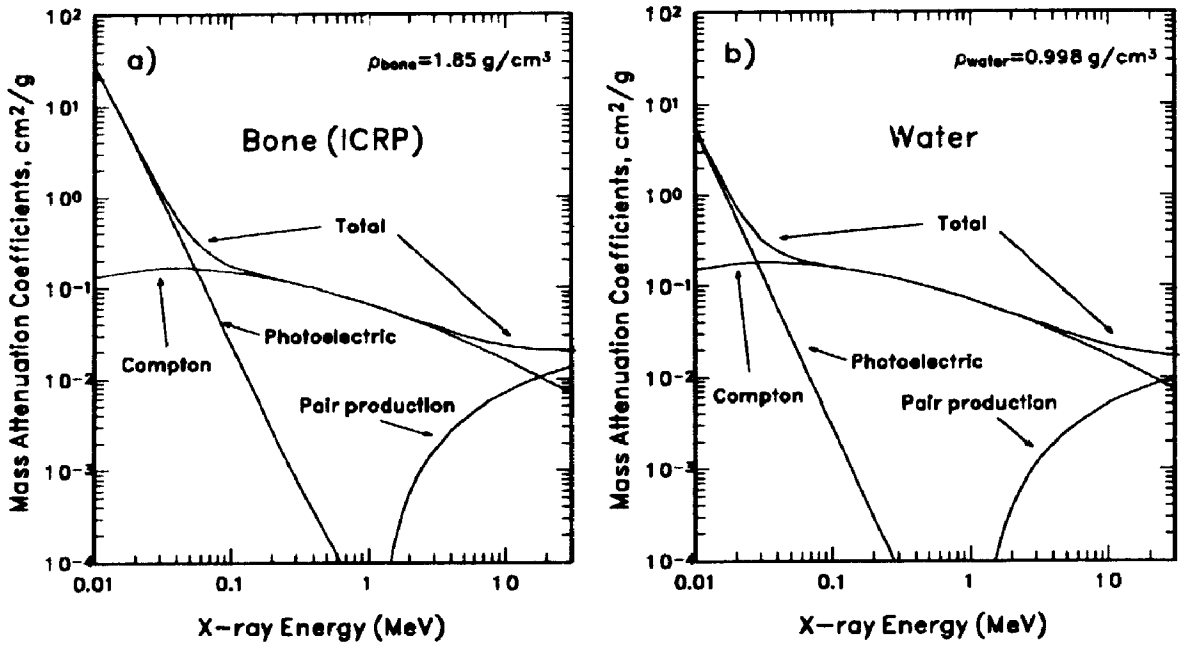

Figure 1.6 The mass attenuation coefficients for bone and water. At diagnostic energies (< 100 keV), photoelectric absorption dominates. At megavoltage energies, Compton scattering dominates.

line in Fig. 1.5b). This is the incident fluence used in a typical diagnostic energy (100 kVp) imaging procedure which delivers 0.05 cGy (50 mR) of dose to the patient (assuming a mean energy of 50 keV). Maintaining a fixed incident photon fluence (9.6×10^6 mm^{-2}) results in a rapid decrease in the SNR with increasing x-ray energy. Clearly, if the same number of quanta are used at 2 MeV as are used at 50 keV, the SNR would be below the visibility threshold recommended by Rose (SNR=5),[28] making it impossible to detect the structures seen at diagnostic energies. In addition to plotting the SNR for a fixed *incident fluence*, we have also plotted the SNR for a fixed *patient dose*. Figure 1.5b (solid lines) shows the SNR versus incident x-ray energy for three different fixed doses: a typical diagnostic imaging dose (0.05 cGy), a low therapy imaging dose (1 cGy), and a typical therapy imaging dose (10 cGy) (see Table 1.1). For a fixed patient dose of 0.05 cGy, the reduction in contrast and detector collection efficiency with increasing x-ray energy makes it impossible to maintain an acceptable SNR at megavoltage energies. As shown in Fig.

1.5b, the SNR falls below the visibility threshold[28] at x-ray energies greater than 300 keV. However, the much higher doses used in therapy imaging (1-10 cGy) produce SNRs which are comparable to that found at diagnostic energies. Table 1.2 shows the SNRs extracted from Fig. 1.7b for 50 keV and 2 MeV monoenergetic x-ray beams.

From Fig. 1.5 it is clear that a much larger patient dose must be delivered in therapy imaging to achieve the same SNR as is found at diagnostic energies. Fortunately, in therapy imaging, a large dose of 1-10 cGy is a small fraction of the daily treatment dose (100-200 cGy) delivered to the patient. However, even allowing these high doses, the SNR of a therapy image is poorer (by a factor of 5) than that found at diagnostic energies. It should be recognized that this estimate of SNR is based on *primary x-ray quantum noise only* and does not include other sources of noise, which will further degrade the SNR.

In summary, this simple model has revealed that subject contrast decreases with increasing x-ray energy. Not only does the contrast of objects decrease, the rate of

	Estimates of Incident Fluence, ϕ_i		
	Diagnostic Energy (50 keV)	Therapeutic Energy (2 MeV)	
Dose	0.05 cGy	1 cGy	10 cGy
Fluence (photons/mm^2)	9.6×10^6	0.115×10^9	1.15×10^9

Table 1.1 Comparison of x-ray fluences in diagnostic and megavoltage imaging for typical patient doses Fluence determined from Rogers' fluence to dose conversion tables

	Estimates of SNR for Typical Patient Doses at Diagnostic and Therapeutic X-ray Energies			
	Diagnostic Energy (50 keV)	Therapeutic Energy (2 MeV)		
Patient Dose	0.05 cGy (50 mR)	1 cGy	10 cGy	55 cGy
SNR	71	4.8	15	35

Table 1.2 Estimates of the SNR for diagnostic and therapy imaging exposures. The model assumed no x-ray scatter and a 0.5 mm thick photon counting detector. Cross-sections were taken from XCOM.

decrease depends on the effective atomic number of the object. This results in the contrast of air passages exceeding that of bony anatomy when x-ray energy exceeds 100 keV. Furthermore, the SNR of the bone signal decreases rapidly with increasing energy. For the same dose to the patient, the SNR is 100 times lower at megavoltage energies (2 MeV) than that at diagnostic energies (50 keV). However, for typical diagnostic and therapy doses (D_d = 0.05 cGy and D_T = 10 cGy) the SNRs are more comparable, the SNR is only 5 times lower at megavoltage energies.

1.3.3 Spatial Resolution

Another important factor that influences image quality, but which is not included in the model described above, is spatial resolution. Spatial resolution is a measure of how the image signal is blurred by the imaging system. For example, the spatial resolution of the system influences how well edges, such as those resulting from bones, will be detected. Several factors can degrade the spatial resolution of an imaging system, such as improper focusing of a camera lens, a large x-ray source size, the scattering of light within a phosphor screen, or, energy-dependent effects, such as the lateral spread of x-

ray energy deposited in a phosphor screen.[34] The spatial resolution of an imaging system is often characterized by examining how well the system reproduces a point object (infinitesimally small). Acquiring an image of such a point object measures the system's point spread function. Conventionally, this spread of signal is represented in the form of the modulation transfer function (MTF). The MTF describes how well the system passes different spatial frequencies and is calculated from the Fourier transform of the point spread function. While these concepts have not been included in our simple model, they can have a significant impact on image quality. Therefore, any complete characterization of an imaging system requires an examination of both the signal-to-noise characteristics and the spatial frequency response of the system.

1.4 Summary

Studies have shown that geometric discrepancies in radiation field placement occur frequently, influence the outcome of treatment, and can be reduced by frequent checks of field placement. However, checks of field placement are not being done as frequently as is desirable. This is largely because the current practice of using portal films to verify field placement has a number of drawbacks. The use of film is time consuming, its fixed display contrast makes detection of low contrast structures difficult, and the non-digital format makes quantification of geometric discrepancies challenging. As a result, a large number of electronic portal imaging systems have been examined as possible replacements for film.[35] These developments have produced digital systems with faster acquisition and display (few seconds), but the quality of the images acquired with currently available systems is still disappointing.[36] The reasons for this are not well known, possibly because relatively few studies of the fundamental physics of imaging at megavoltage

energies have been made. Investigators continue to strive for technical improvements in image quality without knowing what can theoretically be achieved with a megavoltage x-ray beam. *This thesis examines many of the fundamental factors which limit the quality of transmission radiographs that can be obtained when imaging with a megavoltage radiotherapy beam.*

1.5 Thesis Overview

The goal of this thesis research is to determine the causes of the dramatic reduction in image quality at megavoltage energies (Fig. 1.3). The simple model presented in the introduction ignores the influences of x-ray source size, x-ray scatter, and x-ray absorption noise. In this thesis, we analyze fully the magnitude of these effects at megavoltage energies and assess their impact on image quality. The material is presented in a logical sequence of (a) x-ray *source*, (b) x-ray scattering in the *patient*, and (c) the interaction of x-rays within the imaging *detector*.

A CT reconstruction technique was used to measure the size and shape of the high-energy radiation sources in radiotherapy treatment machines. We first measured the size and shape of the radioactive gamma source in a ^{60}Co treatment machine (chapter 2), and subsequently, measured the x-ray focal spots produced in nine different medical linear accelerators (chapter 3). In addition, chapter 3 presents a novel method of measuring the spatial distribution of *extra-focal* radiation emitted from a medical linear accelerator. The influence of these radiation sources (focal and extra-focal) on the spatial resolution of therapy images has been determined. In chapter 4, we present a detailed Monte Carlo simulation of x-ray interactions within the patient, determining the physical characteristics of the scattered radiation reaching the imaging detector. The physical processes responsible for the scattered radiation, the energy distribution of the scatter fluence, and the dependence of this fluence on imaging geometry are examined. In addition, the impact of the scatter fluence on the contrast and the signal-to-noise chara teristics of a therapy image are investigated for a variety of therapy imaging detectors. Chapter 5 examines the interaction of x-rays within typical fluoroscopic imaging detectors (metal

plate/phosphor screen) using Monte Carlo techniques. This study examines the quantum absorption efficiency at diagnostic and megavoltage energies and also examines how statistical variations in x-ray energy absorption degrade image quality. Chapter 6 contains a summary of our results, introduces a new model which may account for some of the reduction in spatial resolution seen in therapy images, and examines possible courses for further study.

Chapter 2 was published in Med. Phys. **18**(2), 288-291 (1991) under the title of "Activity distribution of a cobalt-60 teletherapy source" by D.A. Jaffray, P. Munro, A. Fenster and J.J. Battista; Chapter 3 was published in Med. Phys. **20**(5), 1417-1427 (1993) under the title of "X-ray sources of medical linear accelerators: focal and extra-focal radiation" by D.A. Jaffray, J.J. Battista, A. Fenster and P. Munro; Chapter 4 is *in press* for publication in Medical Physics under the title of "X-ray scatter in megavoltage transmission radiography: physical characteristics and influence on image quality" by D.A. Jaffray, J.J. Battista, A. Fenster and P. Munro; Chapter 5 is to be submitted to Medical Physics under the title of "Monte Carlo studies of x-ray energy absorption and quantum noise in megavoltage transmission radiography" by D.A. Jaffray, J.J. Battista, A. Fenster and P. Munro. All the authors participated in the conceptual development and planning of the work presented in this thesis. The experimental and theoretical work was performed by D.A. Jaffray, with the exception of some previously published measurements made by P. Munro which were included for comparison purposes in Chapter 3.

References

1 C.A. Perez and L.W. Brady, *Principle and practice of radiation oncology*, (JP Liddicoat, Philidelphia, 1987)

2 C.A. Perez, S. Breaux, H. Madoc-Jones, H.M. Camel, J. Purdy, S. Sharma, and W.E. Powers, "Correlation between radiation dose and tumor recurrence and complications in carcinoma of the uterine cervix: stages I and IIA," Int. J. Radiat. Oncol. Biol. Phys., **5**, 373-382 (1979)

3 Ian Rabinowitz, J. Broomberg, M. Goitien, K. McCarthy, and J. Leong, "Accuracy of Radiation Field Alignment in Clinical Practice," Int. J. Radiat. Oncol. Biol. Phys., **11**, 1857-1867 (1985).

4 M. Goitien and Joel Busse, "Immobilization Error: Some Theoretical Considerations," Radiology, **117**, 407-412 (1975).

5 A. Dutreix, "When and how can we improve precision in radiotherapy?," Radiotherapy Oncol. **2**, 275-292 (1984)

6 D.F. Herring and D.M.J. Compton, "The degree of precision required in the radiation dose delivered in radiotherapy," In: Computers in Radiotherapy, Brit. J. Radiol. Special Report No. 5, A.S. Glickman, M. Cohen, and J.R. Cunningham, Eds., (British Journal of Radiology, London, 1971). pp. 51-58

7 International Commission on Radiation Units and Measurements, **24**, 45-50, (1976)

8 G.K. Svensson, "Quality assurance in radiation therapy: physics efforts," Int. J. Radiat. Oncol. Biol. Phys., **10**, Sup. 1, 23-29 (1984)

9 D.F. Herring, "The consequences of dose response curves for tumor control and normal tissue injury on the precision necessary in patient management," Laryngoscope, Vol. LXXXV, **7**, 1112-1118 (1975)

10 R.M. Harrison, "External beam treatment planning - can we deliver what we plan?," Acta Oncologica, **32**, 445-451 (1993).

11 Mijnheer, B.J., Battermann, J.J, Wambersie, A., "What degree of accuracy is required and can be achieved in photon and neutron therapy?," Radiotherapy Oncol., **18**, 237-252 (1987)

12 A. Brahme, "Dosimetric precision requirements in radiation therapy," Acta Radiologica Oncology, **23**, 379-391 (1984).

13 F.R. Hendrickson, "The four p's of human error in treatment delivery," Int J. Radiation Oncology Biol. Phys., **4**, 913-914 (1978)

14 P.Rodrigus, D. Van den Weyngaert and W. Van den Bogaert, "The value of treatment portal films in radiotherapy for bronchial carcinoma," Radiotherapy and Oncology, **9**, 27-31 (1987)

15 S. Griffiths, "Hit or Miss - Is Perfection Achievable in Radiotherapy?," Radiography Today, **55**, No 620 (1989).

16 J.E. Marks, A.G. Haus, H.G. Sutton, and M.L. Griem, "Localization error in the radiotherapy of Hodgkin's disease and malignant lymphoma with extended mantle fields," Cancer, **34**, 83-90 (1974)

17 H. Huizenga, P.C. Levendag, P.M.Z.R De Porre, and A.G. Visser, "Accuracy in radiation field alignment in head and neck cancer: A prospective study," Radiotherapy and Oncology, **11**, 181-187 (1988)

18 P.B. Dunscombe, D.K. Fox, S. Loose, and K. Leszczynski, "The investigation and rectification of field placement errors in the delivery of complex head and neck fields," Int. J. Radiat. Oncol. Biol. Phys., **26**, 155-161 (1993)

19 S.E. Griffiths and R.G. Pearcey, "The daily reproduciblity of large, complex-shaped radiotherapy fields to the thorax and neck," Clinical Radiology, **37**, 39-41 (1986)

20 B. Kihlen and B.I. Ruden, "Reproducibility of field alignment in radiation therapy - a large scale clincal experience," Acta Oncologica, **28**, 689-692 (1989)

21 J.J. Kinzie, G. Hanks, C.J. Maclean, and S. Kramer, "Patterns of Care Study: Hodgkin's Disease Relapse Rates and Adequacy of Portals," Cancer **52**, 2223-2226 (1983).

22 C.A. Perez, H.K. Lee, A. Georgiou, M.D. Logsdon, P.P. Lai, and M.A. Lockett, "Technical and tumor-related factors affecting outcome of definitive irradiation for localized carcinoma of the prostate," Int. J. Radiat. Oncol. Biol. Phys., **26**, 581-591 (1993)

23 J.E. Marks, A.G. Haus, H.G. Sutton, and M.L. Griem, "The value of frequent treatment verification in reducing localization error in the irradiation of complex fields," Cancer, **37**, 2755-2761 (1976)

24 S.E. Griffiths, R.G. Pearcey, and J. Thorcgood, "Quality control in radiotherapy: The reduction of field placement errors," Int. J. Radiat. Oncol. Biol. Phys., **13**, 1583-1588 (1987)

25 A. Ezz, P. Munro, A.T. Porter, J. Battista, D.A. Jaffray, A. Fenster, and S. Osborne, "Daily monitoring and correction of field placement using a video-based portal imaging system: a pilot study," Int. J. Radiat. Oncol. Biol. Phys., **22**, 159-165 (1991)

26 *Radiotherapy Portal Image Quality*, AAPM Report No. 24 (TG28), ISBN# 0-88318-557-1 (1987)

27 L.E. Reinstein, M. Durham, M.Tefft, A. Yu, and A.S. Glicksman, "Portal film quality: A multiple institutional study," Med. Phys, **11**(4), 555-557 (1984)

28 J.W. Motz and M. Danos, "Image information content and patient exposure," Med. Phys., **5**(1), 8-22 (1978)

29 M.J. Berger and J.H. Hubbell, "XCOM: photon cross sections on a personal computer," *National Institute of Standards and Technology Report* no. NBSIR 87-3597 (Gaithersburg, MD: US Department of Commerce) (1987)

30 J.-P. Bissonnette, *Percent Depth Doses for Diagnostic Radiology*, M.Sc. Thesis, McGill University (1991)

31 S. Kubsad, R. Mackie, B. Gehring, D. Misisco, B. Puliwal, M. Mehta, and T. Kinsella, "Monte Carlo and Convolution Dosimetry for Stereotactic Radiosurgery," Int. J. Radiat. Oncol. Biol. Phys., **19**, 1027-1035 (1990).

32 F.H. Attix, *Introduction to Radiological Physics and Radiation Dosimetry*, (John Wiley & Sons, New York, 1986), p. 5-17.

33 D.W.O. Rogers, "Fluence to dose equivalent conversion factors calculated with EGS3 for electrons from 100 keV to 20 GeV and photons from 11 keV to 20 GeV," Health Physics, **46**(4), 891-914 (1984)

34 P. Munro, J.A. Rawlinson, and A. Fenster, "Therapy imaging: A signal-to-noise analysis of a fluoroscopic imaging system for radiotherapy localization," Med. Phys., **17**(5), 763-772 (1990)

35 A.L. Boyer, L. Antonuk, A. Fenster, M. Van Herk, H. Meertens, P. Munro, L.E. Reinstein, J. Wong, "A review of electronic portal imaging systems (EPIDs)," Med. Phys., **19**(1), 1-16 (1992)

36 F. Van den Heuvel, W. De Neve, M. Coghe, D. Verellen, and G. Storme, "Relations of image quality in on-line portal images and individual patient parameters for pelvic field radiotherapy," Eur. Radiol. **2**, 433-438 (1992)

Chapter 2. ACTIVITY DISTRIBUTION OF A COBALT-60 TELETHERAPY SOURCE[a]

Abstract

In the course of quantifying the effect of radiation source size on the spatial resolution of portal images, we have observed a concentric ring structure in the activity distribution of a Cobalt-60 teletherapy source. The activity distribution was measured using a strip integral technique and confirmed independently by a contact radiograph of an identical but inactive source replica. These two techniques suggested that this concentric ring structure is due to the packing configuration of the small ^{60}Co pellets that constitute the source. The source modulation transfer function (MTF) showed that this ring structure has a negligible influence on the spatial resolution of therapy images when compared to the effect of the large size of the ^{60}Co source.

[a] This chapter was pubished in *Medical Physics*, **18**(2), 288-291 (1991). The title of the article is "Activity distribution of a cobalt-60 teletherapy source" by D.A. Jaffray, P. Munro, A. Fenster, and J.J. Battista.

2.1 Introduction

Much effort has gone into predicting the radiation dose delivered to a specified treatment volume. Although an accuracy of 3-5 percent can now be expected[1], this accuracy is eroded by our inability to place the radiation field reproducibly at the correct anatomical site. Investigations have shown that errors in field placement occur frequently,[2,3,4,5,6,7] and that using portal films to confirm or correct patient set-up routinely is impractical.

The need for improvements in portal image quality has prompted the development of a number of digital techniques[8,9,10,11], as well as digitization and image enhancement of conventional film.[12] These developments in portal imaging have necessitated more detailed studies of the fundamental limitations in imaging system performance.[13,14] One of the basic factors which affects the spatial resolution of the portal imaging chain is the radiation source intensity distribution, which we will subsequently refer to as the source spot. With the recent application of a strip integral technique, it is possible to measure radiotherapy source spots quantitatively.[14] From these distributions, the source modulation transfer function (MTF) can be calculated for a specified image magnification and these MTFs can be used to estimate the effect of the source spot on spatial resolution.

The ^{60}Co source distribution for a ^{60}Co teletherapy machine (Theratron-780, Theratronics Inc., Ottawa, Canada) has been measured using the strip integral technique.[14] These measurements not only allow us to estimate what effect the source spot has on spatial resolution of portal images, but has also given us insight into the internal construction of the ^{60}Co source.

2.2 Materials and Methods

2.2.1 Active ^{60}Co Source: Strip Integral Technique

We investigated a ^{60}Co teletherapy source (Serial Number S-3883, Type C-146) manufactured for a Theratron-780 ^{60}Co teletherapy machine. In order to obtain the requested exposure rate, the manufacturer packed approximately 3500 pellets into the source canister. Each pellet had a specific activity of 275 Ci/g at the time of production,

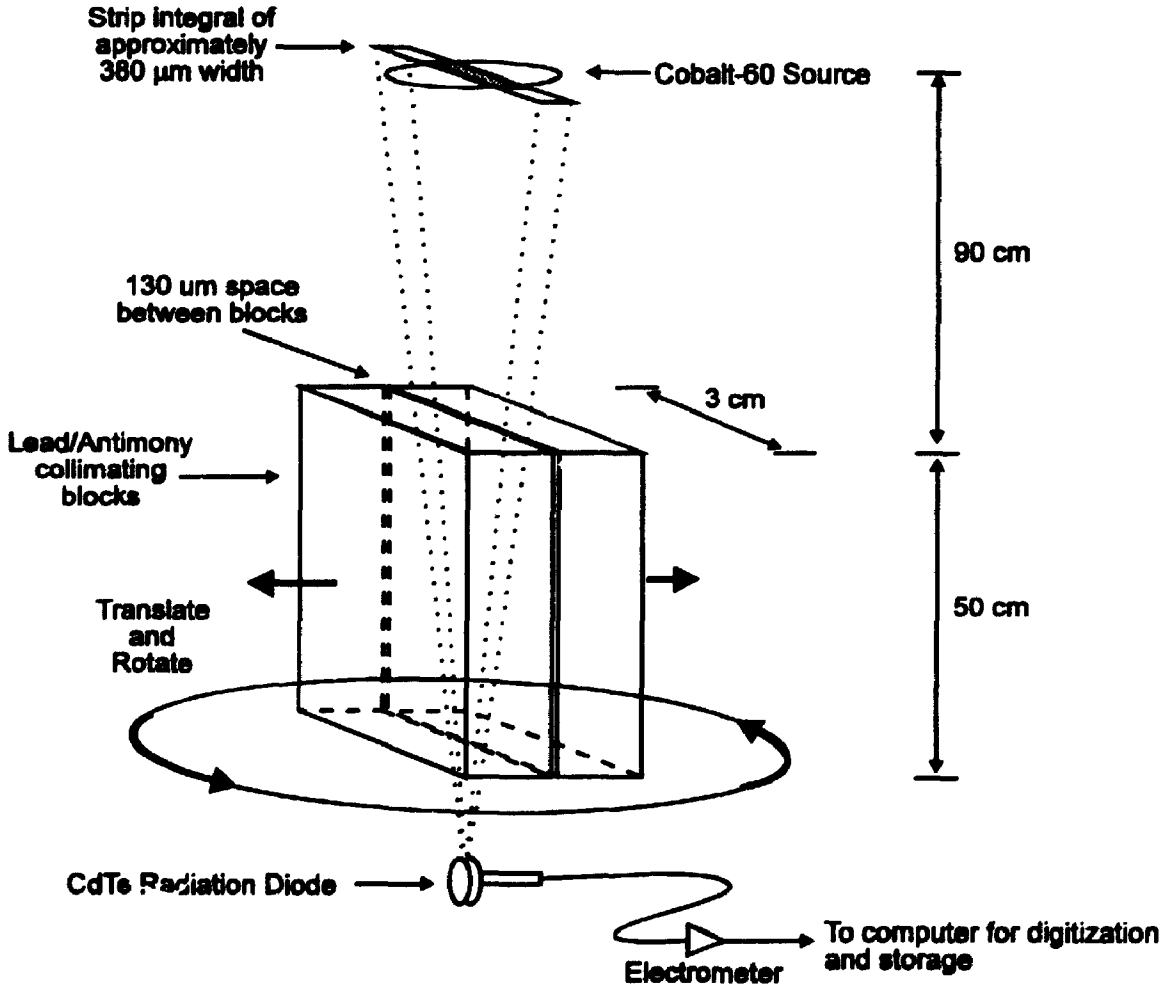

Figure 2.1 Schematic of strip integral technique. The shaded strip represents that portion of the source which produces the signal in the diode.

giving a net source activity of 7703 Ci.[15] At the time of measurements reported here, the source activity had decayed to 4830 Ci.

The activity distribution of this source was measured using the strip integral technique described by Munro et al..[14] Briefly, a collimation assembly restricts the view of a detector to a small strip on the source spot. The signal produced in the detector corresponds to an integration of photon emission over that strip. By collecting several of these strips at different locations and orientations on the source, the source spot is encoded in a series of strip integrals (Fig. 2.1), and can then be decoded using computed tomography (CT) reconstruction techniques.

In our measurements, these strip integrals were acquired using a computer-controlled apparatus. The apparatus consisted of a pair of 50cm long lead/antimony slabs which collimate the beam to a 130 μm slit of 3cm width (Fig. 2.1). The collimation assembly was mounted on a translation stage (Daedal 106041S-04M), which in turn, was mounted upon a rotation stage (Daedal 21001S, Harrison City, PA.). The entire assembly was placed on a large three-point levelling table to allow accurate alignment of the collimator axis with the beam axis.

The photon fluence reaching the detector plane was measured using a cadmium telluride (CdTe) radiation diode (Radiation Monitoring Devices Inc.). A Keithley model 617 electrometer was used to measure the small current (0.1 nA) through the unbiased diode and provided a corresponding voltage reading. This signal was digitized using a computer-controlled data acquisition board (DT2801A, Data Translation Inc., Marlborough, Mass.) and stored to magnetic disk.

Data collection consisted of linear and rotational scanning. A single linear scan was 25 mm in length and was divided into 100 data collection cycles. Each data

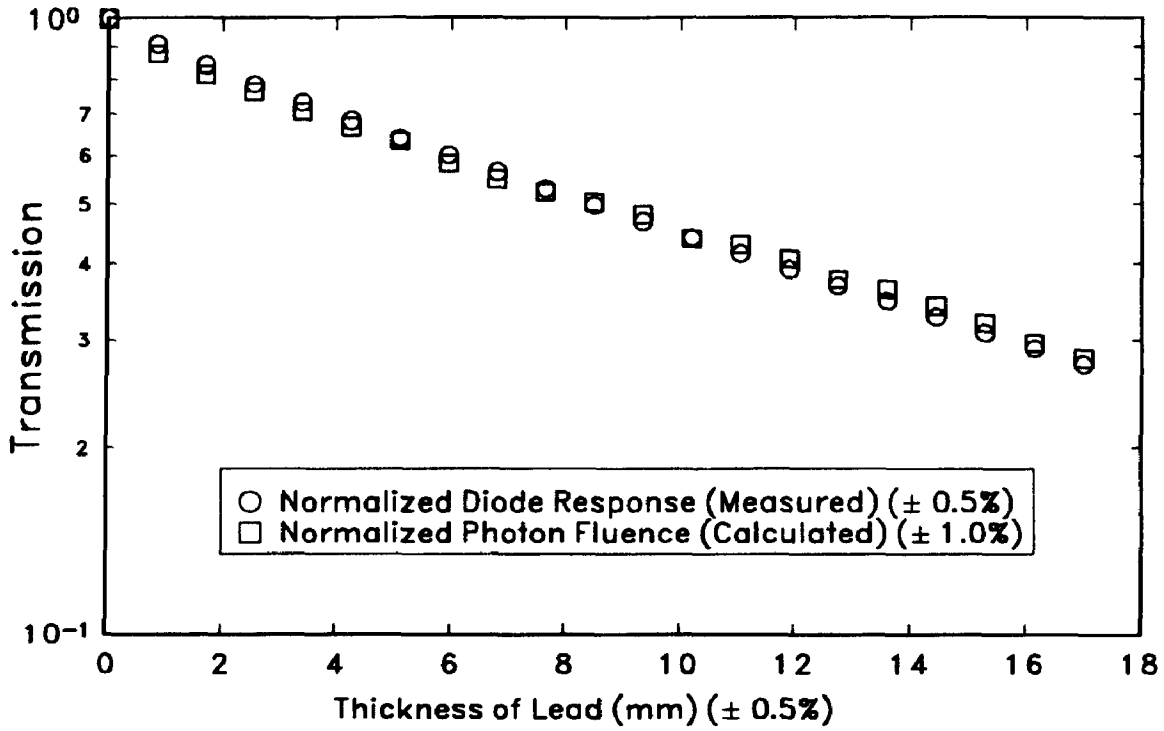

Figure 2.2 Evaluation of diode linearity. Measured diode response and calculated photon fluence incident on diode versus thickness of Pb attenuator.

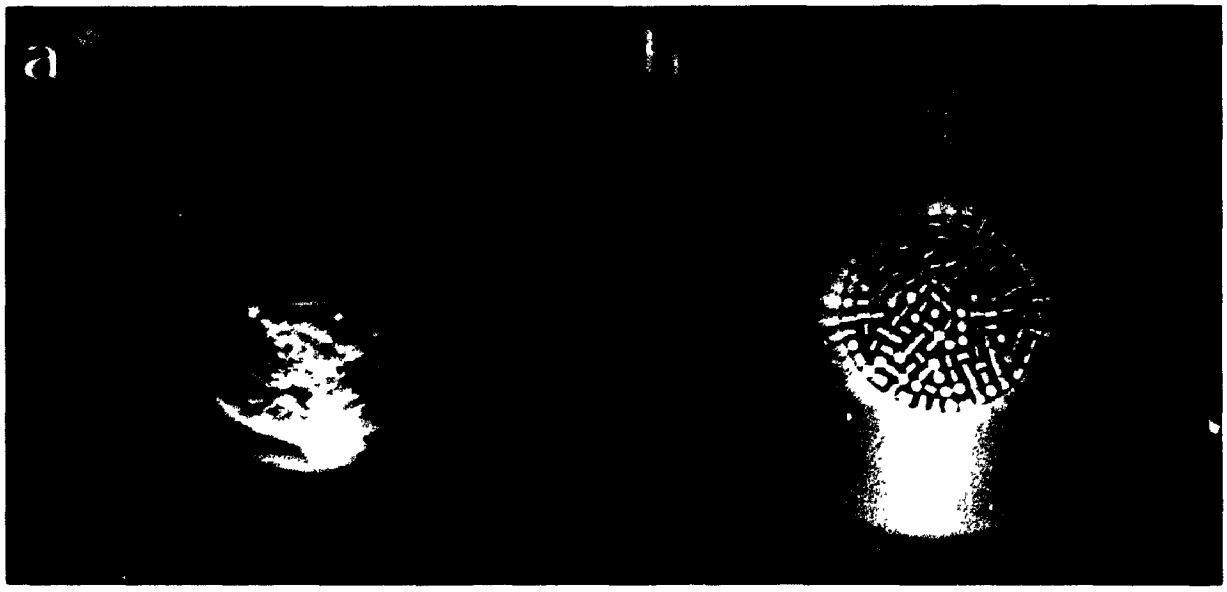

Figure 2.3 Inactive replica of ^{60}Co source, showing (a) the replica cannister filled with ^{59}Co pellets; and, (b) a single layer of pellets in the base of the cannister.

collection cycle lasted 4 seconds during which the collimator assembly was stationary and during which 1000 diode readings were averaged to give a single strip integral value. The averaging of multiple diode readings was designed to reduce noise in the strip integral measurements. Using this approach, the noise was reduced to 0.5% of the maximum diode signal. Upon completion of the 25mm linear scan, the assembly was rotated by 3 degrees and linear scanning was repeated. This process was repeated 61 times, collecting data over a 180 degree angular range.

Measurements to check the linearity of the CdTe diode were done immediately following data collection. These measurements consisted of collecting several diode current readings while gradually decreasing the incident photon fluence. The photon fluence was reduced to thirty percent of its maximum by placing thin layers of lead (0.85mm +/- 0.004mm) on top of the slit formed by the lead/antimony collimators. While adding layers of lead reduced the photon fluence, this procedure also filtered the photon spectrum. To study this, a theoretical attenuation of photon fluence was calculated using a published ^{60}Co spectrum.[16] The agreement between the measured and the calculated (Fig. 2.2) shows that the response of the diode is linear within our experimental error (+/- 2%).

2.2.2 Preparation and Radiography of the Inactive Cobalt Source

Visual inspection of the active ^{60}Co source is impossible. Therefore, we prepared an inactive replica by using ^{59}Co pellets and by imitating the packing and processing procedure used by the manufacturer[17]. The packing of the pellets was done by filling a source canister (Fig. 2.3a) with enough pellets to form one layer. The canister was then shaken laterally until the pellets became well packed and responded very little to further

Figure 2.4 Comparison of (a) measured ^{60}Co activity distribution with (b) radiograph of inactive replica filled with approximately 3500 ^{59}Co pellets.

agitation (Fig. 2.3b). This packing process was repeated until all the pellets (approximately 3500) were loaded into the canister.

A contact radiograph of the source replica was taken with a ^{60}Co teletherapy unit using standard radiotherapy verification film (150 cGy exposure on Kodak XV-2 verification film). The use of contact radiography (i.e. magnification of 1) and a 130 cm source-to-object distance minimized the effects of both beam divergence and blurring due to the finite source size.

2.3 Results and Discussion

2.3.1 Strip Integral Technique Results

Reconstruction of the source spot from the collected strip integrals was carried out using the Donner Laboratory RECLBL software package.[18] A gray scale image of the resulting distribution is shown in Figure 2.4a. The outside diameter of the measured source is 1.5 cm which is in agreement with the known physical size of the source. The distribution also displays a prominent ring pattern, as well as some intra-ring structure. The peak-to-trough variation in this ring pattern is typically 10% and proves to be significantly larger than the statistical uncertainity in the measurements (+/-2.5%).[18,19] Altogether, six rings of increased intensity can be seen in the distribution, with each ring having a width of approximately 1 mm.

2.3.2 Photographic and Radiographic Results

Figure 2.3a shows the canister used to form the source replica and Fig. 2.3b shows a single layer of pellets in the base of this canister. These pellets conform to the inside walls of the canister and organize into a concentric ring pattern. A contact radiograph of the same source canister with approximately 3500 ^{59}Co pellets in it is shown in Fig. 2.4b. *A concentric ring pattern and intra-ring structure comparable to that measured for the activity distribution of the ^{60}Co source can be seen.* It appears that even after many layers have been packed into the canister, the concentric ring pattern observed in Fig. 2.3b is maintained. Comparing the two results, there is a difference in the number of rings visible in the two images. In the strip integral result 6 rings can be seen compared to only 4 in the radiograph. This difference is believed to be due to our inability

to imitate fully the manufacturer's packing and processing procedures.

2.3.3 Influence on Portal Image Quality

In order to quantify the effect of the fine structure on portal image resolution, the MTF of the source spot was calculated. To simplify the MTF calculation, the point spread function (PSF) was converted to a line spread function (LSF) by integrating the PSF along an arbitrary axis. The axis on which the PSF was integrated was chosen arbitrarily since the PSF is essentially symmetric. The MTF was then calculated by taking the modulus of the 1-D Fourier Transform of the LSF and scaling the result to account for image magnification, which was assumed to be 1.2. The resulting MTF is plotted in Fig. 2.5.

If the cobalt source was assumed to be a perfectly flat disk of activity, the source

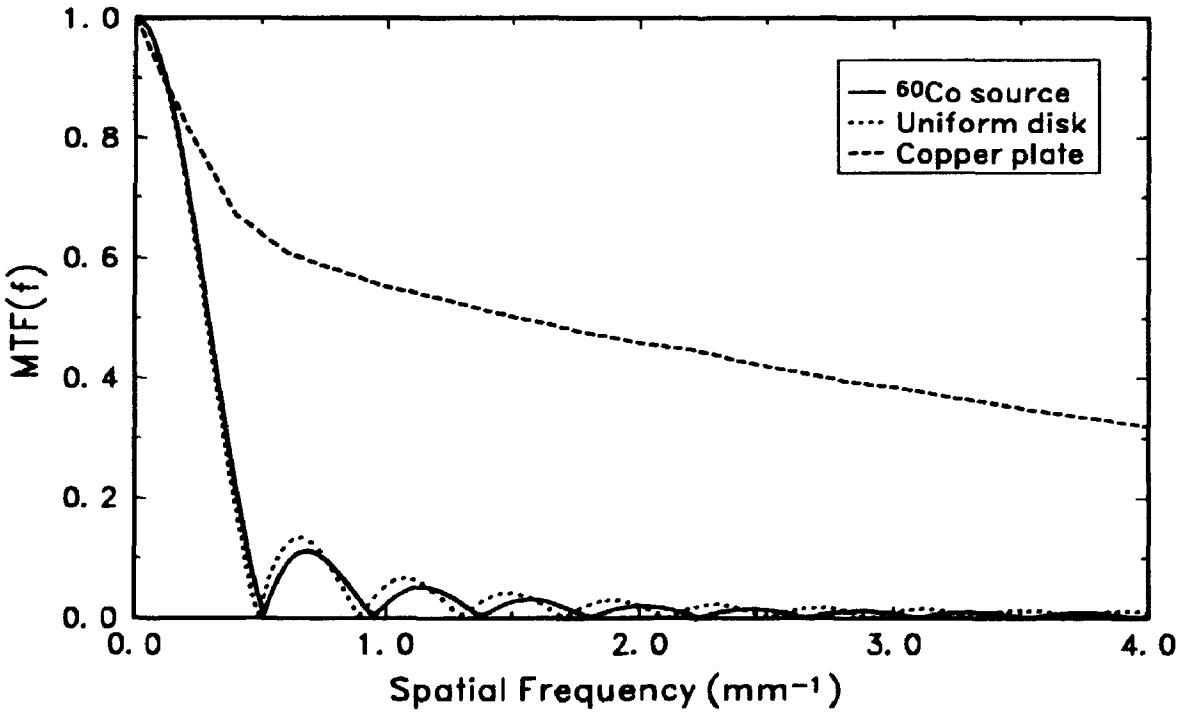

Figure 2.5 Source MTFs calculated from measured ^{60}Co activity distribution and theoretical uniform disk. The MTF of a copper conversion plate is shown for comparison. All MTFs were calculated assuming a magnification of 1.2

MTF would result in an Airy function.[20] An Airy function for a 1.5 cm diameter source is also shown in Fig. 2.5.

It can be seen that the ring structure has a negligible influence on the source MTF. The ^{60}Co source MTF and the Airy function for a 1.5 cm diameter disk are identical with the exception of a slight difference in modulation between the first and second zero points. For comparison, the MTF due to a copper conversion plate often used in portal film cassettes is also shown (Fig. 2.5).[14] It is clear that the large ^{60}Co source size will produce a dominant loss of spatial resolution in a typical portal film imaging system.

2.4 Conclusion

Our results have revealed an interesting ring structure in the activity distribution of a ^{60}Co source used in teletherapy. This structure is attributed to the packing of the small ^{60}Co pellets within the source canister. The source MTFs were calculated to quantify the effect of this fine structure on the spatial resolution of portal images. Comparison of this result to the MTF for a uniform distribution showed that the rings had little influence when compared to the effect of the large overall size of the source.

References

1. International Commission on Radiation Units and Measurements, **24**, 45-50, (1976)

2. R.W. Byhardt, James D. Cox, Allan Hornburg, Gail Liermann, "Weekly Localization Films and Detection of Field Placemant Errors," Int J. Radiation Oncology Biol. Phys., **4**, 881-887, (1978)

3. M. Goitien and Joel Busse, "Immobilization Error: Some Theoretical Considerations," Radiology, **117**, 407-412, (1975)

4. Ian Rabinowitz, J. Broomberg, M. Goitien, K. McCarthy, and J. Leong, "Accuracy of Radiation Field Alignment in Clinical Practice," Int. J. Radiation Oncology Biol. Phys., **11**, 1857-1867, (1985)

5. J.J. Kinzie, G. Hanks, C.J. Maclean, and S. Kramer, "Patterns of Care Study: Hodgkin's Disease Relapse Rates and Adequacy of Portals," Cancer **52**, 2223-2226 (1983).

6. S. Griffiths, "Hit or Miss - Is Perfection Achievable in Radiotherapy?," Radiography Today, **55**, No 620, January, 1989

7. H. Huizenga, P.C. Levendag, P.M.Z.R De Porre, and A.G. Visser, "Accuracy in radiation field alignment in head and neck cancer: A prospective study," Radiotherapy and Oncology, **11**, 181-187 (1988)

8. N.A. Baily, R.A. Horn, T.D. Kampp, "Fluoroscopic Visualization of Megavoltage Therapeutic X-ray Beams," Int. J. Radiation Oncology Biol. Phys., **6**, 935-939 (1980)

9. H. Meertens, M van Herk, J. Weeda, "A Liquid Ionization Detector for Digital Radiography of Therapeutic Megavoltage Photon Beams," Phys. Med. Biol., **30**, 313-321, (1985)

10. P. Munro, J.A. Rawlinson, and A. Fenster, "A Digital Fluoroscopic Imaging System for Radiotherapy Localization," Int. J. Radiation Oncology Biol. Phys., **18**, (1990)

11. J. Leong, "Use of digital fluoroscopy as an on-line verification device in radiation therapy," Phys. Med. Biol., **31**, 985-992 (1986)

12. H. Meertens, "Digital processing of high energy photon beam images," Med. Phys., **12**(1), 111-113, (1985)

13. P. Munro, J. A. Rawlinson, and A. Fenster, "Therapy imaging: A signal-to-noise analysis of metal plate/film detectors," Med. Phys., **14**(6), 975-984, (1987)

14. P. Munro, J. A. Rawlinson, and A. Fenster, "Therapy imaging: Source sizes of radiotherapy beams," Med. Phys., **15**(6), 517-524, (1988)

15. J. Slobodian, Theratronics Inc, Ottawa, Ontario, Canada, Personal Communication

16. K. Han, D. Ballon, C. Chui, R. Mohan, "Monte Carlo Simulation of a Cobalt-60 Beam," Med. Phys. **14**(3), 414-419, (1987)

17. Ron Strike, Nordion Industries Inc., Ottawa, Ontario, Canada, Personal Communication

18. R. H. Huesman, G. T. Gullberg, W. L. Greenberg, and T. F. Budinger, "Donner Algorithms for Reconstructive Tomography Users Manual," Lawrence Berkeley Laboratory Publication No. 214, 1977

19. R. A. Brooks and G. DiChiro, Phys. Med. Biol. **21**, 689 (1976)

20. G. B. Airy, Trans. Camb. Phil. Soc., **5**, 283 (1835)

Chapter 3. X-RAY SOURCES OF MEDICAL LINEAR ACCELERATORS: FOCAL AND EXTRA-FOCAL RADIATION[a]

Abstract

We have applied a CT reconstruction technique to make quantitative measurements of the size and shape of the focal spot in medical linear accelerators. Using this technique, we have measured the focal spots in a total of nine accelerators, including: (i) two Varian Clinac 2100c's, (ii) two Atomic Energy of Canada Ltd.* (AECL) Therac 25's, (iii) two AECL Therac 6's, (iv) a Siemens KD-2, (v) a Varian Clinac 600c (4 MV) and (vi) a Therac 20. Some of these focal spots were monitored for changes over a two year period. It has been found that: (i) the size and shape of the source spot varies greatly between accelerators of different design ranging from 0.5 to 3.4 mm in full-width-at-half-maximum (FWHM); and (ii) for accelerators of the same design, the focal spots are very similar. In addition to our measurements of the focal spot, a new technique for measuring the magnitude and distribution of extra-focal radiation originating from the linear accelerator head (flattening filter, primary collimator) has also been developed. We have measured the extra-focal radiation produced by a Varian Clinac 2100c accelerator using this technique and found that the extra-focal radiation accounts for as much as 8% of the total photon fluence reaching the isocentre. The majority (75%) of this extra-focal radiation originates from within a circle 6 cm in diameter at the target plane. The source MTFs for each of the measured focal spots have been calculated in order to assess their

[a] This chapter was published in *Medical Physics,* **20**(5), 1417-1427 (1993). The title of the article was "X-ray sources of medical linear accelerators: focal and extra-focal radiation" by D.A. Jaffray, J.J. Battista, A. Fenster, and P. Munro.

influence on the spatial resolution of verification images. The limiting spatial resolution (i.e. 10% modulation) for all the source MTFs is 1.8 mm^{-1} or greater when used for transmission radiography at a magnification of 1.2. The extra-focal radiation, which produces a low-frequency drop in the source MTFs of up to 8%, changes with field size. As a result, the source MTFs of linear accelerators depend not only on the design of individual accelerators and image magnification, but also on the field size used when forming an image.

3.1 Introduction

The size and shape of the x-ray source produced in a medical linear accelerator is of interest in both the calculation of radiotherapy dose distributions[1,2,3] for determining primary beam penumbra, and in verification imaging for determining the degree of blurring due to the finite size of the source.[4,5,6] Despite its importance, relatively little quantitative data on the size and shape of these x-ray sources is available in the literature. The size and shape of the focal region of the source (focal spot) for an 8 MV x-ray beam has been measured by Lutz et al.[7] using a beam-spot camera composed of alternating lead and cardboard sheets. Loewenthal et al.[8] measured the 6 and 18 MV focal spots of a Varian Clinac 1800 using a similar technique based on a single, translated slit. Both of these techniques measure a projection of the focal spot and infer the size and shape by assuming rotational symmetry. Munro et al.[9] developed a technique which allows measurement of the size and shape of the focal spot in a medical linear accelerator. His technique is based on CT reconstruction principles and allows reconstruction of the full spatial distribution of the focal spot.

Since so few focal spots were examined in these studies, the authors were neither able to determine whether the size and shape of a focal spot varies with time, nor whether the focal spots of two accelerators of identical design were similar. In addition, the authors do not examine how the focal spot size and shape appears to change when measurements are made at points off the central axis of the x-ray beam. And finally, these studies only investigate the focal spot and do not consider any extra-focal contributions. While the majority of the x-ray fluence generated by the accelerator is emitted from the focal spot, a sizeable fraction (~10%) originates from the structures (primary collimator, flattening filter) surrounding the target;[10,11] these contributions

constitute the *extra-focal* portion of the source. (For clarity we will refer to the radiation emitted from the target as the *focal spot* radiation, while the *focal* plus *extra-focal radiation* will be referred to as the *x-ray source.*) The literature contains little information describing the size and shape of the extra-focal portion of the source. An indirect measure of the magnitude of the extra-focal radiation has been reported by a number of authors, through measurement of the output factors for medical linear accelerators.[11,12,13,14,15,16,17] While the magnitude of the extra-focal radiation can be inferred from changes in the output factor with field size, the spatial distribution of the extra-focal radiation has not been measured directly. The only attempt at measuring the extra-focal source was made by Wilkinson et al[3] for a ^{60}Co treatment machine, however, this work was not published. The extra-focal region of the x-ray source is quite important clinically because its size and shape will influence both accelerator output and beam penumbra as a function of field size.

In this paper, we report on the focal spots of nine medical linear accelerators measured using the CT reconstruction technique.[9] These studies, which were taken over a 5 year period, include repeated measurements on the same accelerator as well as comparative studies between different accelerators of the same design. These results allow us to determine the variations in the focal spot of the accelerator with time, and give us insight into the variability of focal spot size and shape between machines of the same design. In addition, we report on the development of a new technique to measure the magnitude and distribution of the extra-focal radiation and describe the use of this technique to measure the extra-focal radiation produced by a Varian Clinac 2100c accelerator. Our measurements of the x-ray source (focal and extra-focal) can be used to calculate the modulation transfer function due to the source (source MTF) for a specified imaging geometry (magnification, field size), demonstrating the effect of the

entire x-ray source on the spatial resolution of radiotherapy verification images.

3.2 Materials and Methods

3.2.1 Focal spot measurement technique

The focal spots were measured using the CT reconstruction technique described previously.[9,18] Briefly, a collimator assembly restricts the view of a radiation detector to a small strip at the source. The signal produced in the detector corresponds to the integral of x-ray emissions over that strip [Fig. 3.1a]. By recording the signal from several of these strips at different locations and angular orientations with respect to the source,

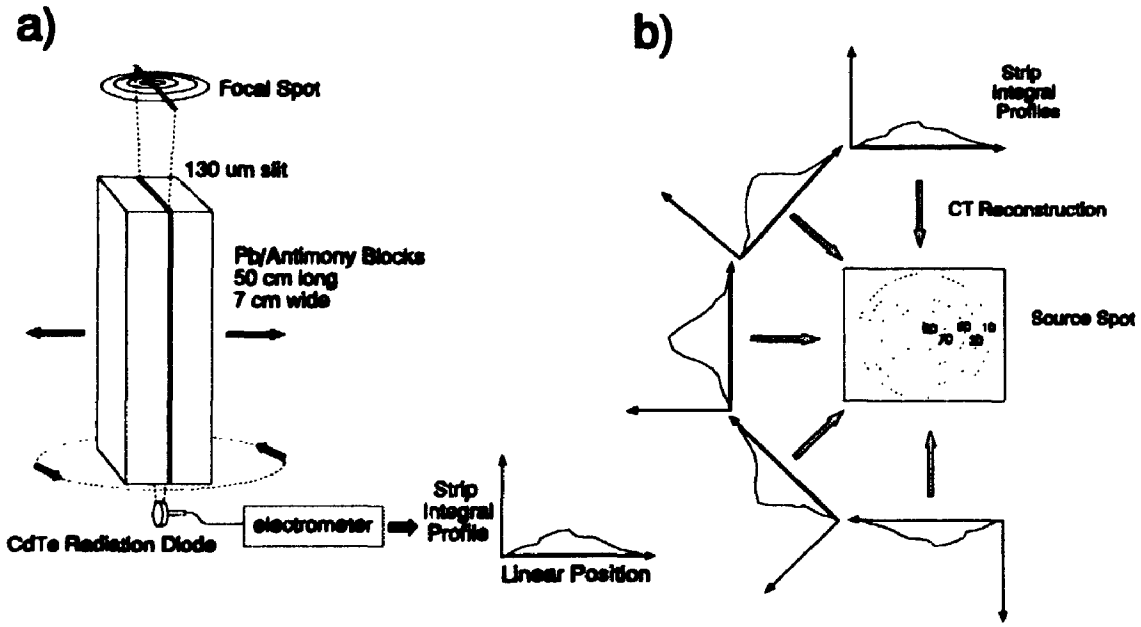

Figure 3.1 (a) Schematic diagram of the focal spot measurement apparatus Translation of the apparatus underneath the focal spot results in a strip integral profile. (b) Reconstruction of the focal spot

the focal spot is encoded in a series of strip integrals, and can then be decoded using computed tomography (CT) reconstruction techniques [Fig. 3.1b].

In our measurements, these strip integrals were acquired using a computer-controlled apparatus. The apparatus consisted of a pair of 50 cm long lead/antimony slabs, which collimate the beam to a 130 μm slit of 3 cm length [Fig. 3.1a]. The collimator assembly was mounted on a translation stage (Daedal 106041S-04M, Harrison City, PA.), which, in turn, was mounted upon a rotation stage (Daedal 21001S). The entire assembly was placed on a large three-point levelling table to allow alignment of the collimator axis with the beam axis.

The photon fluence reaching the detector plane was measured using a cadmium

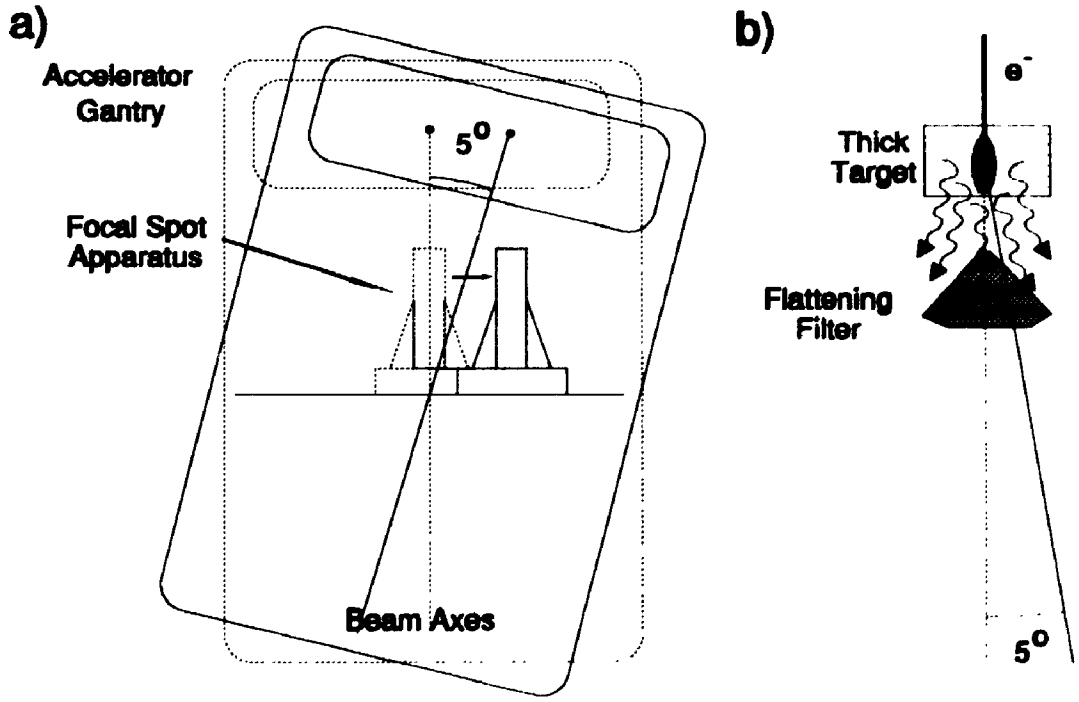

Figure 3.2 Schematic diagram showing the off-axis measurement of the focal spot The gantry was rotated to 5 and the focal spot apparatus was repositioned to view the source

telluride (CdTe) radiation diode (Radiation Monitoring Devices Inc.). A Keithley model 617 electrometer was used to measure the small current (~0.1 nA) through the unbiased diode and provided a corresponding voltage reading. This signal was digitized using a data acquisition board (DT2801A, Data Translation Inc., Marlborough, Mass.) and stored on the magnetic disk of a personal computer.

A typical focal spot measurement required approximately 9000 monitor units of x-ray beam (40 minutes). The linear scans ranged from 6 mm to 10 mm in length and were divided into 30 to 100 data collection cycles (step size, Δx), depending on the spatial extent of the focal spot. Each data collection cycle lasted 1 second during which the collimator assembly was stationary and during which 1000 diode (current) readings were collected and then averaged to give a single strip integral value. The averaging of

Accelerator	Energy (MV)	Date of Measurement	Δx (mm)	$\Delta\theta$ (°)	FOV (mm)
Varian 2100c #1	6 & 18	May 89 May 91	0.06	5	6
Varian 2100c #2 (on & off-axis)	18	Aug 89	0.06	5	6
Varian 2100c #2	6 & 18	May 91	0.06	5	6
Siemens KD-2	6 & 23	May 92	0.1	5	10
Therac 25 #1	25	May 87	0.05	10	10
Therac 25 #2	25	June 92	0.1	5	10
Therac 6 #1	6	Oct 86	0.22	10	10
Therac 6 #2	6	Dec 91	0.1	5	10
Varian 600c	4	Nov 91	0.1	5	10
Therac 20	18	Oct 86	0.22	10	10

Table 3.1 The sampling parameters (Δx, $\Delta\theta$, field-of-view) for each of the measured focal spots The field-of-view (FOV) was determined by the size of the source being scanned.

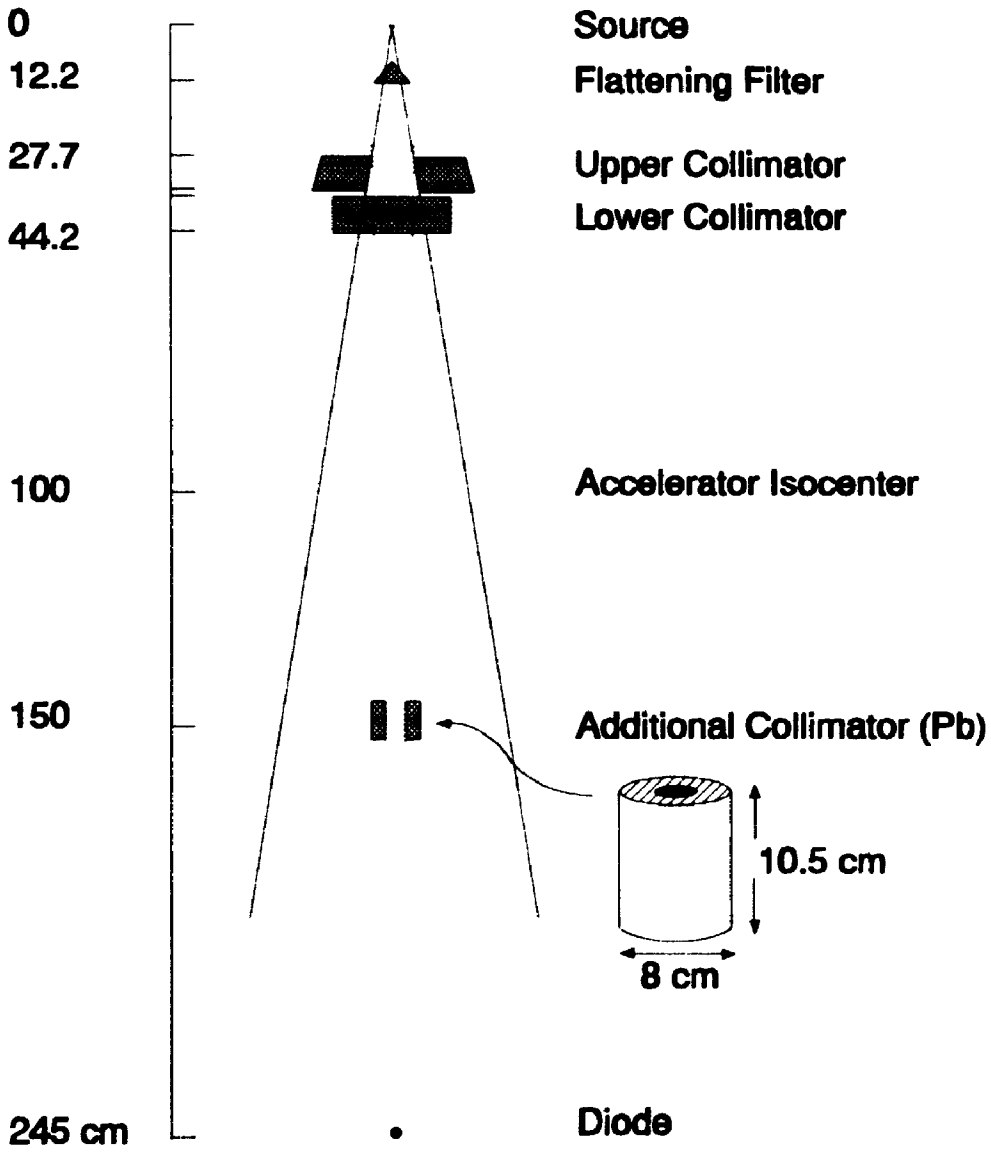

Figure 3.3 Schematic diagram showing the experimental setup used for our study of extra-focal radiation The scale is given in the left-hand side of the figure

multiple diode readings reduced the noise in the strip integral measurements. Upon completion of the linear scan, the assembly was rotated by 5 or 10 degrees (angular increment, $\Delta\theta$) and the linear scanning was repeated. Each linear scan produced a series of strip integral values which we will refer to subsequently as a *strip integral profile* [Fig. 3.1b]. This process was repeated until data were collected over 180°. A tabulation of the sampling parameters (Δx, $\Delta\theta$, field-of-view [FOV]) for each of the measured sources is shown in Table 3.1.

The focal spots were reconstructed from the measured strip integral profiles using the Donner algorithms for reconstruction tomography.[19] The profiles were convolved using the Shepp and Logan[19] (SHLO) kernel and back-projected onto an 80x80 array.

The resolution of the focal spot measuring assembly is limited by the width of the scanning slit (130 μm). Assuming the reconstruction grid is of sufficient resolution, the system is capable of resolving a 125 μm object at the source plane. The uncertainty, due to noise, in the measured focal spot distributions is minimized by oversampling in the linear scan direction and by using prolonged exposures for each strip integral measurement. We have estimated the uncertainty in the focal spot distributions to be approximately +/- 2.5%.[18]

To determine whether the shape of the focal spot changes as one moves away from the centre of the beam, the 18 MV x-ray focal spot of the Varian Clinac 2100c (#2) was re-measured 5° off the central axis. This was done by rotating the accelerator gantry to 5° and shifting the measuring apparatus to bring the focal spot back into the FOV of the apparatus [Fig. 3.2]. A complete scan of the focal spot was then performed. The resulting distribution was then compared to the same measurement made on the central axis.

3.2.2 Extra-focal measurement technique

The magnitude and distribution of the extra-focal radiation for a Varian Clinac 2100c accelerator (6 MV) was measured using the geometry described in Fig. 3.3. The gantry of the Varian 2100c accelerator was rotated to 90 degrees and a silicon radiation diode with brass build-up (#2004, Theta Systems, USA) was placed on the central axis at a distance of 245 cm from the source. (The brass buildup was sufficient to provide full electronic equilibrium in a 6 MV beam.) An additional collimator placed on the central axis at 150 cm from the x-ray source restricted the field-of-view of the diode at the head of the accelerator. The diameter of the field-of-view was increased by exchanging a series of additional collimators each having an increasingly larger aperture. The diameter of the collimator apertures at the face closest to the diode (these are divergent collimators) are 5.3, 6.7, 8.8, 10.2, 11.7, 13.6, 15.0, 15.4, 15.9, 17.1, 19.2, 20.4, 21.5, and 22.9 mm. As the field-of-view is increased, a larger fraction of the extra-focal radiation can reach the diode resulting in an increase in the diode signal. The measurement technique has been designed so that the diameter of the circular area viewed by the diode at the target plane of the accelerator can be varied from 1.4 to 6.4 cm while minimizing the amount of scatter contributions from the additional collimator itself. This is accomplished by separating the diode and the additional collimator by a 95 cm air gap. Furthermore, increases in the size of the aperture result in only small changes in the mass of the additional collimator. Therefore, any changes in signal measured by the radiation diode are attributed to changes in the extra-focal radiation reaching the diode and are *not* due to changes in scatter from the extra collimator. These measurements were performed for a total of 10 square field size settings on the accelerator (1, 2, 3, 5, 10, 15, 20, 25, 30, 40 cm on a side).

To account for room scatter, measurements were made for each of the field size settings while the additional collimator was completely blocked. In this geometry, all direct contributions from the focal and extra-focal portions of the x-ray source are removed, thereby allowing us to determine the amount of signal generated in the diode by x-rays which have scattered off the walls and surrounding equipment (room scatter). For each field size setting, the measured room scatter signal (~3%) was subtracted from the open-aperture diode signals. When the room scatter signal is subtracted from measurements made with the additional collimator completely removed, the resulting signal is due to photons which pass through the volume originally occupied by the additional collimator. From the diode's perspective, this volume projects to a 20.6 cm diameter area of view at the target plane; the resulting signal corresponds to the largest aperture in our results.

Since the corrected diode signals correspond to a cumulative integral over the extra-focal source distribution, the extra-focal source distribution (diode signal/cm^2 at the target plane) can be calculated by differentiating these signals with respect to the increase in area viewed by the radiation diode at the target plane. For the small field sizes, 5 cm x 5 cm and 10 cm x 10 cm, the measured diode signal becomes constant (+/- 0.5%) within the first two centimetres. This occurs because the field-of-view exceeds the aperture of the secondary collimator, and hence, no more of the extra-focal radiation is detected by diode. Differentiating the diode signal with respect to area is very sensitive to any noise in the measurements. For this reason, a smooth curve was fit to the measured data for the 5 cm x 5 cm and 10 cm x 10 cm field sizes. This curve was constrained to have a slope greater than or equal to zero, since the diode signal should never decrease with increasing field-of-view (as it is a cumulative integral over a positive distribution). The smooth curve was then sampled at the radii corresponding to the

original measurements. This technique of measuring the extra-focal radiation is based on two assumptions. First, we assume the extra-focal radiation, originating from the head of the accelerator, is emitted uniformly over the angular range of +/- 10° from the central axis. This makes our measurements of the extra-focal radiation, as detected by the diode at 245 cm from the source, representative of what would be detected at the isocentre. Secondly, it is assumed that the extra-focal radiation is circularly symmetric about the focal spot. This assumption is quite reasonable for the region within the secondary collimators. However, the periphery of the extra-focal distribution is likely rectangular because the secondary collimators occlude the extra-focal distribution.

3.2.3 Calculation of source MTFs

The effect of the x-ray source (focal and extra-focal regions) on the spatial resolution of radiotherapy verification images can be described by the source MTF. The influence of extra-focal radiation on source MTFs has been described previously.[20] Since the extra-focal radiation originates from a region much larger than the focal spot itself (by one or two orders of magnitude larger), it influences the shape of the source MTF only at very low frequencies (i.e. produces a low-frequency drop). This low-frequency drop results in a uniform reduction (i.e. renormalization) of the source MTF at higher frequencies. The magnitude of the low-frequency drop is equal to the percentage of the primary fluence which originates from the extra-focal region (Appendix A). In this paper, the source MTFs corresponding to the entire x-ray source (including extra-focal contributions) have been calculated by multiplying the MTFs calculated from the focal spot alone by a factor equivalent to the percentage of the primary fluence which originates from the focal spot.

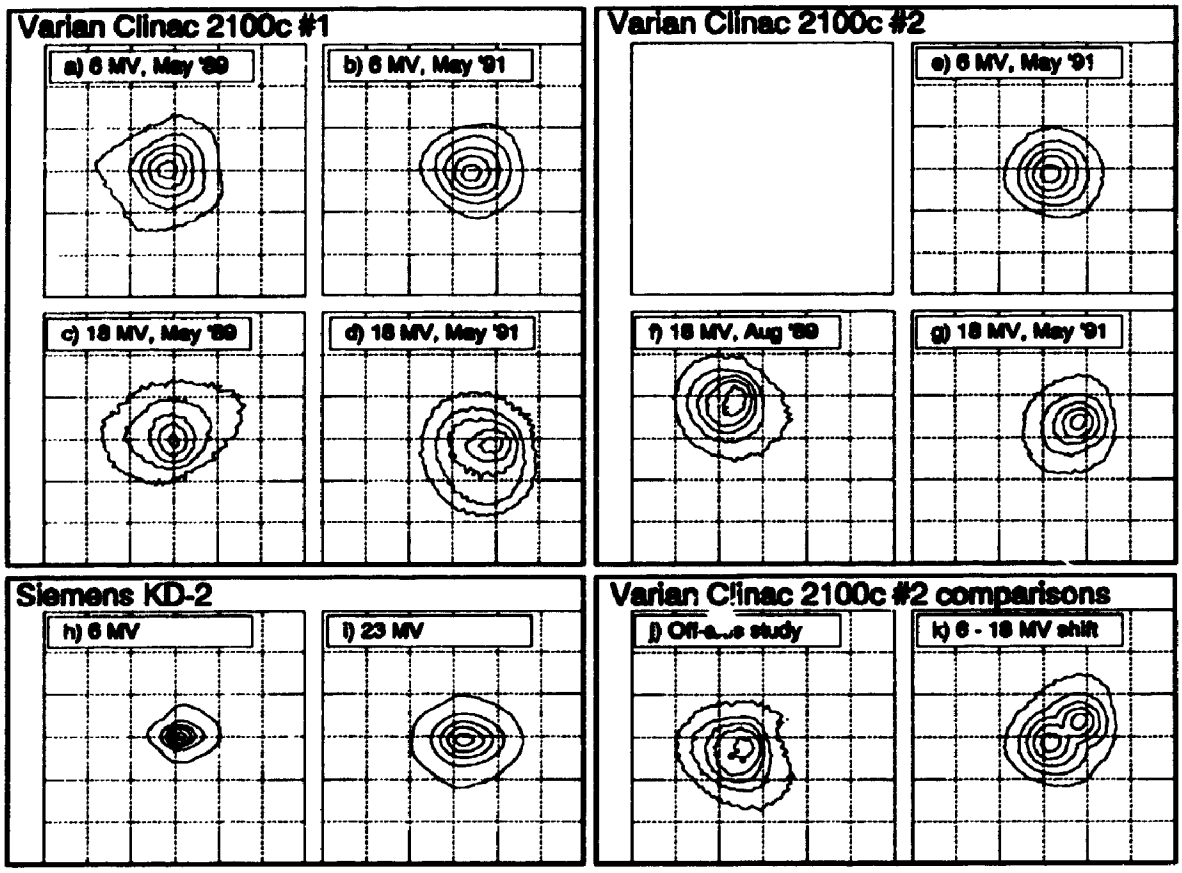

Figure 3.4 Focal spots for the Varian 2100c [#1 and #2] [(a)-)g), (j)-(k)] and the Siemens KD-2 [(h)-(i)]. The contour lines correspond to 10%, 30%, 50%, 70% and 90% of maximum.

There are two ways to determine the source MTFs corresponding to the focal spots alone. The 2-dimensional source MTF can be calculated by taking the Fourier transform of the focal spot and by scaling the frequency axis appropriately to account for the desired magnification. A radial slice along any central axis of the 2-D source MTF can be extracted, yielding the 1-D MTF for that orientation. This method of calculating the source MTF requires that the focal spot be reconstructed from the measured strip integral profiles. However, the reconstruction produces uncertainty in the MTFs because angular undersampling of the focal spots leading to artefacts at the periphery of the reconstructed focal spot.[21]

An alternative approach is to calculate the 1-D source MTF from the strip integral profiles directly. The central-slice theorem[21] states that a central profile through the 2-D Fourier representation of a 2-D spatial distribution is given by the Fourier transform of the strip integral profile of the distribution. Therefore, 1-D source MTFs corresponding to specific axes of the focal spot can be calculated by finding the Fourier transform of the measured strip integral profiles directly, without reconstructing the focal spot. This eliminates the uncertainties associated with the reconstruction process itself. This technique also allows the source MTF to be found for a specific axis of the focal spot by acquiring a single strip integral profile, resulting in a large reduction (1/36) in data collection time. The source MTFs reported here were calculated using the latter approach.

Each strip integral profile was centred on a 1024 element array and zero-padded to allow use of the FFT algorithm and to improve sampling in frequency space, respectively. The frequency axis of the MTFs were scaled to correspond to frequencies in the object plane for an image magnification of 1.2. Furthermore, the MTFs were

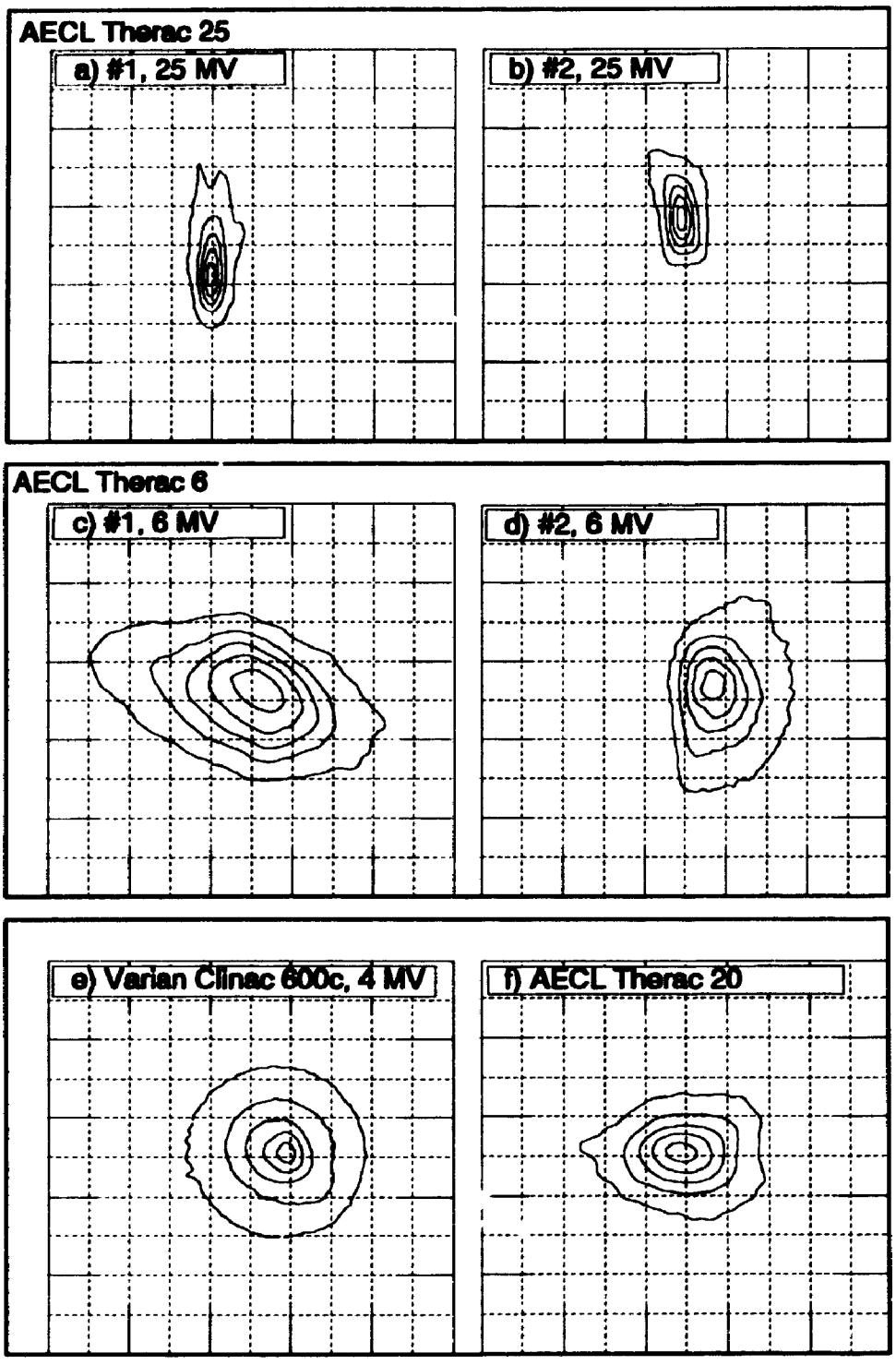

Figure 3.5 Focal spots for the AECL Therac-25, Therac-20, Therac-6 and Varian Clinac 600c accelerators. The contours correspond to 10, 30, 50 ,70 ,and 90% of maximum.

corrected for the finite width of the slit used in measuring the strip integral profiles; this correction was less than 4% for the frequencies of interest.[22]

3.3. Results

3.3.1 Focal spot size and shape

In total, nine different accelerators were studied, including: (i) two Varian Clinac 2100c's; (ii) two AECL Therac 25's; (iii) two Atomic Energy of Canada Ltd. (AECL) Therac 6's; (iv) a Siemens KD-2; (v) a Varian Clinac 600c (4 MV); and, (vi) a Therac 20. The reconstructed focal spots shown in Figs. 3.4 and 3.5 are represented with contour plots in which the 5 contour lines correspond to 10, 30, 50, 70 and 90 % of the maximum in the distribution. The grid spacing in all the plots reported here is 1 mm.

The size of each measured focal spot has been tabulated in Table 3.2. The full-width-half-maximum (FWHM), full-width-tenth-maximum (FWTM) on the major and minor axes of the focal spot and eccentricity at FWTM are shown. The eccentricity of the focal spot, e, is defined to be the ratio of $FWTM_{major}$ to $FWTM_{minor}$.

The focal spots of the two Varian 2100c accelerators are shown in Fig. 3.4(a-g). Measurements were made in 1989 and 1991 for both the 6 MV and 18 MV x-ray modes. Unfortunately, the 6 MV focal spot on accelerator #2 was not measured in August 1989 because of accelerator failure. The focal spots are all similar in size (0.9-1.6 mm FWHM) and shape ($e < 1.4$). The 18 MV focal spot on the 2100c #1 was the most asymmetric and also the largest of all the 2100c sources.

The focal spots for the two Therac 25 (25 MV) accelerators are shown in Fig. 3.5a and 3.5b. These correspond to two different accelerators at two different clinics measured

approximately 5 years apart. The Therac 25 focal spots are the most asymmetric of all those investigated, as described by their eccentricities (#1 - e=3.1, #2 - e=2.5).

The focal spots for two Therac 6 accelerators [Fig. 3.5c and 3.5d] showed the greatest differences in size and shape between two accelerators of identical design. These two spots, which were measured approximately 5 years apart, on accelerators installed at different cancer centres, have similar shapes - as given by their eccentricity (#1 e=1.8, #2 e=1.9). However, the focal spot on accelerator #1 was about 1.4 times larger than that of accelerator #2.

The focal spot of the Siemens KD-2 was measured at both operating energies (6 MV - Fig. 3.4h and 23 MV - Fig. 3.4i). The 23 MV spot is comparable in size to the Varian 2100c focal spots. The 6 MV mode on the Siemens KD-2 has the smallest of all the focal spots investigated; it has a FWHM of only 0.5 mm.

3.3.2 Relative focal spot position

The mechanical rigidity and operating software of the focal spot measuring device has been improved considerably from that reported in previous studies[9] so that we can now determine the *position* of a focal spot as well as its size and shape. This capability has revealed that the position of the two focal spots in dual energy accelerators do not necessarily coincide. This was demonstrated by the measurements performed on the Varian Clinac 2100c #2, where a shift of 0.8 mm was observed between the 6 and 18 MV focal spots. Figure 3.4k contains a plot of the two focal spots, showing the relative shift. This plot was generated by plotting the maximum of the two focal spots for each point in the distribution.

3.3.3 Off-axis perspective

Since the x-ray fluence produced in a medical linear accelerator is generated throughout a thick transmission target, the focal spot has a three-dimensional shape. Our device can only measure a 2-D "projected" distribution; therefore, the measured distribution may change depending upon the angle used to view the (3-D) focal spot (i.e. off-axis points versus on the central axis). This is further complicated by the presence of the flattening filter, since for off-axis points, the x-ray fluence travels through a reduced thickness of the flattening filter compared with the central axis thickness [Fig. 3.2].

In order to determine whether the 2-D projection of the x-ray source is similar for

Accelerator	Energy (MV)	Date Measured	FWHM (mm)		FWTM (mm)		
			major	minor	major	minor	ε
Varian 2100c #1	6	May 89	1 4	1 2	2 9	2 3	1 3
	6	May 91	1 4	1 2	2 3	2 3	1 0
	18	May 89	1 3	1 0	3.2	2 3	1 4
	18	May 91	1 6	1 3	2 9	2 6	1 1
Varian 2100c #2	6	May 91	1 2	1 2	2 2	1 9	1 2
	18	May 91	1 1	0 9	2 4	2 0	1 2
Varian 2100c #2 (on & off-axis)	18	Aug 89	1 4	1 4	2 7	2 3	1 2
	18	Aug 89	1 4	1 3	2 8	2 4	1 2
Siemens KD-2	6	May 92	0 7	0 5	1 7	1 4	1 2
	23	May 92	1 2	0 9	2 6	2 2	1 2
Therac 25 #1	25	May 87	1 8	0 5	3 7	1 2	3 1
Therac 25 #2	25	June 92	1 6	0 5	3 2	1 3	2 5
Therac 6 #1	6	Oct 86	3 4	2 3	7 1	3 8	1 9
Therac 6 #2	6	Dec 91	2 3	1 6	5 5	3 0	1 8
Varian 600c	4	Nov 91	1 8	1 6	4 7	4 5	1 0
Therac 20	18	Oct 86	2 0	1 5	4 1	3 0	1 4

Table 3.2 The size of the measured focal spots. The full-width-half-maximum (FWHM), full-width-tenth maximum (FWTM) and eccentricity at FWTM have been determined for each source. The eccentricity of the focal spot, ε, is defined to be the ratio of $FWTM_{major}$ to $FWTM_{minor}$.

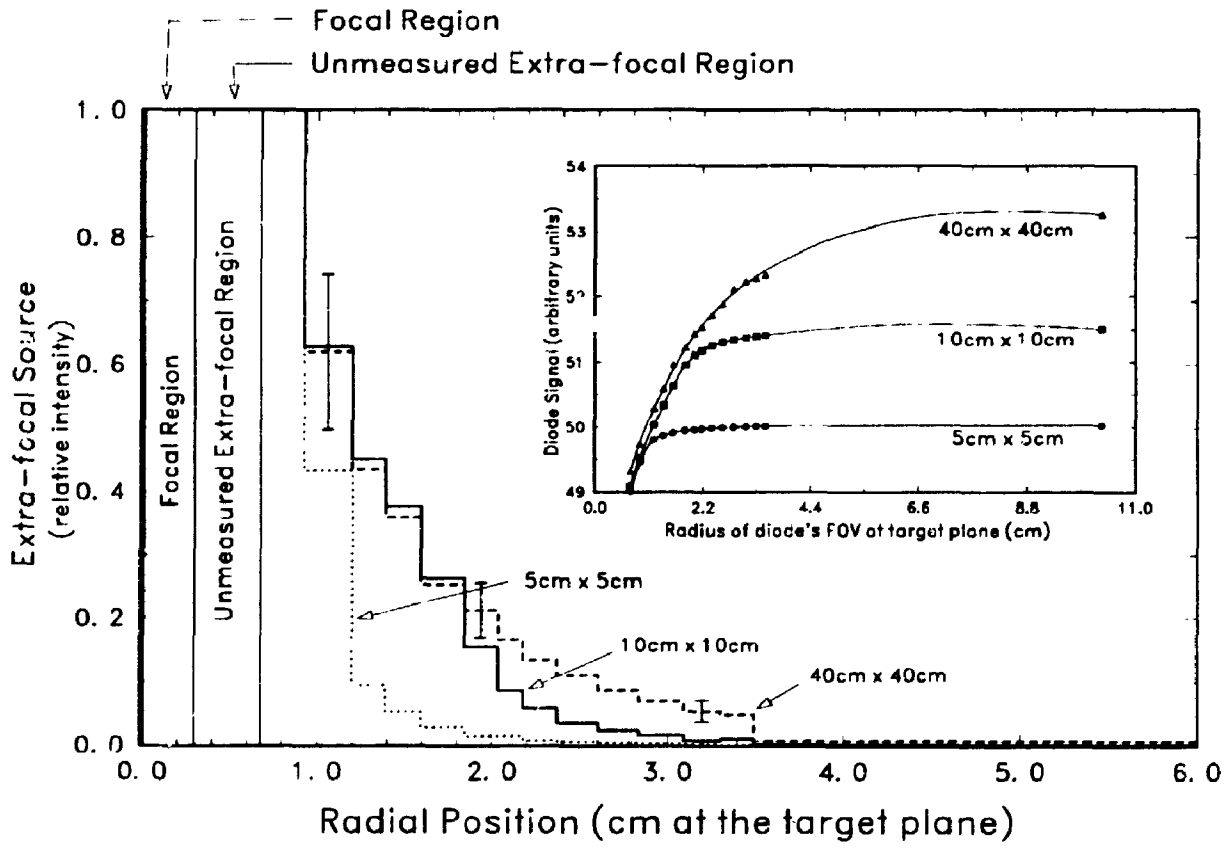

Figure 3.6 Extra-focal radiation for the Varian Clinac 2100c accelerator (6 MV beam). Differentiation of the data shown in the inset w r.t the area 'seen' at the target plane produces the plot in the main panel

all points in the radiation field, the focal spot of the Varian 2100c #2 accelerator (18 MV) was measured off the central axis and is shown in Fig. 3.4j. The same focal spot measured on the central axis is shown in Fig. 3.4f. The distributions have the same FWHM (1.4 mm) and shape (e = 1.2). The similarity of our two (2-D) distributions suggest that the 3-dimensional character of the source has a negligible influence on the apparent size or shape of the focal spot. Therefore, we conclude that the focal spot, as measured on the central axis, is representative of that which would be measured at other points in the x-ray field.

3.3.4 Extra-focal radiation: magnitude and distribution

The method described above has been used to estimate the magnitude and distribution of the extra-focal radiation produced by a Varian Clinac 2100c #2 (6 MV x-ray beam) for field sizes ranging from 1 cm x 1 cm to 40 cm x 40 cm field size (defined at 100cm SAD). Both the measured diode signal (corrected for room scatter and dark current) (Fig. 3.6 inset) and our estimate of the extra-focal radiation distribution for a 5 cm x 5 cm, 10 cm x 10 cm, and 40 cm x 40 cm field are shown in Fig. 3.6.

The graph in the inset of Fig. 3.6 shows that, as the aperture of the additional collimator is changed from its minimum to maximum value, the signal produced in the radiation diode changes by 8% for a 40 cm x 40 cm field size. This change is attributed to the increased fraction of the extra-focal radiation being viewed by the diode and represents the magnitude of the extra-focal radiation for the 40 cm x 40 cm field size. We believe that the value of 8 % for the magnitude of the extra-focal radiation is an *underestimate* because the dimensions of the radiation diode prevented the field-of-view at the target plane from being reduced to match the small size (2.2 mm, FWTM) of the

source focus. Therefore, the signal measured for the smallest collimator aperture (field viewed by the diode = 1.3 cm diameter) includes both the focal and some extra-focal radiation.

The corrected diode signal measurements in Fig. 3.6 (inset) are very similar to those published as output factors by Watts and Ibbott[12] for a Clinac-18 accelerator (10 MV beam), which has a head design similar to the Clinac 2100c.* Correcting their measurements for radiation backscatter into the monitor chamber results in a change in the output factor of ~9.3 % when changing the secondary collimators from a 4 cm x 4 cm to a 35 cm x 35 cm field size. The difference between our results and those of Watts and Ibbott can be attributed to the differences in the field-of-view at the flattening filter for the smallest field size setting. For the 4 cm x 4 cm field size, the ionization chamber used by Watts and Ibbott would have had a field-of-view at the target plane of approximately 0.8 cm x 1.4 cm, which is smaller than the smallest field-of-view obtained in our measurements (1.4 cm in diameter). Therefore, our results are in substantial agreement with the results of Watts and Ibbott.

The distributions of the extra-focal radiation for the 5 cm x 5 cm , 10 cm x 10 cm and 40 cm x 40 cm field sizes are shown in Fig. 3.6 and were obtained using the technique described in Section II.B. For all field sizes, the majority of the extra-focal radiation is emitted from the region approximately 7.0 cm in diameter at the target plane. Combining these results with our study of the focal spot on the same accelerator (6 MV) reveals that *the x-ray source consists of a very small (2.2 mm FWTM) focal region surrounded by a low intensity, broadly distributed, extra-focal region.*

---

* C. Huntzinger, Varian Associates Inc., Palo Alto, CA., USA (Personal Communication)

3.3.5 Source MTFs

The source MTFs corresponding to the focal spot alone for each of the accelerators we investigated are shown in Fig. 3.7. These source MTFs *do not include* any extra-focal considerations. The source MTFs were calculated using the technique described in section II.C. and the frequency axes were scaled to correspond to an image magnification of 1.2. Only the source MTFs corresponding to the major (7a) and minor (7b) axes of the source are shown. Since all the source MTFs for the Clinac 2100c accelerators are similar, they have been displayed as hatched regions. This figure shows that only those accelerators with the smaller focal spots (e.g., Siemens KD-2, 6 MV; Therac-25 #1 & #2, minor axes) will produce MTFs which are above zero at spatial frequencies in excess of 10 mm^{-1} at a magnification of 1.2. For the same magnification, the larger focal spots (e.g., Therac-6 #1 & #2; Therac-25 #1 & #2, major axis; Clinac 600c) have MTFs which are less than 0.1 at spatial frequencies above 1.8 mm^{-1}.

The effect of extra-focal radiation on the source MTF for the Varian Clinac 2100c (6 MV) accelerators is shown in Fig. 3.8 for a 40 cm x 40 cm field size. The extra-focal radiation reduces the source by a constant factor (~8%) for the range of spatial frequencies shown in Fig. 3.8. This factor corresponds to the fraction of primary fluence originating from the extra-focal region for the 40 cm x 40 cm field size. The visual impact of this low-frequency drop would most likely be perceived as a reduction in contrast rather than spatial resolution.

It should be emphasized that the size of the x-ray source (focal and extra-focal), as seen from the imaging plane, will vary with field size because the secondary collimators occlude parts of the extra-focal region of the source. Therefore, the source MTF will

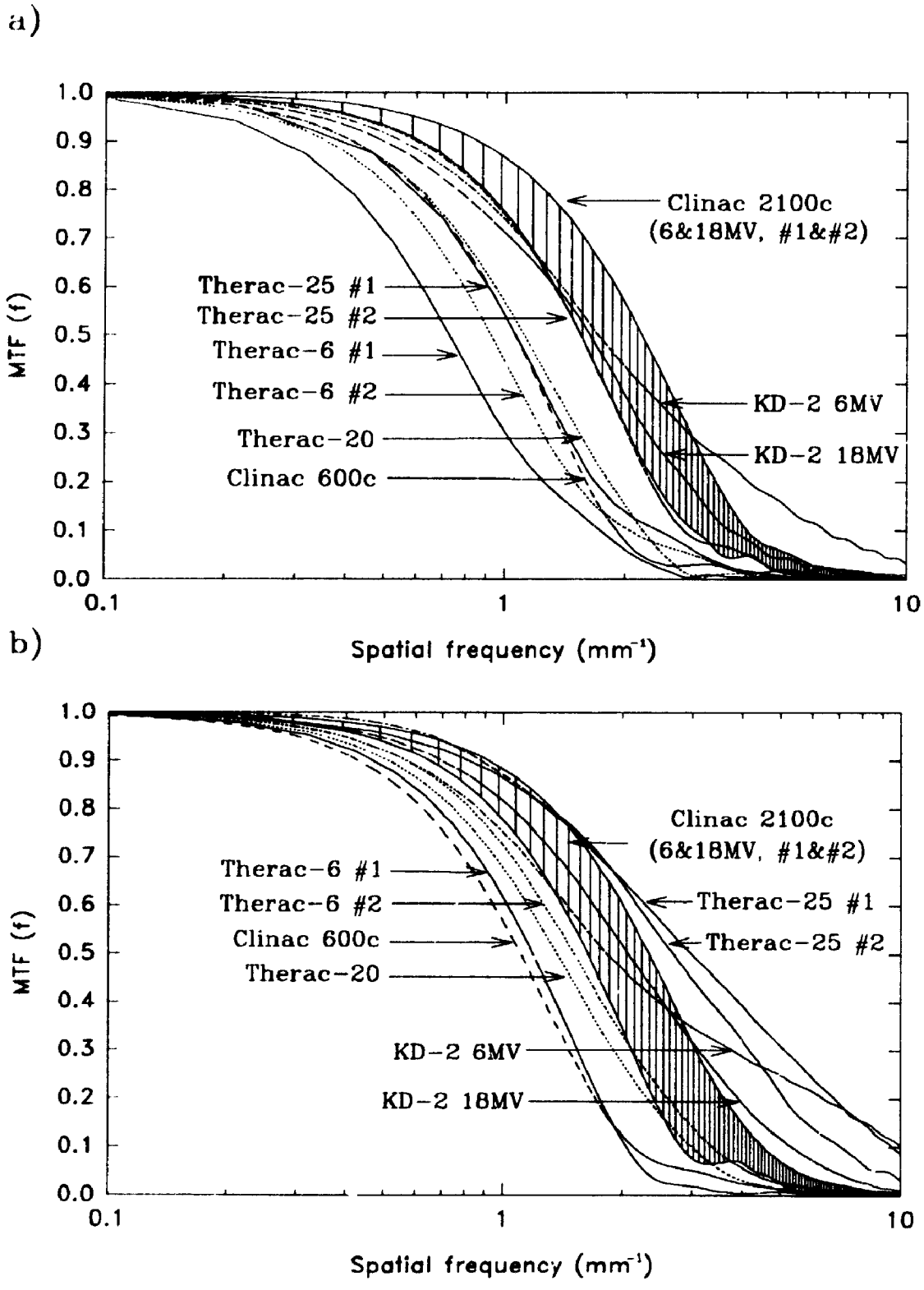

Figure 3.7 Source MTFs corresponding to the (a) major, and b) minor axes of the medical linear accelerator focal spots

change with field size. The results shown in Fig. 3.8 represent the two extremes for the source MTF (Clinac 2100c #2; 6 MV) corresponding to small fields (no extra-focal radiation) and large fields (maximum extra-focal radiation). From these results, it is clear that image quality would be expected to decline with increasing field size.

3.4 Discussion

3.4.1 Focal Spots

Our study of the focal spots of medical linear accelerators revealed a number of findings. The results from two Varian Clinac 2100c accelerators presented an opportunity to draw some general conclusions on the size and shape of focal spots in these machines. Surprisingly, the long term stability of the focal spots, in each of these accelerators, appears to be very high. Over the two year period of our study, the size and shape of the focal spots for the 2100c accelerators [Fig. 3.4(a-g)] changed only marginally. This was despite the fact that both accelerators were in daily use over the two year period and some components of accelerator #1 had to be altered or replaced, including the x-ray target and energy switch. For these accelerators, the size and shape of the focal spots appear to be determined predominantly by the accelerator design and influenced only modestly by tuning adjustments. The results for the Therac 25 and Varian Clinac 600c (4 MV) accelerators support this belief. The electron gun of the Therac 25 has a long, narrow filament which acts as an elongated electron source. The highly asymmetric shape of the electron cloud emitted from the filament is maintained as the electrons are accelerated through a complex beam transport assembly (which includes both a 180 degree and a 270 degree bending magnet)[23] resulting in a highly elongated x-ray focal

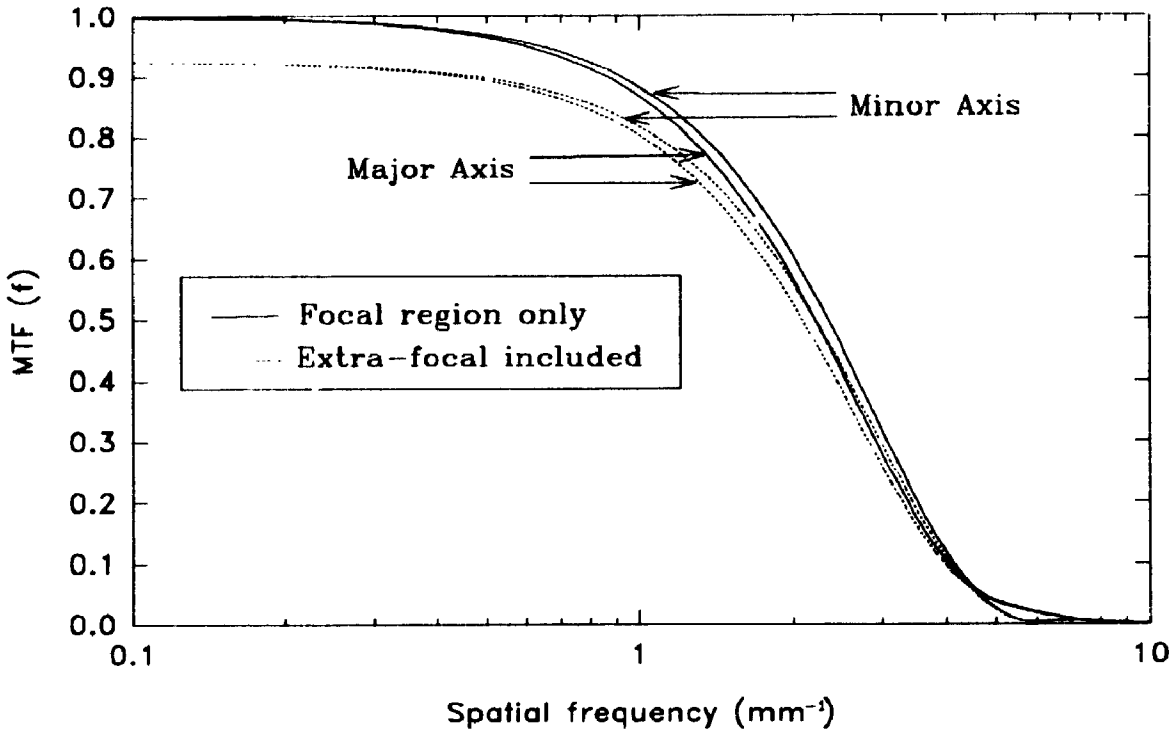

Figure 3.8 The extra-focal source introduces a low-frequency drop in the source MTF. Since the apparent size of the extra-focal source changes with field size, so will the source MTF.

spot. On the other hand, the 600c accelerator, which has an extremely simple beam transport assembly consisting of a straight-ahead accelerator section with no bending magnets, has a highly symmetric focal spot [Fig. 3.5e]. Since there are no bending magnets, the electron cloud cannot be preferentially focused along any one axis, thus a symmetric distribution is observed. Furthermore, the absence of the bending magnet results in a more diffuse electron cloud striking the x-ray target, giving rise to a focal spot which has a larger fraction of its emission at the periphery. It is not reasonable to suggest that the size and shape of the focal spot is independent of the tuning of the accelerator, since it has been shown that the tuning can influence the shape of the focal spot[9]. However, our current experience suggests that once an accelerator has been tuned to deliver clinically acceptable radiation beams, the accelerator design is the predominant factor in determining focal spot size and shape. The improvements to the mechanical rigidity of our focal spot measurement apparatus has revealed that the focal spots in a dual-energy accelerator are not necessarily coincident. The 6 and 18 MV focal spots of the Varian Clinac 2100c #2 were found to be shifted relative to each other by approximately 0.8 mm. While a 0.8 mm shift is not large in comparison to the scale of the treatment geometry, it is greater than half the width of the focal spot itself! Furthermore, such a shift represents up to a 2 mm displacement in position of the treatment field at the isocentre. The relative shift in source position permits accurate alignment of the light field with only one of the two x-ray beams. Such a shift in focal spot position may be a concern for certain clinical treatments, such as stereotactic radiosurgery, where small treatment fields are used.

3.4.2 Extra-focal radiation

Our results show that the extent of the extra-focal source distribution is limited by the secondary (beam defining) collimators. Therefore, the extra-focal radiation must be originating from points upstream of the secondary collimators, and not from the secondary collimators themselves. Several authors have attributed the change in *output factor* with increasing field size to changes in collimator scatter from the secondary collimators.[2,11-16] These changes in the output factor are more likely due to the variation in the amount of extra-focal radiation reaching the isocentre. Based on our findings, we believe that the term "collimator scatter" is a misleading description of the non-focal portions of the x-ray source in medical linear accelerators. We suggest a more precise term might be "extra-focal scatter" or "extra-focal radiation".

We have shown that the x-ray source in a medical linear accelerator consists of two components: a "focal region" and an "extra-focal region". This phenomenon has been recognized by other authors, however, no measurements demonstrating the physical size and magnitude of the "extra-focal" radiation have been reported.[24,25] Our findings show that the size of the x-ray source changes with field size due to the partial occlusion (by the secondary collimators) of the extra-focal portion of the source. This observation has implications, not only for portal imaging as demonstrated by the source MTFs shown in Figs. 3.7 and 3.8, but also for treatment planning systems. All treatment planning systems assume that the size of the x-ray source remains constant as a function of field size. In some treatment planning algorithms, a compromise has to be made in how accurately profiles for both the large and small field sizes are modelled. In other treatment planning algorithms a number of factors can be manipulated (e.g. collimator transmission[26] or backscatter[27]) in order to account for the penumbral differences between large and small field sizes. Our results suggest that a simple and intuitive x-ray source model which

consists of a high-intensity, field size-independent component (focal spot) and a low-intensity field size-dependent component (extra-focal) can improve the accuracy of treatment planning systems which model x-ray beam profiles.

3.5 Conclusion

A number of conclusions can be drawn from our study of medical linear accelerator x-ray sources.

(i) Quantitative measurements of medical linear accelerator focal spots on nine different accelerators showed that the size and shape of the source spot varies greatly between accelerators of different design. For accelerators of the same design, however, the source spots were found to be similar. This suggests that accelerator design is the most important factor in determining source spot size and shape, with adjustment of the beam transport parameters being less critical.

(ii) Our study of two Varian Clinac 2100c accelerators suggests that the long term stability in the size and shape of the focal spots, for an individual accelerator, appears to be very high, despite two years of daily use and replacement of components in the x-ray production assembly.

(iii) The positions of the two focal spots in a dual-energy accelerator are not necessarily coincident.

(iv) Despite the 3-dimensional nature of the target, the focal spot, as measured on the central axis, is representative of that which would be measured at all other positions in the x-ray field.

(v) The magnitude and distribution of extra-focal radiation for a Varian Clinac 2100c accelerator (6 MV beam) has been found to account for in excess of 8% of the

output of the accelerator. The majority of the extra-focal radiation originates from a circular region 5 cm in diameter (at the target plane).

(vi) The limiting resolution (i.e., 10% modulation) of the source MTFs range by a factor of 5 from 1.8 to 10 mm^{-1} for the source spots of the medical linear accelerators studied. The extra-focal radiation produces a low-frequency drop in the source MTF, which reduces the source MTF over the entire frequency range. Since the magnitude of this drop increases with field size, it is clear that image quality will decrease with increasing field size.

References

+ Now serviced through Theratronics International Ltd., Kanata, ON

1. H.E. Johns and J.R. Cunningham, *The Physics of Radiology*, 4th ed. (Thomas, Springfield, IL, 1983).

2. F. Kahn, *The Physics of Radiation Therapy* (Williams and Wilkins, Baltimore, MD, 1984).

3. J.M. Wilkinson, J.A. Rawlinson and J.R. Cunningham, "An extended source model for the calculation of the primary component of a Cobalt-60 radiation beam in the penumbral regions," Presented at the AAPM Meeting, Washington, D.C. (1970)

4. R.F. Wagner, K.E. Weaver, E.W. Denny, and R.G. Bostrom, "Toward a unified view of radiological imaging systems, Part I: Noiseless Images," Med. Phys. **1**, 11-24 (1974)

5. R.T. Droege and E.P. Cytacki, "The significance of screen resolution in treatment verification," Int. J. Radiat. Onc. Biol. Phys. **8**, 873-877 (1982)

6. W. Swindell, E.J. Morton, P.M. Evans and D.G. Lewis, "The design of megavoltage projection imaging systems: Some theoretical aspects," Med. Phys. **18**, 855-866 (1991)

7. W.R. Lutz, N. Maleki, and B.E. Bjarngard, "Evaluation of a beam-spot camera for megavoltage x rays," Med. Phys. **15**, 614-617 (1988)

8. E. Loewenthal, E. Loewinger, E. Bar-Avraham and G. Barnea, "Measurement of the source size of a 6- and 18-MV radiotherapy linac," Med. Phys. **19**, 687-690 (1992)

9. P. Munro, J. A. Rawlinson, and A. Fenster, "Therapy imaging: Source sizes of radiotherapy beams," Med. Phys. **15**, 517-524 (1988)

10. R. Mohan, C. Chui, and L. Lidofsky, "Energy and angular distributions of photons from medical linear accelerators," Med. Phys. **12**, 592-597 (1985)

11. A. Ahnesjo, T. Knoos, and A. Montelius, "Application of the convolution method for calculation of output factors for therapy photon beams," Med. Phys. **19**, 295-301 (1992)

12. D.L. Watts and G.S. Ibbott, "Measurement of beam current and evaluation of scatter production in an 18-MeV accelerator," Med. Phys. **14**, 662-664 (1987)

13. H. Kubo, "Telescopic measurements of backscattered radiation from secondary collimator jaws to a beam monitor chamber using a pair of slits," Med. Phys. **16**, 295-298 (1989)

14. G. Luxton and M.A. Astrahan, "Output factor constituents of a high-energy photon beam," Med. Phys. **15**, 88-91 (1988)

15. K.R. Kase and G.K. Svensson, "Head scatter data for several linear accelerators (4-18 MV)," Med. Phys. **13**, (1986)

16. M.S. Patterson and P.C. Shragge, "Characteristics of an 18 MV photon beam from a Therac 20 Medical Linear Accelerator," Med. Phys. **8**, 312-318 (1981)

17. P-H. Huang, J. Chu and B.E. Bjarngard, "The effect of collimator backscatter radiation on photon output of linear accelerators," Med. Phys. **14**, 268-269 (1987)

18. D.A. Jaffray, P. Munro, J.J. Battista and A. Fenster, "Activity distribution of a cobalt-60 teletherapy source," Med. Phys., **18**, 288-291 (1991)

19. R. H. Huesman, G. T. Gullberg, W. L. Greenberg, and T. F. Budinger, "Donner Algorithms for Reconstructive Tomography Users Manual," Lawrence Berkeley Laboratory Publication No. 214 (1977)

20. R. F. Wagner, K. E. Weaver, E. W. Denny, and R. G. Bostrom, "Toward a unified view of radiological imaging systems, Part I: Noiseless Images," Med. Phys., **1**, 11-24 (1974)

21. R. Waggener and W. McDavid, "Transmission computed tomography system components," *Medical Physics of CT and Ultrasound: Tissue Imaging and Characterization*, Ed. by G.Fullerton and J. Zagzebski, AAPM Monograph #6, 25-52, AIP, New York (1980)

22. H. H. Barrett and W. Swindell, *Radiological Imaging: The Theory of Image Formation, Detection, and Processing (Vol. 1)*, (Academic Press, New York, NY, 1981), 59

23. C.J. Karzmark, "Advances in linear accelerator design for radiotherapy," Med. Phys. **11**, 105-120 (1984)

24. T.C. Zhu, B.E. Bjarngard, and H. Shackford, "Analysis of components of the head-scatter factor for megavoltage photon beams," Med. Phys. **19**, 1138, (1992) (abstract)

25. P. Dunscombe and J.M. Nieminen, "On the field size dependence of relative output from a linear accelerator," Med. Phys. **19**, 1441-1444 (1992)

26. User's Manual, Theraplan V04B, Theratronics International Ltd., Kanata, ON

27. J. van de Geijn and R.W. Miller, "A new description of the photon beam peak-depth profile as a function of field size," Med. Phys. **13**, 904-907 (1986)

Chapter 4. X-RAY SCATTER IN MEGAVOLTAGE TRANSMISSION RADIOGRAPHY: PHYSICAL CHARACTERISTICS AND INFLUENCE ON IMAGE QUALITY[a]

Abstract

The physical characteristics of x-rays scattered by the patient and reaching the imaging detector, as well as their effect on verification (portal) image quality were investigated for megavoltage (0.1MeV-20MeV) x-ray beams. Monte Carlo calculations and experimental measurements were used to characterize how the scatter and primary fluences at the detector plane were influenced by scattering geometry and the energy spectrum of the incident beam. The calculated scatter fluences were differentiated according to photon energy and scattering process. Scatter fractions were measured on a medical linear accelerator (Clinac 2100c, 6MV) for a typical imaging geometry using an ionization chamber and a silicon diode. After correction for the energy dependence of the chamber and diode, the scatter fractions generated by the Monte Carlo simulations were found to be in excellent agreement with the measured results. In order to estimate the effect of scatter on image quality, the scatter and primary signals (i.e. energy deposited) produced in five different types of portal imaging detectors (lead plate/film, storage phosphor alone, lead plate/storage phosphor, Compton recoil-electron detector, and a copper plate/Gd_2O_2S phosphor) were calculated. The results show that, for a specified geometry, the scatter fraction can vary by an order of magnitude, depending on the sensitivity of the imaging detector to low-energy (< 1 MeV) scattered radiation. For a

[a] This chapter has been accepted for publication in *Medical Physics*, **21**(1), (1994). The title of the article is "X-ray scatter in megavoltage transmission radiography: Physical characteristics and influence on image quality" by D.A. Jaffray, P. Munro, A. Fenster, and J.J. Battista.

common portal imaging detector (copper plate/Gd_2O_2S phosphor), the scattered radiation (i) reduced contrast by much as 50% for a fixed display-contrast system, and (ii) decreased the differential-signal-to-noise ratio (DSNR) by 10-20% for a quantum noise-limited portal imaging system. For currently available TV camera-based portal imaging systems, which have variable display contrast, the reduction in DSNR depends on the light collection efficiency and the noise characteristics of the TV camera. Overall, these results show that scattered radiation can reduce contrast significantly in portal films while deteriorating image quality only moderately in on-line systems.

4.1 Introduction

In transmission radiography, the x-rays reaching the detector plane consist of unscattered (primary) and scattered components. While the primary fluence contributes to the signal in the resulting image, the scatter fluence can reduce contrast and introduce additional noise. In order to estimate the influence of scattered radiation on image quality, the physical characteristics of the scattered radiation must be known.

While many studies of scatter have been performed for the kilovoltage x-ray energies used in diagnostic radiology[1,2,3], there are few reports describing scatter fractions or scatter spectra for the megavoltage x-ray energies used in verification (portal) imaging. Droege et al.[4] have measured scatter-to-primary dose ratios at megavoltage energies for film and various thicknesses of lead buildup. However, their results have large uncertainties because they do not account for changes in primary beam fluence with changing field size (output factors) when determining the primary component. In addition, the scatter doses reported in their study contain signal generated by both x-ray scatter and electron contamination. Clearly, experimental measurements of scatter are very important, but are very difficult to carry out. Detailed studies of x-ray scatter at diagnostic energies have shown that the Monte Carlo method is the most successful method of studying x-ray scatter.[1] Barnea and Dick have used Monte Carlo simulations to examine x ray scatter fractions for industrial radiography (30 keV-20 MeV).[5] They have investigated the dependence of scatter on incident photon energy, atomic number of scattering medium, and imaging geometry. However, their work focuses on high atomic number materials (eg. iron) and provides little information for scattering by tissue-equivalent materials. In addition to their study of x-ray scatter, Barnea et al. also report on the number of electrons and positrons exiting the scattering medium. Swindell et al.[6]

have also performed a Monte Carlo study of x-ray scatter in which they consider Compton scattering only. Their simulations were performed for a restricted geometry and a 2 MeV monoenergetic incident beam; the influence of field size, patient thickness and polyenergetic spectra were not considered. In addition to their Monte Carlo study, Swindell et al. also provide an interpretation of the scatter fluences by presenting scatter-to-primary ratios (SPRs) in terms of signal variances. Since these variance calculations require knowledge of the spectral response characteristics of the imaging detector, a number of hypothetical detector response functions are also presented in their work. Overall, the studies to date provide some description of x-ray scatter at megavoltage energies, but do not present spectral information or isolate the processes responsible for the scatter fluence. In addition, the measured scatter fractions must be considered cautiously.

In this chapter, we present the results of both Monte Carlo calculations and experimental measurements which quantify x-ray scattering in low atomic number materials exposed to megavoltage photons. It should be noted that, in this paper, 'x-ray scatter' refers to scattered photons generated in the patient and not those originating from the head of the accelerator. Our Monte Carlo calculations yield the spectral distribution of primary and scatter x-rays for varying: (i) incident photon energy, (ii) thickness of scattering slab, (iii) field size, and (iv) air gap. The scatter spectra are categorised further to show the relative contributions from Compton and Rayleigh scattering, bremsstrahlung and positron annihilation. The calculated Monte Carlo fluences (scatter and primary) are compared with measurements made in a 6 MV x-ray beam. In addition to studying the physical characteristics of x-ray scatter reaching the imaging detector, we also investigate the relative magnitudes of the primary and scatter signals produced in five different x-ray

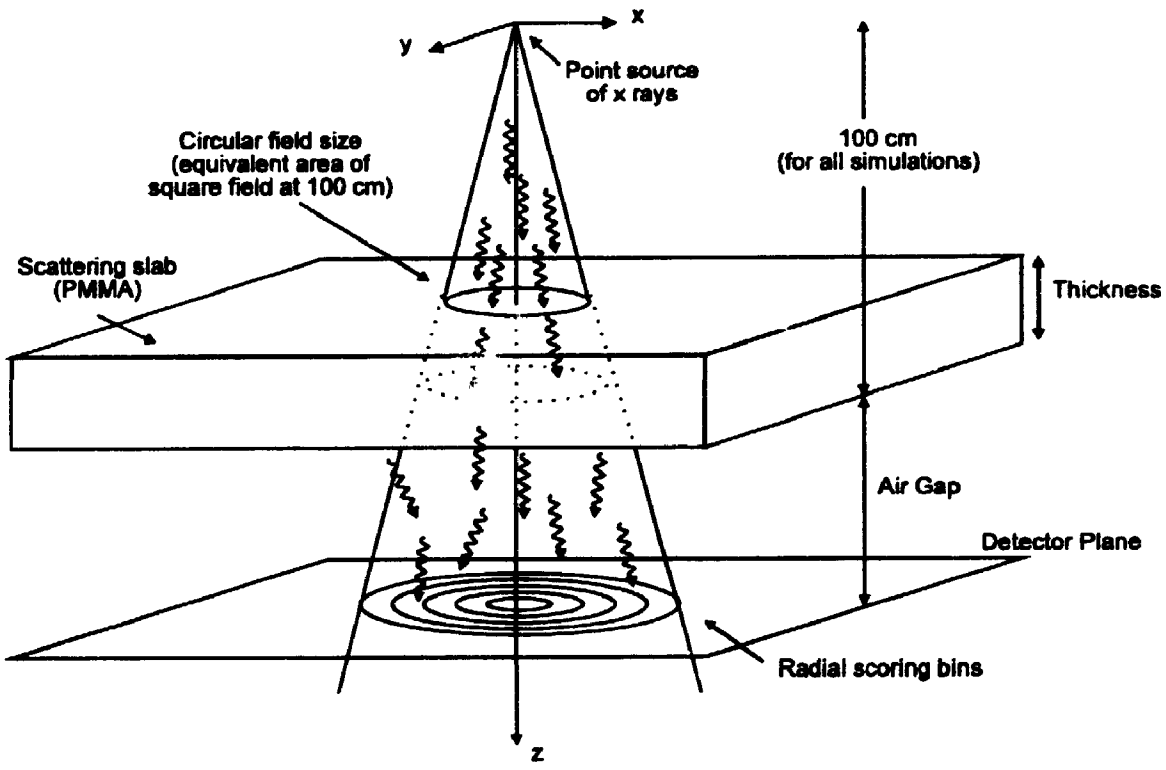

Figure 4.1 Diagram of the geometry used in the Monte Carlo simulations of x-ray scatter in megavoltage radiography The exit plane of the slab was fixed at 100 cm from the source

detectors: lead plate/film, lead plate/storage phosphor, storage phosphor alone, a Compton recoil-electron detector, and a copper screen/gadolinium oxysulfide phosphor combination. Using these results, we describe the detrimental effect of x-ray scatter on image quality in terms of a loss of contrast for fixed display contrast systems and in terms of a decrease in the differential signal-to-noise ratio (DSNR) for quantum noise limited systems. These studies provide information about the magnitude of x-ray scatter at megavoltage energies and the effect of x-ray scatter on verification (portal) image quality.

4.2 Materials and Methods

4.2.1 Monte Carlo Simulations of X-ray Scatter

4.2.1.1 Monte Carlo code

This study employs the EGS4 (Electron Gamma Shower) Monte Carlo code system, which has been tested extensively over the energy range under consideration here[7]. Since this code simulates coupled photon-electron(positron) particle transport, contributions from events such as bremsstrahlung and positron annihilation as well as Compton and Rayleigh scattering can be isolated.

A user code (SLAB) has been written for the EGS4 system which models the geometries found in portal imaging and scores *photon fluence (spherical)*[8] at the detector plane. The fluence at the detector plane is scored by summing the number of photons crossing the plane, weighted by $1/\cos\theta$, where θ is the angle the photon makes with respect to the normal to the plane (i.e. $\theta = 0°$ for normal incidence). To prevent $1/\cos\theta$

$\rightarrow \infty$ (i.e. θ=90°), a cutoff angle for this weighting was set at 85°.[7] The electron fluence reaching the detector plane is not scored.

The EGS4 code is used in its standard configuration[9] with only three modifications. We include the Parameter Reduced Electron Step Transport Algorithm (PRESTA).[10] PRESTA makes charged particle transport less dependent on user-selected parameters and decreases calculation times while retaining an accurate model of the physics of charged particle transport. The SLAB code also uses the improved sampling of the bremsstrahlung photon angular distribution, as developed by Bielajew et al.[11], as well as the improved radiative and collision stopping powers.[12,13]

4.2.1.2 Geometry of Monte Carlo simulations

The modelled geometry, shown schematically in Fig. 4.1, contains a point source which emits photons of specified energies into a cone of a designated half angle. The half angle is derived from the field radius at 100 cm from the source. The cone intersects a slab of scattering material which is perpendicular to the central axis of the beam. The scattering slab, which represents the patient in our geometry, can be located anywhere along the beam axis, has infinite lateral extent, finite thickness, and for these calculations was composed of poly-methyl-methacrylate (PMMA). PMMA was chosen as the scattering material in these simulations because its radiological properties are similar to those of water at megavoltage energies, and because the results of the simulations could be compared to the experimental measurements, directly. The "detector" plane can lie at any point beyond the bottom of the PMMA scattering slab and is divided into annular scoring rings. The photons detected in these rings are grouped according to (i) energy and (ii) history of the x-ray.

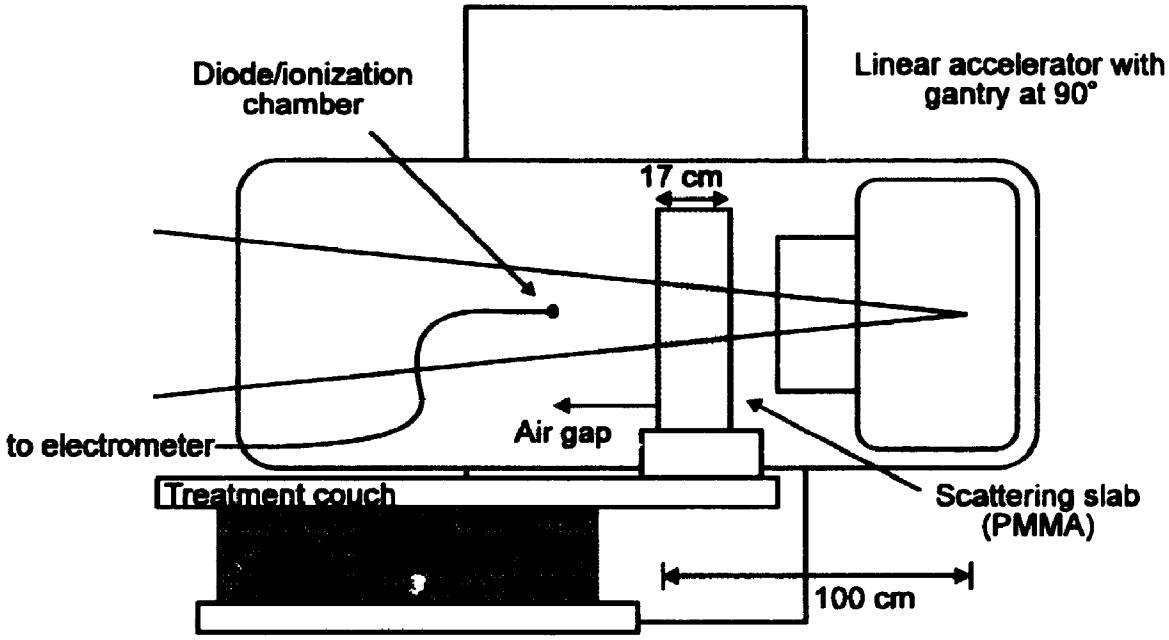

Figure 4.2 Diagram of the experimental setup used for measuring scatter fractions. The gantry was rotated to 90 degrees to eliminate backscattering from the floor of the treatment room.

Grouping according to x-ray history allows examination of the processes responsible for the scatter fluences. All scattered photons are classified as Compton unless they have undergone Rayleigh scattering or are produced through secondary processes such as bremsstrahlung or positron annihilation within the slab. Each of the Compton photons are further classified according to the number of Compton scattering events it has undergone before detection.

With the SLAB user code, the detected x-ray photons are scored according to the above categories for a variety of slab thicknesses (5-40 cm), field sizes (i.e. cone half angle), slab to detector distances (air gap), and incident photon x-ray energies (100keV - 20 MeV). The results of the Monte Carlo calculations are presented in the form of a scatter fraction, SF, which is defined as:

$$SF = \frac{\overline{\Phi_s}}{\overline{\Phi_s} + \overline{\Phi_p}} = \frac{\int \overline{\Phi'_s}(E)dE}{\int \overline{\Phi'_s}(E)dE + \int \overline{\Phi'_p}(E)dE} \qquad (4.1)$$

where $\overline{\Phi'_s}(E)$ and $\overline{\Phi'_p}(E)$ are the differential scatter and primary fluences (fluence/energy interval) in units of photons/m^2/MeV. The bars over these symbols denote that these values are estimated means of a random process. The scatter fluence refers to the contributions from all scattering processes: Rayleigh, Compton, bremsstrahlung and positron annihilation.

4.2.1.3 EGS4 transport and calculation parameters

The EGS4 Monte Carlo code has a number of parameters which control particle transport. PCUT and ECUT represent the minimum total (kinetic plus rest-mass) energy

of photons and electrons which are transported. AP and AE represent the energy thresholds for creation of secondary photons and electrons, respectively. For the simulations, we set PCUT=AP=10 keV and ECUT=AE=711 keV. An ECUT of 711 keV was chosen since it provided a significant decrease in calculation time while having a negligible effect on the contributions from the electron dependent processes (eg. bremsstrahlung). The user-adjustable parameters in PRESTA were left at their default values. In all simulations, the number of histories was sufficient to reduce the statistical uncertainty in the reported differential fluences to less than 5% in each bin. Typically, this required in excess of half a million incident photons (histories). The statistical uncertainties were estimated by dividing all calculations into 10 batches and computing the variance in the mean.[14] The simulations required 2 to 72 hours of CPU time on a Vaxstation 3200 (Digital Equipment Corporation, Maynard, Mass.), depending on the energy of the incident photon beam and the simulation geometry. The polyenergetic incident spectra used in our simulations were obtained from the papers of Kubsad et al. (6 MV) and Mohan et al. (24 MV).[15,16] These spectra were calculated by Monte Carlo modelling of x-ray production and transport in the head of a medical linear accelerator and, therefore, include the effects of scattering in the accelerator head.

4.2.2 Experimental Validation of Monte Carlo Simulations

4.2.2.1 Measurement technique

Measurements were made to confirm our Monte Carlo results using a medical linear accelerator (Varian 2100C, Palo Alto, Ca.) operated at 6 MV. Using the geometry shown in Fig. 4.2, measurements were made at a number of air gaps (10 cm to 70 cm)

and for a range of field sizes (1x1, 2x2, 3x3, 5x5, 10x10, 20x20, and 30x30 cm^2). These measurements were made using both a silicon diode with brass buildup cap (#2004, Theta Systems, USA) and an ionization chamber (PTW-N23323-2359) with a 4 cm diameter PMMA buildup cap connected to an electrometer (Capintec Model 192, Capintec, USA). The small outside diameter (7.8 mm) of the diode housing (which included the buildup cap) made it possible to make measurements at the small (1x1 cm^2) field sizes (Fig. 4.3a). Over the range of scatter geometries studied here, the relative response of the two detectors was found to be indistinguishable. Both the diode and ionization chamber had sufficient buildup to minimize signal due to electrons originating from within the scattering slab.

Two sets of raw data were acquired: one set with the scattering slab (17 cm of PMMA) in place, and the second set with the slab removed. The second set of data, which is a measure of incident beam fluence (output factor, cGy/monitor unit), corrects the first data set for changes in accelerator output with field size. This correction can be as large as 10% and is due to both changes in the amount of extra-focal radiation reaching the detector, as well as changes in the number of electrons backscattering into the beam monitoring chamber.[17] The corrected data describe the dependence of the total (scatter and primary) detector signal on field size and air gap, independent of variations in accelerator output.

Since we can only measure total signal, it must be separated into its scatter and primary components. This is done by extrapolating the measured data to a zero field size, where the scatter component, S, reduces to zero, leaving only the primary component, P. [18] The zero field size estimate was calculated by linearly extrapolating the signal values using the three smallest field size values (1cm x 1cm, 2cm x 2cm and 3cm x 3cm).

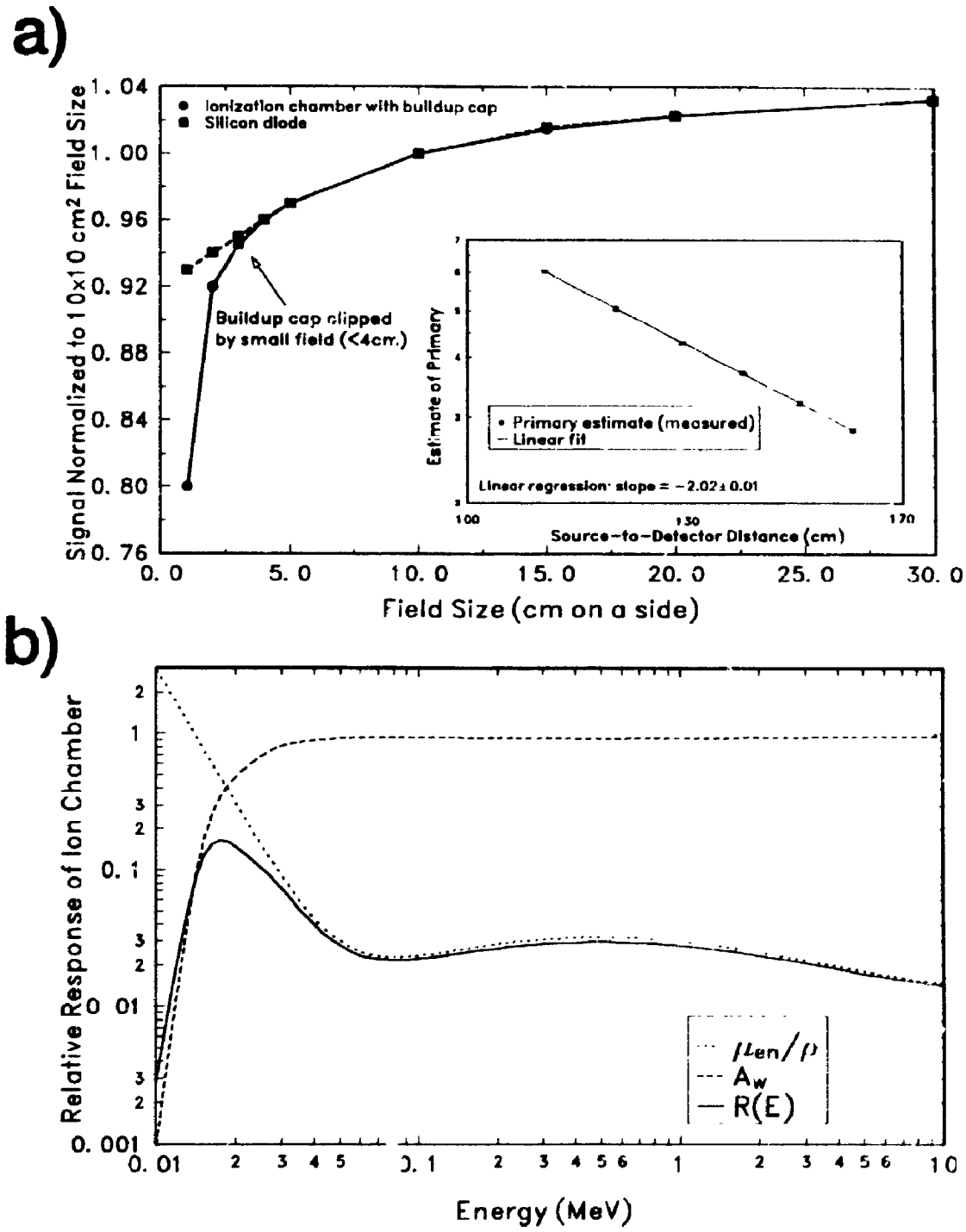

Figure 4.3 (a) Signal vs field size measured using (i) a Si diode (brass buildup) (square symbols), and (ii) a Farmer ionization chamber (PMMA buildup) (b) Estimated energy response of the ionization chamber

The error associated with the linear extrapolation (as calculated from the regression coefficients) was no larger than 0.2% for all air gaps. Subtracting the primary component from the measured data, T, yields the scatter signal, S. The scatter and primary components can then be presented as measured scatter fractions, SF_m, where:

$$SF_m = \frac{S}{S + P} = \frac{S}{T} \qquad (4.2)$$

Since the primary signal is similar in magnitude to the total signal for the small field sizes, the primary signal must be accurately known. To check our estimate of P (the primary signal), the extrapolated primary signal vs. source-detector distance was plotted on a log-log plot (inset, Fig. 4.3a). Since these measurements were made on a divergent beam, the primary signal should reduce as the inverse square of the distance to the source and thus produce a straight line on the log-log plot with a slope of -2. Figure 4.3a (inset) shows that the extrapolated values form a straight line with a slope of -2.02 indicating that the estimates of P are consistent with the geometry.

4.2.2.2 Ion chamber response

The Monte Carlo simulations estimate the *photon fluence*, while the experiments measure *signals* related to the energy deposited in the ion chamber (or silicon diode). Therefore, the Monte Carlo estimates of scatter and primary fluences must be converted from *fluence* to *signal* by estimating the response of the ion chamber to a broad range of x-ray energies. In this study, the signal is taken to be the energy deposited in the detector.

Provided the spectral response characteristics of a detector are known, the signal, $\overline{Q}$ (MeV), generated by the fluence incident on a detector is calculated as:[6]

$$\overline{Q} = A_d \int_E R(E)\,\eta(E)\,\overline{\Phi'}(E)\,dE \qquad (4.3)$$

where $\overline{\Phi'}(E)$ corresponds to either the primary or scatter fluence, A_d is the cross-sectional area of the detector, and $R(E)$ and $\eta(E)$ are the detector responsivity and quantum efficiency, respectively.[6] The quantum efficiency is the fraction of photons that interact in the detector and contribute signal (interacting fluence/incident fluence). The detector responsivity describes the amount of energy deposited per interacting photon (MeV/interacting fluence) and is assumed to be deterministic in this study.

The total response of a detector, $q(E)$, is the product of the responsivity and quantum efficiency, $R(E)\eta(E)$, and has units of energy/incident fluence [MeV m^2]. For the ion chamber, this was estimated to be:[19]

$$q(E) = R(E)\eta(E) = \left(\frac{\mu_{en}}{\rho}\right)\Big|_E \cdot \overline{S_{wall}^{air}} \cdot m_{detector} \cdot A_w\Big|_E \cdot E \qquad (4.4)$$

where $\left(\frac{\mu_{en}}{\rho}\right)\Big|_E$ is the mass energy absorption coefficient for the buildup cap material (PMMA), $\overline{S_{wall}^{air}}$ is the ratio of mass stopping powers (air to wall), $m_{detector}$ is the mass of

the detector, and $A_w|_E$ is a correction for the wall of the detector. Since the mass of the detector is constant and the ratio of mass stopping powers vary only slightly (assumed to be constant) over the energy range of interest[20] , they are not important for the final calculations, as they will be cancelled out when the scatter fraction is calculated.

The total response for the ion chamber depends upon two competing effects. The mass energy absorption coefficient represents the fraction of energy deposited in the chamber walls per unit incident energy fluence, which decreases with increasing energy over the range studied here. The wall correction, A_w, accounts for the attenuation (and scattering) of incident photons in the wall/cap of the ion chamber. Its value increases with increasing energy. A_w is calculated using the mass-energy absorption coefficient as an approximation of the broad-beam attenuation coefficient.[21] An estimate of the response of our ionization chamber with a 4 cm diameter PMMA buildup cap is shown in Fig. 4.3b. The coefficients used in calculating the response function are from tabulated data[22].

Employing this estimate of ion chamber (diode) response, the primary and scatter signals were calculated from the Monte Carlo estimated fluences, $\overline{\Phi'(E)}$, using Eq. 4.3. The resulting scatter fractions were calculated as:

$$SF_{signal} = \frac{\overline{Q_s}}{\overline{Q_s} + \overline{Q_p}}. \qquad (4.5)$$

In this way, the scatter fractions calculated using the EGS4 Monte Carlo code could be compared directly with those measured using the ionization chamber and diode.

4.2.3 Calculation of scatter fractions for typical imaging detectors

While our study of scatter describes the nature of the primary and scatter fluences reaching the detector, the impact of these fluences on image quality will depend upon the energy response of the imaging detector. To assess this dependence, the total response, $q(E)$, for five different imaging detectors have been studied. These detectors include: (i) a lead plate/Kodak AA film, (ii) a lead plate/storage phosphor, (iii) a storage phosphor alone, (iv) a Compton recoil-electron detector, and (v) a copper plate/gadolinium oxysulfide (Gd_2O_2S) phosphor screen. The response functions for (i), (ii), and (iii) have been obtained from the literature,[23,24] that of (iv) has been estimated analytically, and that of (v) has been determined from our own Monte Carlo simulations.

The lead plate/Kodak AA film detector consists of a sheet of Kodak AA film sandwiched between two lead plates, each 800 μm thick . The total response for this detector is based on Monte Carlo estimates of energy deposition in the front and back emulsions of the film and has been substantiated with experimental measurements.[23] Two Fuji storage phosphor detectors have also been considered, a standard (ST) storage phosphor (310 μm thick) mounted on an 800 μm thick plate of lead, and a high resolution (HR) storage phosphor (150 μm thick) with no additional metal plate. The response functions for these detectors have been estimated using Monte Carlo simulations and verified with experiment.[24] The fourth detector is a Compton recoil detector, as described by Swindell et al..[6] At the high energies found in verification imaging, where Compton interactions dominate, Swindell et al. suggest that the signal generated in the detector is proportional to the average energy imparted to the Compton recoil electron. In their implementation, Swindell et al. assume that the quantum efficiency of the detector is unity for all x-ray energies (i.e. $\eta(E) = 1$). The final detector consists of a 400 mg/cm^2 layer

of gadolinium oxysulfide (Gd_2O_2S) phosphor bonded to a 1 mm copper plate. This detector is typical of those found in TV camera-based portal imaging systems currently being developed by a number of vendors. The response function for this detector has been determined from Monte Carlo simulations which estimated the energy deposited within the phosphor per incident x-ray. The simulations modelled a pencil-beam of x-rays incident on the copper plate backed with phosphor. In order to model the energy deposition accurately, the particle transport parameters were set to PCUT=AP=10 keV and ECUT=AE=521 keV (10 keV kinetic energy). The value of ECUT used in these simulations is lower than that used in the x-ray scatter simulations; this was done to ensure proper modelling of electron transport within the relatively thin (1 mm) layers of the detector. The signals produced in the imaging detectors by the primary and scatter fluences were calculated using Eq. 4.3. The energy range considered in the signal calculations varied from detector to detector, depending on their sensitivity to low-energy photons. The HR storage phosphor and copper/Gd_2O_2S phosphor detectors are sensitive to lower-energy x-rays, therefore, the low-energy cutoffs for these two detectors were set to 10 and 50 keV, respectively. For the other three detectors, the low-energy cutoff was set at 100 keV. In addition to applying low-energy cutoffs in our calculations, it was necessary to extrapolate the response functions to the maximum x-ray energy in our study (24 MeV). For the storage phosphor detectors, the response functions were linearly extrapolated between 20 and 24 MeV. The response function for the 800 μm lead plate/Kodak AA film detector was only available for photon energies up to 10 MeV. For energies greater than 10 MeV, the response was assumed to be identical in shape to that reported for the 800 μm lead plate/storage phosphor detector. With the relative magnitudes of the scatter and primary signals determined for each of the five imaging

detectors, the corresponding scatter fractions were calculated using Eq. 4.5.

4.2.4 Estimating the effect of scatter on image quality

There are two major ways in which scattered x-rays reaching the detector plane can degrade image quality: (1) a reduction in contrast, and (2) a reduction in the differential signal-to-noise ratio (DSNR).

In the presence of scatter, the contrast of an object in the image is reduced. This loss in contrast is the result of the added background signal generated by the scatter fluence. The ratio of contrast in the presence of scatter to that in the no-scatter case is given by[25] (Appendix B)

$$\frac{C_s}{C_{ns}} = (1 - SF), \qquad (4.6)$$

where C_s and C_{ns} refer to the contrast in the scatter and no-scatter cases, respectively. The importance of this loss in contrast is dependent on the display characteristics of the imaging system. Systems which have a variable display contrast, such as a digital system, can compensate this loss in contrast by proper selection of display window and level. For fixed display systems, such as film, it is not possible to compensate for this loss. The loss in contrast due to scatter for the lead plate/Kodak AA film detector was calculated for both a 6 and 24 MV incident beam considering both a typical imaging geometry, and an extreme imaging geometry. The typical geometry examines a range of field sizes (5 x 5, 10 x 10, 15 x 15, 20 x 20 and 30 x 30 cm^2) incident on 17 cm of

PMMA with the detector at a 20 cm air gap. Under the extreme imaging geometry, the loss in contrast is examined as a function of air gap for a very thick (40 cm) scattering slab and a large (30 x 30 cm^2) field size.

In addition to increasing the background signal, the scatter fluence also adds x-ray quantum noise. This added noise reduces the DSNR. For a fixed dose to the patient, the loss in DSNR is calculated as (Appendix C),[2]

$$\frac{DSNR_s}{DSNR_{ns}} = \frac{1}{\sqrt{1+SPR}} \qquad (4.7)$$

where $DSNR_s$ and $DSNR_{ns}$ refer to the scatter and no-scatter cases. For the case of a detector which counts photons, the SPR term in Eq. 4.7 can be represented by the ratio of scatter and primary fluences. However, we follow the more general formalism described by Swindell[6] (i.e. one which accommodates polyenergetic spectra and energy dependant detector response) where the scatter-to-primary ratio, SPR, is defined as the ratio of the variances in the scatter and primary signals,[6]

$$SPR = \frac{\sigma^2_{Q_s}}{\sigma^2_{Q_p}}. \qquad (4.8)$$

In order to determine the variances, both the responsivity, $R(E)$, and quantum efficiency, $\eta(E)$, must be known individually. If these quantities are known, the variance can be calculated as follows,[6]

$$\sigma_Q^2 = A_d \int_E R^2(E)\eta(E)\overline{\Phi'}(E)dE. \qquad (4.9)$$

Swindell et al. also derive an expression for the increase in patient dose required to compensate for the loss in DSNR associated with the added scatter fluence. This 'scatter compensation factor' or SCF, is defined as:

$$SCF = \frac{D_{scatter}}{D_{no\ scatter}} = (1 + SPR), \qquad (4.10)$$

where $D_{scatter}$ and $D_{no\ scatter}$ are the doses to the patient required to maintain the same DSNR in the presence and absence of x-ray scatter. Since the responsivity, $R(E)$, and quantum efficiency, $\eta(E)$, were available for the Compton recoil-electron detector and the copper/Gd_2O_2S detector only, it was possible to calculate the loss in the DSNR and the SCF for these two detectors only. The calculations were performed for 5 x 5, 10 x 10, 15 x 15, 20 x 20 and 30 x 30 cm^2 field sizes for a standard geometry of 6 MV x-rays incident on a 17 cm thick slab of PMMA and a 20 cm air gap.

4.3. Results and Discussion

4.3.1 Dependence of Scatter on Incident X-ray Energy

4.3.1.1 Monoenergetic beams

Figure 4.4 shows the scatter and primary fluences reaching the central region of the detector plane as a function of monoenergetic incident x-ray energy irradiating the scattering slab. The scatter and primary fluences were obtained by summing over the energy spectra of the differential primary and scatter fluences reaching the detector plane. These fluences have been normalized to the incident fluence in the absence of the scattering slab. As expected, the primary fluence reaching the centre of the detector plane (0 cm < r < 2.5 cm) increases with increasing energy, from a few percent transmission at 100 keV to 72 % transmission at 20 MeV. In contrast, the scatter fluence changes in an unexpected fashion over the same energy range. It increases rapidly between 100 keV and 700 keV, falls moderately between 700 keV and 5 MeV and then increases slowly. These changes in scatter fluence with increasing energy (Fig. 4.4) are dependent on five factors: (1) the Compton cross-section decreases with increasing energy resulting in a decrease in the scatter fluence; (2) the incident high energy photons which *are* scattered are more forward directed and hence more likely to reach the detector; (3) these scattered photons are more energetic and therefore more likely to escape from the scattering object; (4) by increasing the incident energy, the energy of charged particles released (recoil electrons and positrons) in the scattering object also increases, resulting in a marked increase in the number of photons generated through the

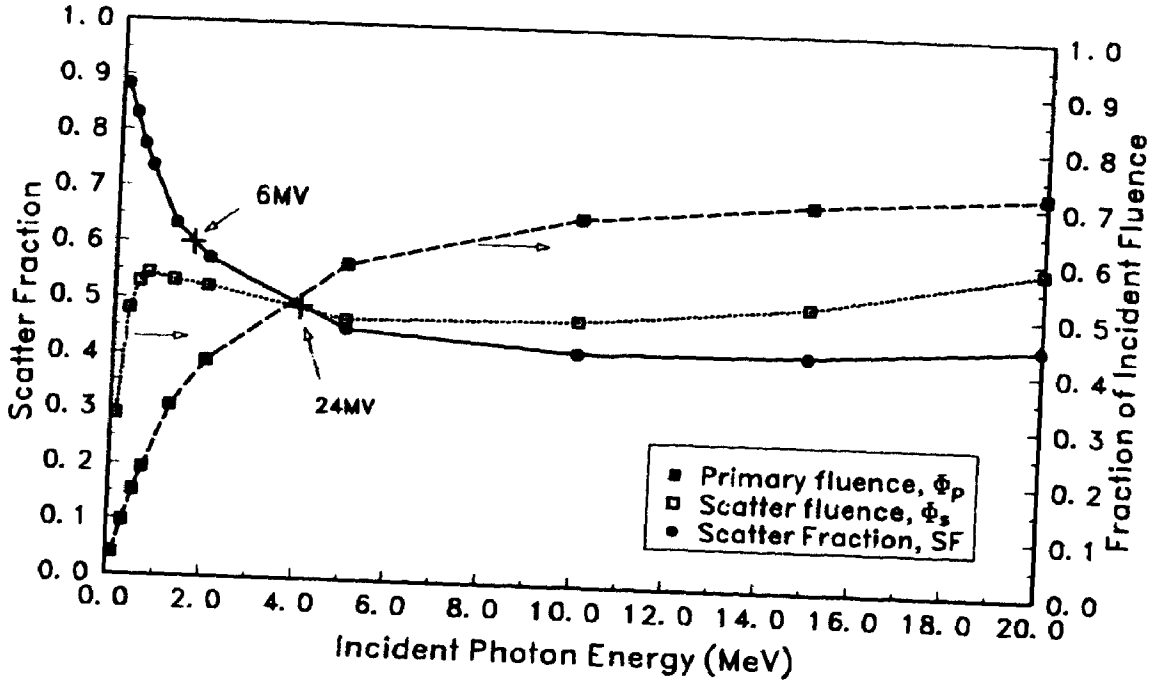

Figure 4.4 The dependence of scatter fraction (SF-Eq 4.1) on incident photon energy for a 17 cm PMMA slab and a 30x30 cm^2 field. (crosses - polyenergetic beams)

bremsstrahlung process; and finally, (5) at photon energies in excess of 1.022 MeV, positrons are generated within the slab through pair production, which, upon annihilation, contribute annihilation quanta to the scatter fluence. Factors 2 and 3 compensate for the fall in Compton cross-section (factor 1), resulting in a rise in scatter fluence and an increased fraction of 1st-scattered photons exiting the slab and reaching the detector. This is illustrated in Table 4.1. At 500 keV only 29 percent of Compton scattered photons which reach the detector are first-scattered photons compared to 66 percent at 20 MeV. Increasing the energy of the incident x-ray beam increases the energy of the first-scatter photons, and thus it is more probable that they will exit the slab. At these higher energies, the angle of scattering is also reduced making it more likely that the scattered photon will strike the detector. Factors 4 and 5 (bremsstrahlung and positron annihilation) are responsible for the gradual increase in scatter fluence as the energy of the incident x-ray beam is increased beyond 6 MeV.

The net effect of the changes in the primary and scatter fluences on the scatter fraction is shown in Fig. 4.4. The scatter fraction declines rapidly from 100 keV to 10 MeV and then increases slowly, this rapid decline is almost solely the result of a climb in primary transmission. Therefore, the change in scatter fraction at the energies of interest in verification imaging (500 keV - 10 MeV) is influenced more by rapid changes in *primary* transmission than by changes in scatter fluence.

Not only do the relative magnitudes of the scatter and primary fluences change with energy, so do the relative energies. Figure 4.5 shows relative primary and scatter fluence spectra for two monoenergetic photon beams ((a) 0.5 MeV and (b) 20 MeV) incident on a 17 cm PMMA slab, with an equivalent area field size of 30x30 cm^2. These

plots have been normalized to unit primary fluence in the absence of the slab. At 0.5 MeV (Fig. 4.5a), almost all the scatter is produced through Compton interactions, while the remainder is the result of Rayleigh scattering. Figure 4.5a shows that as the order (first, second, multiple) of the scatter increases, the average energy decreases. The scattered photons have a minimum energy threshold determined by the number of scattering events which the photons have experienced and the scoring geometry. For example, no first scatter photons of energy less than approximately 0.25 MeV can reach the detector for this geometry because the scattering angle would have to exceed 90 degrees. This minimum energy level serves as a check of the Monte Carlo calculations because it can be predicted analytically using the Compton energy-angle relationships.[26] At higher incident energies, pair production and bremsstrahlung events start making significant contributions to the scatter fluence reaching the detector. Figure 4.5b shows that for a 20 MeV incident photon beam, the scatter fluence is due largely to bremsstrahlung and positron annihilation photons. Although the term "scatter" does not strictly apply to these contributions, we will continue to refer to these components as scatter. For these higher incident energies, the energy of the scatter is very much lower than that of the primary. To examine the differences in energy between the scatter and primary spectra, we have plotted the mean energy of the scatter fluence versus the energy of the incident monoenergetic beam in Fig. 4.6. For a 0 cm air gap, at low energies (100 keV), the mean energy of the scatter (67 keV) is comparable to the energy of the primary. However, as incident x-ray energy is increased, the difference between the energy of the scatter and primary spectra becomes much more pronounced. For a 20 MeV monoenergetic incident x-ray beam, the mean energy of the scatter fluence is only 2 MeV. Overall, the difference

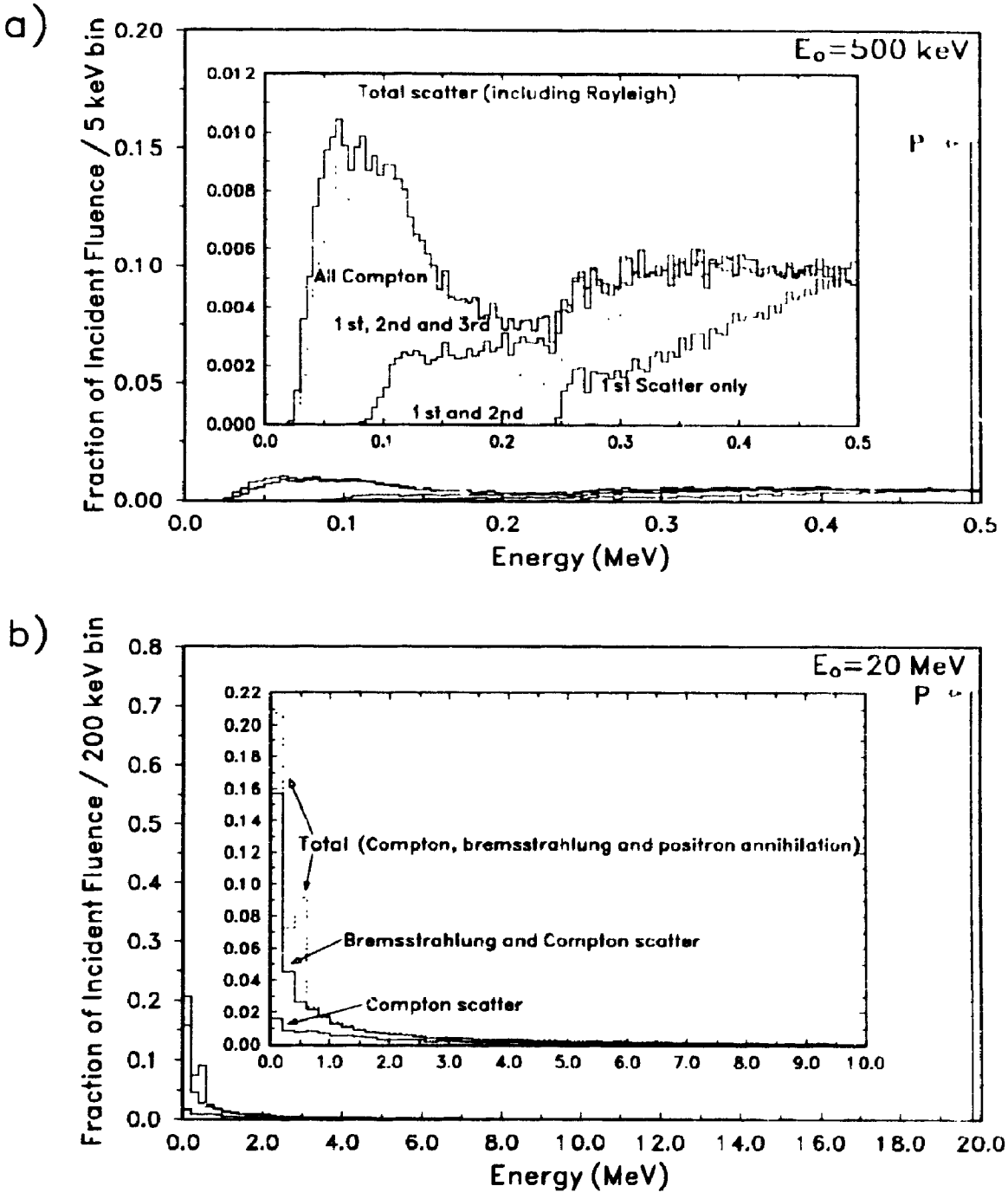

Figure 4.5 Incident, primary transmission, and scatter spectra for (a) 500 keV and (b) 20 MeV monoenergetic incident photons

in energy between the primary and resulting scatter fluences becomes more and more pronounced as the energy of the incident x-ray beam is increased. Increasing the air gap (Fig. 4.6) reduces the difference in energy between the primary and scatter. This is because the lower-energy components of the scatter fluence have a broader angular distribution.

4.3.1.2 Polyenergetic beams

The above studies of monoenergetic incident photon beams do not represent the

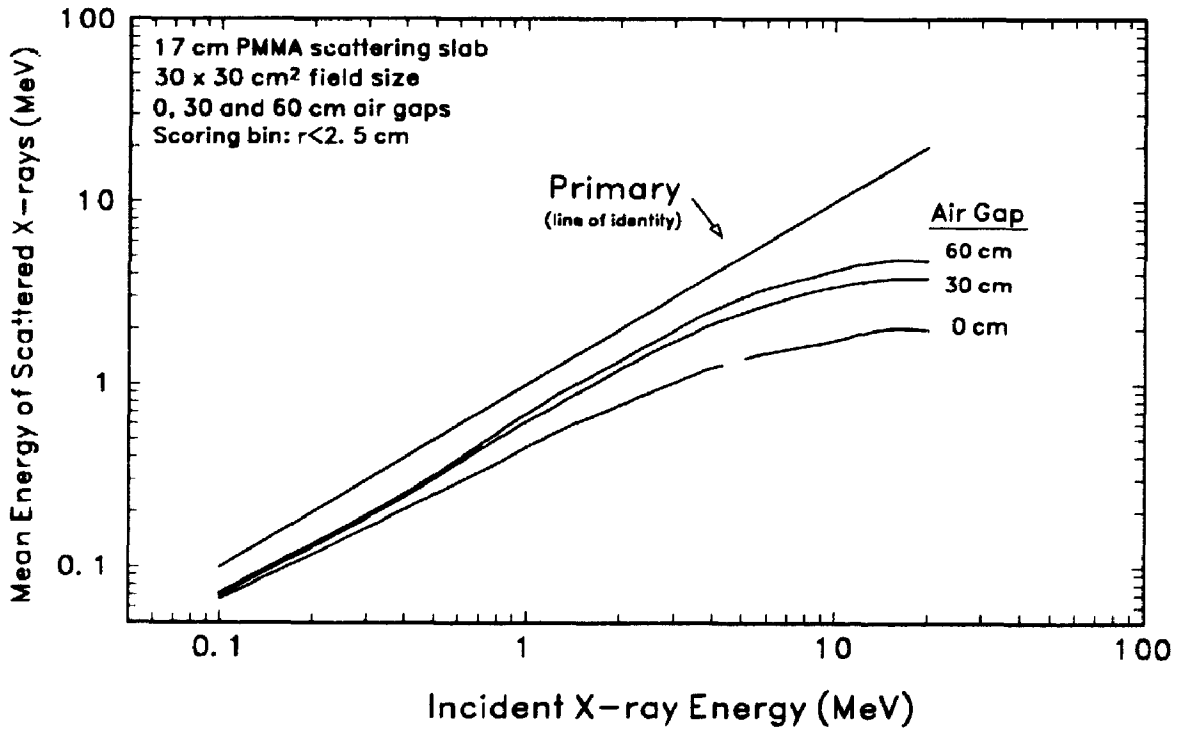

Figure 4.6 Mean energy of scatter fluence versus energy of incident x-ray beam (monoenergetic)

scatter that would be found in a polyenergetic radiotherapy beam from a medical linear accelerator. Figure 4.7 shows scatter spectra for 6 MV and 24 MV polyenergetic incident photon beams, using the same geometry as for the monoenergetic results shown in Fig. 4.5 (30 cm x 30 cm field size, 0 cm air gap, 17 cm thick scattering slab).

The incident, transmitted and scattered spectra are a composite of many monoenergetic beams, therefore, the trends for polyenergetic beams will be the same as those described above for the monoenergetic case. The low energy component of the incident spectra (0-4 MeV) produces the majority of the scatter through Compton scattering, while the high energy component produces low-order, high-energy scatter as well as bremsstrahlung and annihilation quanta (as shown in Fig. 4.5b). It is interesting to note that for a 24 MV (Fig. 4.7b) incident x-ray beam, the scatter fluence at energies below 240 keV is composed almost equally of Compton scattered x-rays and bremsstrahlung/annihilation quanta.

To demonstrate the influence of the broad spectra on scatter fraction, the scatter fractions for the 6 and 24 MV x-ray beams are plotted as crosses in Fig. 4.4. The 6 MV

Order of Scatter	Fraction of total Compton scatter fluence			
	500 keV	2 MeV	10 MeV	20 MeV
1	0.29	0.46	0.62	0 66
2	0.20	0 21	0 17	0 16
3	0.14	0 11	0.07	0 06
4+	0.37	0 22	0 14	0 12

Table 4.1 Order of Compton scattered photons reaching the detector for 500 keV, 2 MeV, 10 MeV and 20 MeV incident monoenergetic x-ray beams

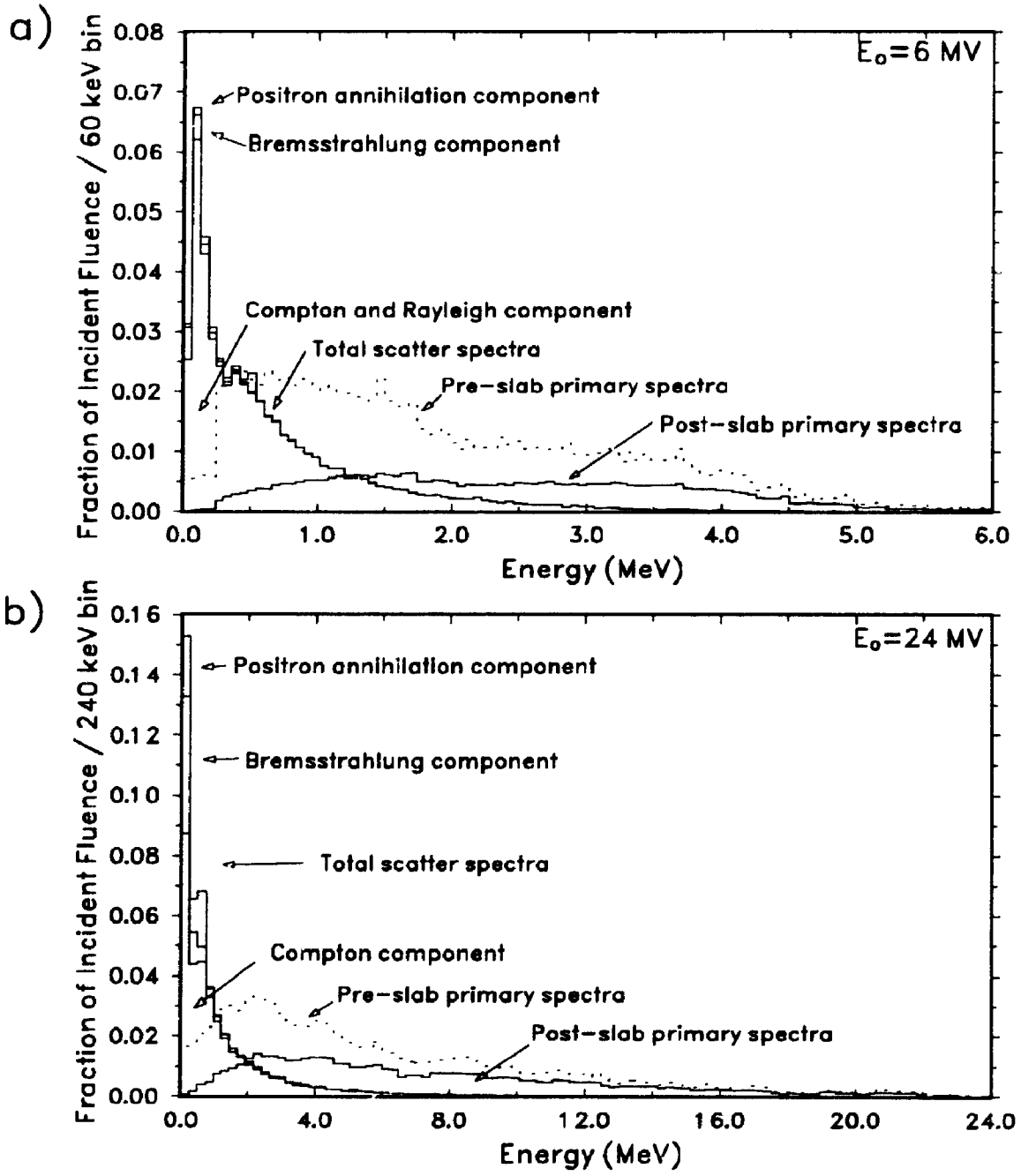

Figure 4.7 Incident, primary tranmission, and scatter spectra for (a) 6 MV and (b) 24 MV incident spectra.

and 24 MV beams have the same effective scatter fractions as that of a 1.6 MeV and 4 MeV monoenergetic beam, respectively.

4.3.2 Dependence of scatter fluence on geometry

The dependence of scatter fluence, primary fluence and scatter fraction on imaging geometry (field size, patient thickness, air gap) has been investigated for 6 and 24 MV clinical x-ray spectra.

Scattering slab thickness was varied between 5 cm and 40 cm while keeping the distance between the x-ray source and the exit surface of the slab fixed at 100 cm (Fig. 4.1). This kept both the detector position (relative to the x-ray source) and the air gap fixed for all thicknesses. For this study, a 30x30 cm^2 field size and an air gap of 30 cm (corresponding to an image magnification of approximately 1.3) were simulated. The results of the simulations are shown in Fig. 4.8a. Although the scatter fraction increases with increasing thickness, the scatter fluence eventually reaches a maximum and then starts to decline. This maximum depends on the energy of the incident photon beam and occurs at approximately 15 cm for 6 MV and 25 cm for 24 MV. The maximum also depends on the simulation geometry. For example, if a larger incident radiation field had been simulated, the peak in the scatter fluence would have occurred at a reduced slab thickness compared with those shown in Fig. 4.8a. Overall, the change in scatter fluence with slab thickness is small (for the slab thicknesses considered here) compared to the change in primary fluence. Therefore, the steady increase in scatter fraction is caused mainly by the decrease in primary transmission.

The effect of field size on the scatter fluence was studied for a 17 cm PMMA slab

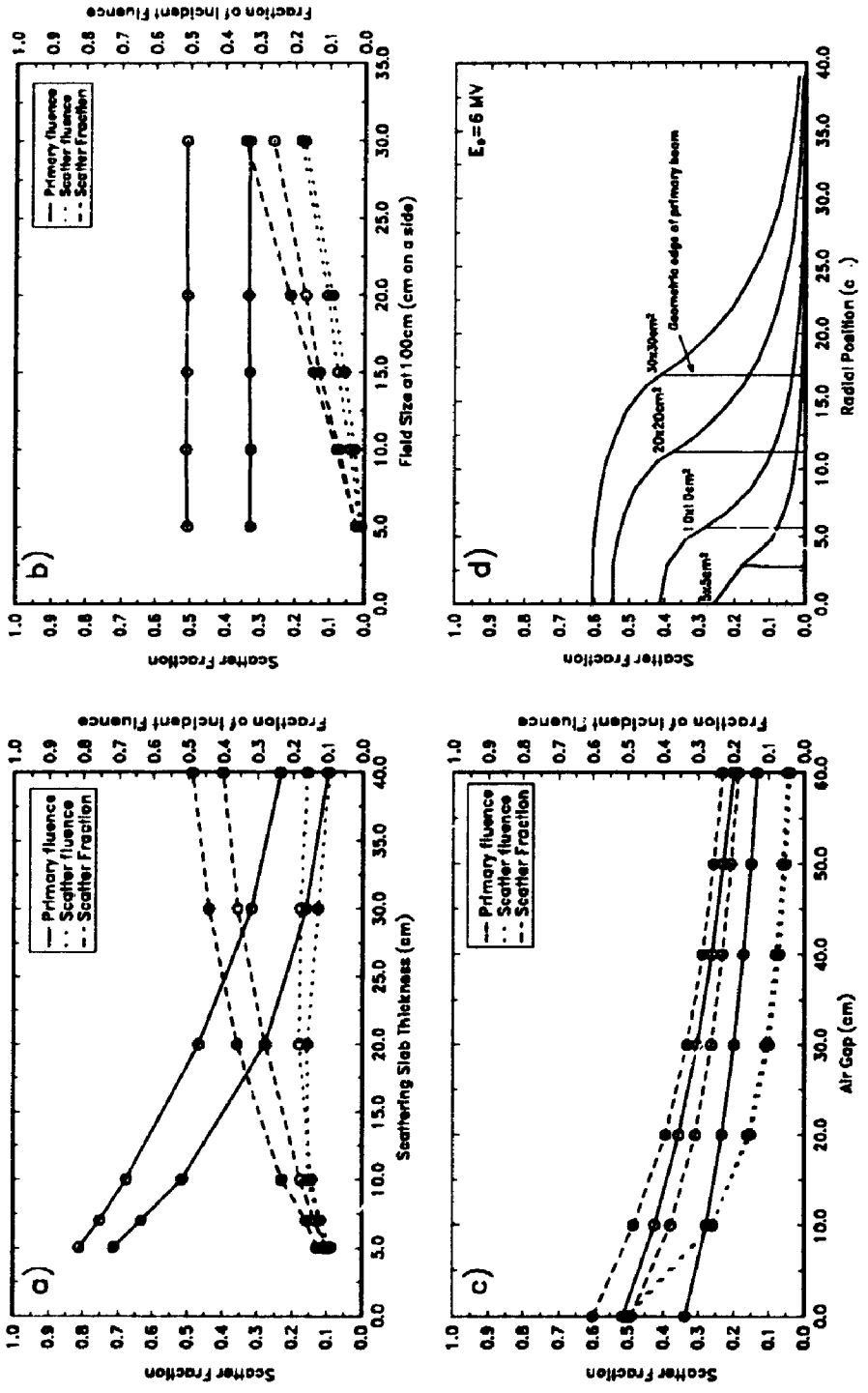

Figure 4.8 SF (Eq 4 1) vs geometry: (a)slab thickness (FS=30x30, AG=30cm), (b)field size (T=17cm, AG=30cm), (c)air gap (FS=30x30, T=17cm), (d)radial position (T=17cm, AG=0cm). [6MV-solid, 24MV -open]

thickness and an air gap of 30 cm. Since the cross-section of the incident beam modelled in our Monte Carlo simulations is circular, the square field sizes reported here are actually modelled as circular fields of equivalent area. Figure 4.8b shows the change in scatter and primary fluences and scatter fraction with field size. As expected, the primary fluence is independent of field size. However, the scatter fluence increases rapidly as the field size changes from 5 to 40 cm on a side. The scatter fractions of the 6 and 24 MV beams are different by almost 10 percent at large field sizes, however, the scatter fluences are almost identical. The difference in scatter fraction is a result of the higher primary transmission associated with the 24 MV beam.

Changing the air gap is the simplest and most effective way of reducing the scatter fraction. Figure 4.8c shows the changes in scatter fluence, primary fluence and scatter fraction over a range of air gaps for a 30x30 cm^2 field size and 17 cm of PMMA. The decrease in scatter fraction is caused by the decline in scatter fluence, which occurs more rapidly than the inverse square-law reduction of the primary fluence. This rapid decline is attributed to the broader angular distribution of the scattered x-rays. The scatter fluences for the 6 and 24 MV x-ray beams decrease similarily with increasing air gap. This is a surprising result, as one would expect the scatter fluence produced in the lower-energy beam (6 MV) to have a broader angular distribution and therefore, fall more quickly. However, at the higher energies considered here, the mean angle of the Compton scattered photon changes very little with increasing photon energy. For example, the mean energies for the 6 and 24 MV spectra are about 2 MeV and 6 MeV, respectively. Based on the Klein-Nishina expression for the Compton cross-section, the mean angle of a Compton scattered photon is 40° at 2 MeV and has only decreased to

30° at 6 MeV. This relatively small change in mean angle will not significantly alter the air gap dependence of scatter fluence, particularily for this geometry (i.e. fluence scored on the central axis and large [30 cm x 30 cm] field sizes).

The air gap influences not only the relative magnitude of the scatter and primary fluences but also influences the spectra of the scatter fluence. Figure 4.9 shows that the mean energy of the scattered photons reaching the detector increases with increasing air gap. This occurs because, as the air gap increases, the detector geometry discriminates increasingly against the lower-energy component of the scatter fluence, which has a broader angular distribution. Therefore, the air gap serves a dual-purpose; it reduces the magnitude of the scatter fluence reaching the detector plane and, it hardens the scatter spectra, filtering out the low-energy scattered photons. The combination of these two effects will be especially advantageous for those portal imaging detectors which have a low-energy sensitivity. The difference in energy between the scatter and primary fluences will have implications in the design of detectors and scatter rejection techniques for use at megavoltage energies.

4.3.3 Radial dependence of scatter fraction

The plot in Fig. 4.8d shows the radial distribution of x-ray scatter at the detector plane for a range of circular field sizes. These results correspond to an air gap of 0 cm for a 6 MV x-ray beam incident upon 17 cm of PMMA. Since the primary fluence falls to zero at the edge of the field (vertical lines), the scatter fraction at each radial position was calculated using the primary fluence as detected on the central axis. This estimate of

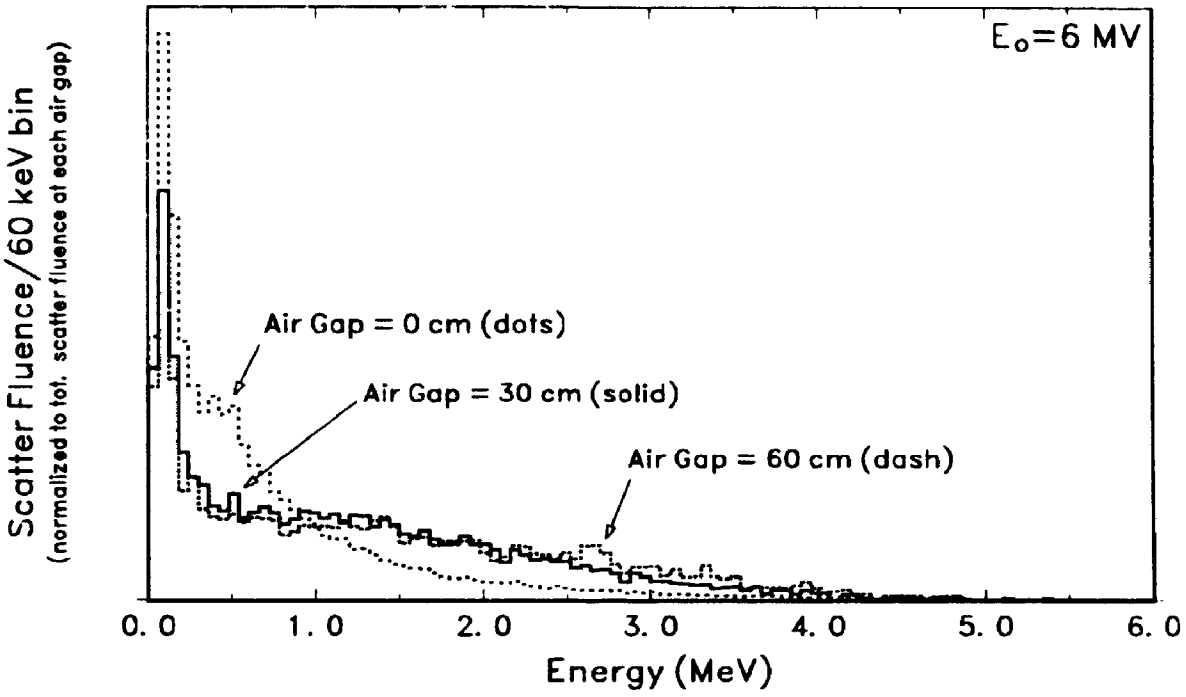

Figure 4.9 Scatter spectra at 0, 30, 60 cm air gaps for a 6 MV x-ray beam (30x30 cm^2 field size) incident on a 17 cm slab of PMMA

primary fluence was also corrected to accourt for the minor reduction in fluence with increasing radial position due to increased source to scoring bin distance (i.e. inverse-square law). The results shown here are slightly higher than those reported by Swindell et al.[6], this is attributed to the consideration of bremsstrahlung and positron annihilation processes in our simulations.

The scatter fractions in Fig. 4.8d, which lie outside the edge of the primary beam, have little importance in terms of image quality, however, they may be important in the design of future portal imaging systems. The results show that for large area flat panel detectors, which are currently being developed for portal imaging, the electronic circuitry which lies within 5 cm of the edge of these detectors will be exposed to a significant

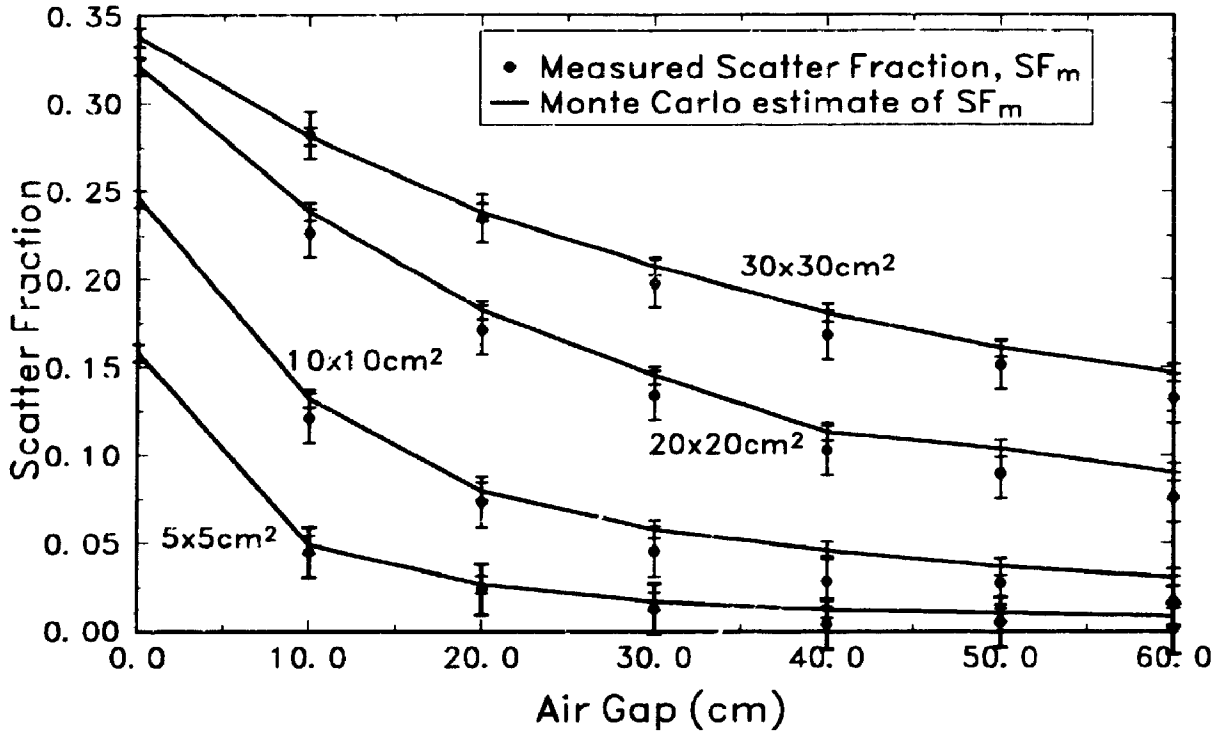

Figure 4.10 Comparison of scatter fractions (SF_m - Eq. 4.2) measured using the ionization chamber and diode with those calculated from the Monte Carlo generated fluences and detector response

scatter fluence. For a 30 x 30 cm^2 field, this scatter fluence is approximately one fifth of the total (scatter + primary) received at the centre of the detector itself. This suggests that the detector electronics must either have a high radiation resistance or will have to be shielded, increasing the weight of the detector assembly.

4.3.4 Experimental validation and comparison with the literature

Figure 4.10 shows a comparison of the scatter fractions measured experimentally with those calculated from the Monte Carlo simulations. Because the radiation detector (ionization chamber with PMMA buildup cap) used in the scatter fraction measurements (sec 4.2.2.1) recorded **signal** rather than counted photons, the Monte Carlo generated

fluences were converted using the procedure outlined in section 4.2.2.2 to allow the comparison. Absolute errors in the experimentally-measured scatter fractions are estimated to be +/- 0.015 based on detector signal reproducibility, detector positioning, and the error in our primary signal estimate. The errors in the Monte Carlo results are +/- 0.005, based on statistical uncertainty in the individual fluence estimates. Figure 4.10 shows that the experimentally-measured scatter fractions agree, within experimental and statistical uncertainties, with those calculated from the Monte Carlo generated fluences.

In addition to the comparison of our measured scatter fractions to that estimated by Monte Carlo simulations, we have also compared our Monte Carlo results with those found in the literature. As we have shown, scatter is highly dependent upon geometric

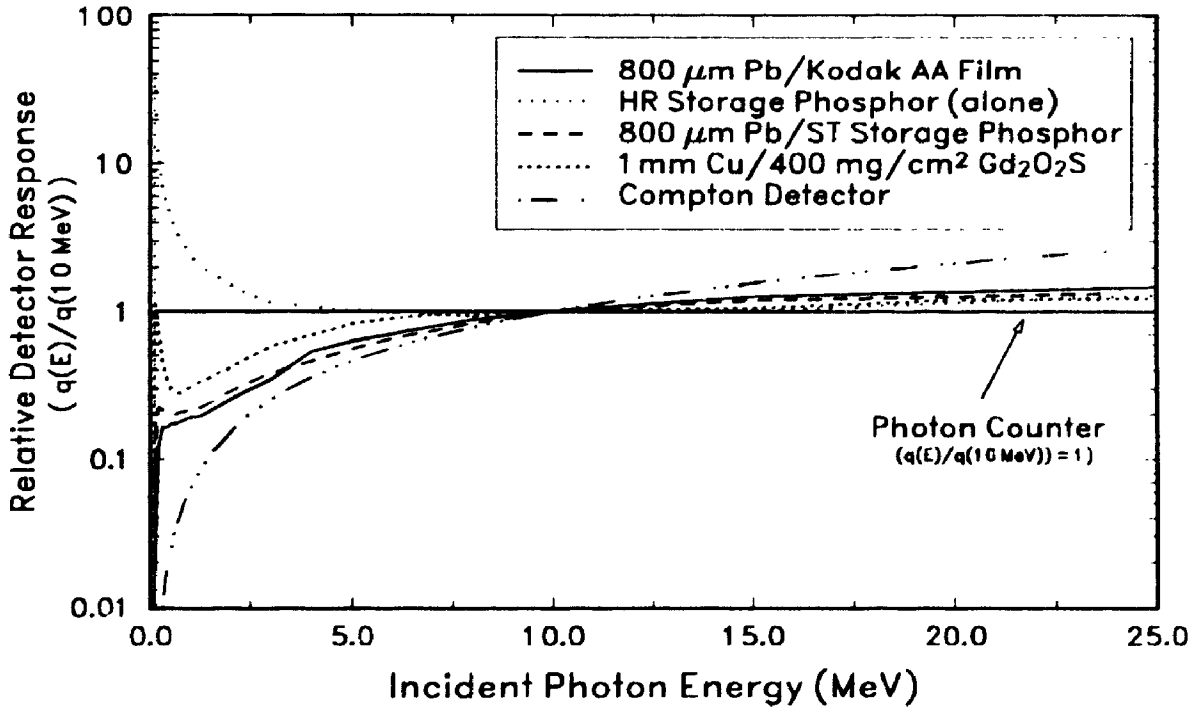

Figure 4.11 Detector response curves (MeV/incident photon) for 5 different imaging detectors Each curve has been normalized to its response at 10 MeV to allow inter-comparison

considerations, therefore, our results cannot be compared directly to those calculated assuming other geometries, such as that reported by Barnea and Dick.[5] Furthermore, Barnea and Dick report *planar* fluences in their paper instead of spherical fluence. To allow direct comparison of our results, we modified the scoring of our Monte Carlo code from spherical fluence to planar fluence and simulated the geometry described in their report. For a 1 MeV monoenergetic x-ray beam incident on 21 cm of polystyrene (0 cm air gap, 10 x 10 cm^2 field size, 2 m source-slab-distance) Barnea and Dick reported a scatter fraction of approximately 0.36 while we have calculated a scatter fraction of 0.38. In addition to a comparison of scatter fluences with those published by Barnea and Dick, we have compared our calculated SF_{signal} values with those measured for a metal plate/film detector by Droege et al.[4] In their study, they measure scatter fractions in an 8 MV treatment beam for a detector with various thicknesses of lead plate in contact with Kodak XM film. The geometry consisted of a 30 cm x 30 cm field incident on 20 cm of polystyrene, measurements were performed for an air gap of 30 cm. Based on their results, we estimated the scatter fraction (SF_{signal}) for an 800 μm thick lead plate to be 0.32. We have replicated their geometry with two exceptions: a 6 MV x-ray beam is used, instead of 8 MV, and the scattering slab consists of PMMA, as opposed to polystyrene. Considering these two differences, we obtain a SF_{signal} of 0.24 which is comparable to their estimate (0.32). The discrepancy in the scatter fraction represents a difference in the estimate of the primary signal by about 10%. This discrepancy is somewhat expected, as Droege et al. do not compensate for the dependence of accelerator output on field size in determining the primary component used in their scatter fraction calculations. Typically, the output of a medical linear accelerator changes by about 10% when the field size is

increased from 3 cm x 3 cm to 30 cm x 30 cm.[17] Assuming a 10% underestimate in their primary component, we re-calculate Droege et al.'s scatter fraction to be 0.25, very close to our estimate of 0.24. With the above qualifications, our Monte Carlo estimates of scatter agree well with those that have been calculated[5] or measured[17] previously.

4.3.5 Scatter Fractions for typical imaging detectors

Figure 4.11 shows the relative response of the five detectors described in section 4.2.3. While the relative response of the detectors is similar at energies in excess of 5 MeV, the response to lower energy x-rays varies by orders of magnitude. The HR storage phosphor is sensitive to low-energy x-rays. The relative response of the lead plate/ST storage phosphor detector shows that this sensitivity to low energy x-rays can be reduced significantly by inserting a lead plate. This occurs because the lead plate filters out the low-energy photons before they can deposit their energy in the storage phosphor. The copper/Gd_2O_2S detector has a response intermediate to these two detectors. This is the result of the intermediate atomic number of the copper plate (Z = 29). The copper is not as effective at attenuating the low-energy x-rays, therefore, a moderate fraction reach the Gd_2O_2S phosphor. The response of the Compton recoil-electron detector is different from that of the HR storage phosphor. The sensitivity of the Compton recoil-electron detector is greatest for the highest energy x-rays. As x-ray energy is increased, the Compton scattered photon transfers a larger and larger fraction of its energy to the recoil-electron. For a finite thickness detector, this increase in energy transfer ($R(E)$) would be balanced by a decrease in the quantum efficiency ($\eta(E)$). However, in our implementation, we have used the formalism developed by Swindell[6] where the quantum efficiency is fixed at

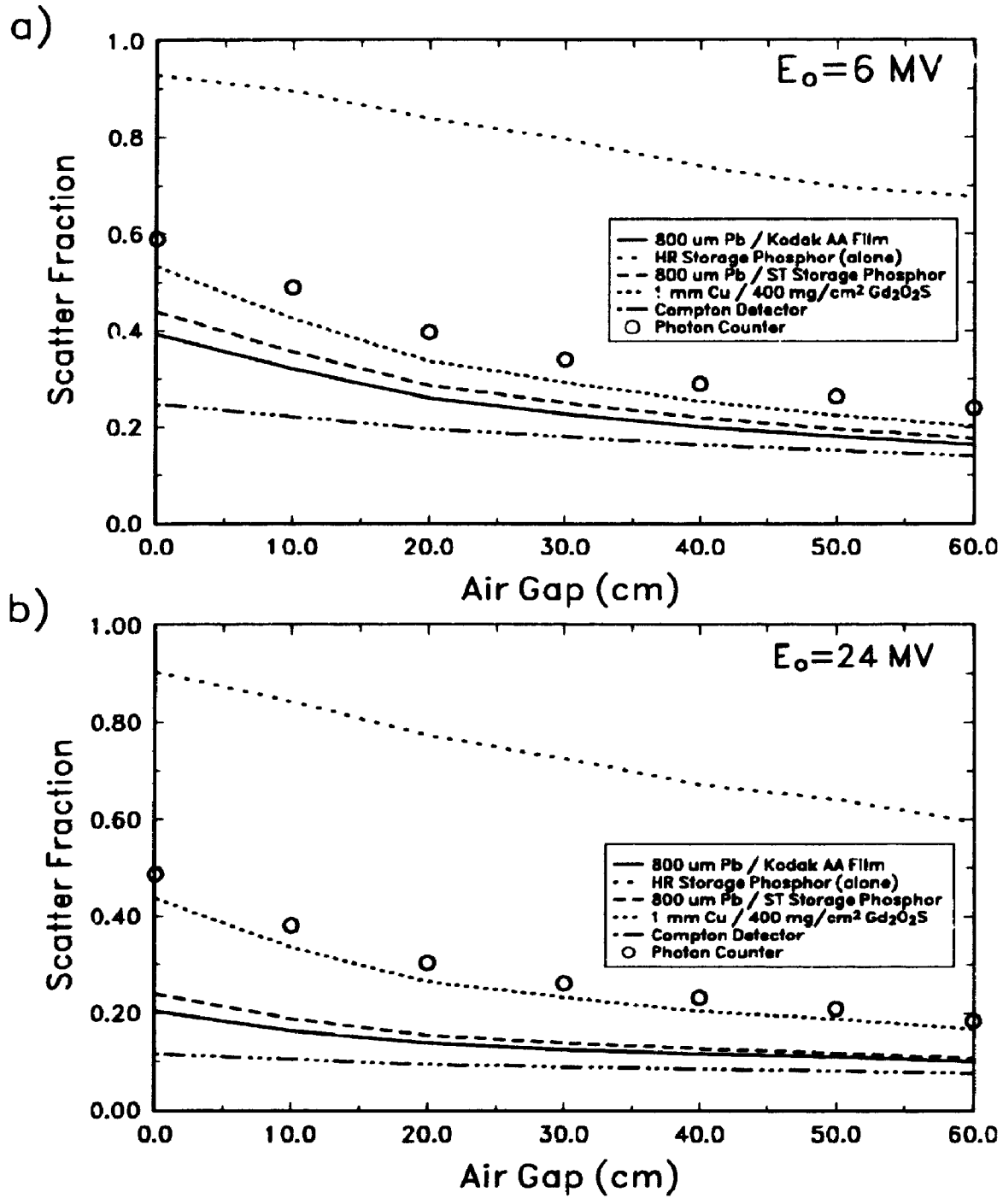

Figure 4.12 Signal scatter fraction (SF_{sg} - Eq. 4.5) vs. air gap for the 5 different imaging detectors shown in Fig 4.10

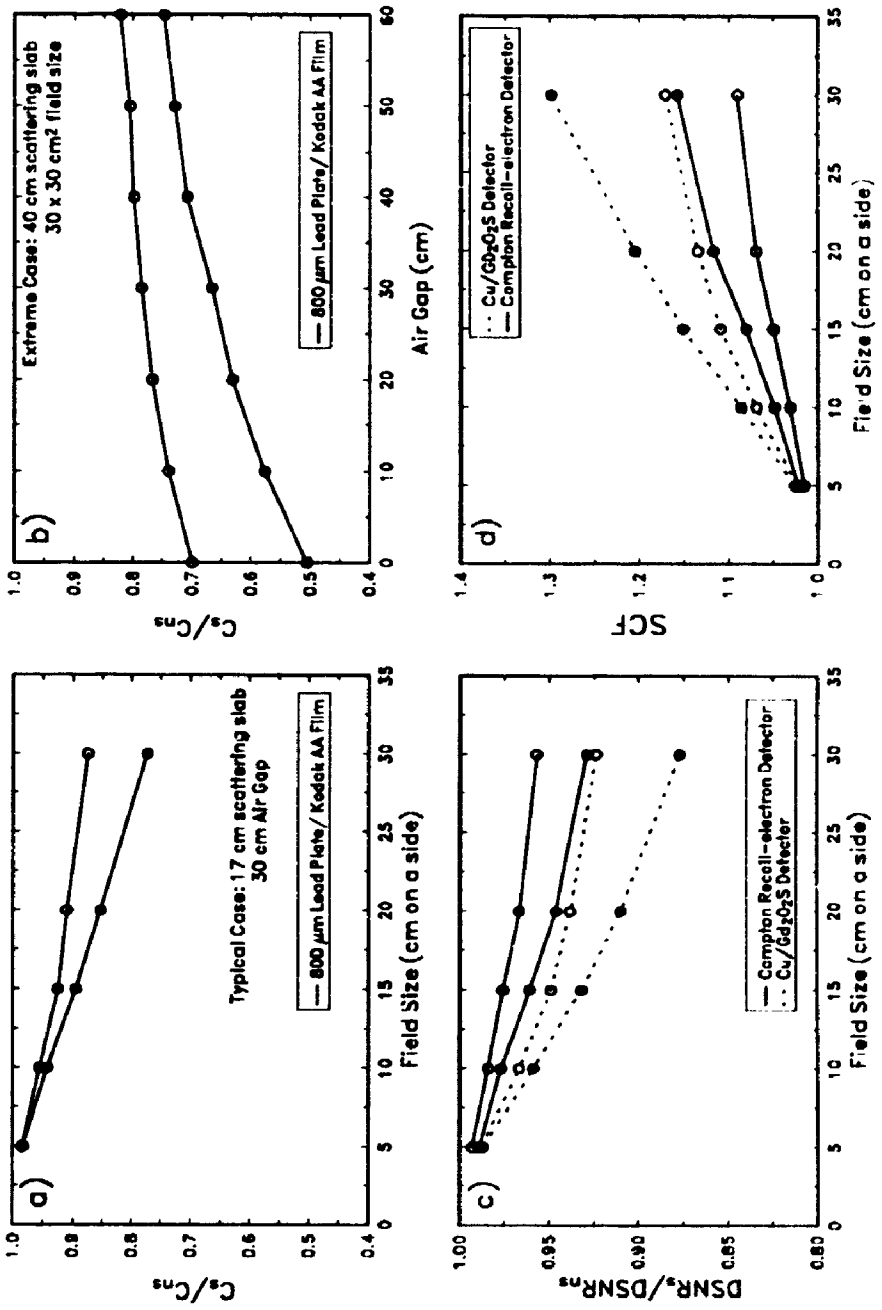

Figure 4.13 The effect of scatter on contrast and DSNR for various geometries (6MV - solid, 24MV - open). Panels a), b) & d) are for a 17cm thick PMMA scattering slab and a 30 cm air gap

unity. The resulting response is more representative of a very thick x-ray detector, such as the 25 mm thick zinc tungstate ($ZnWO_4$) detector developed by Morton et al.[27]

Scatter fractions have been calculated for each of the five x-ray detectors using Eqs. 4.3 and 4.5. The dependence of scatter fraction on air gap is shown in Fig. 4.12. The geometry for these calculations is the same as that in Fig. 4.8c, a 30x30 cm^2 field incident on 17 cm of PMMA. For a specific geometry, the scatter fractions vary over a wide range because the scatter and primary spectra are significantly different. The sensitivity of the bare HR storage phosphor to low-energy x-rays results in the scatter signal being 9 times larger than the primary signal. A detector with the opposite characteristics (high-energy sensitivity), such as the Compton recoil-electron detector, results in a scatter signal which is one third that of the primary. These two detectors give different scatter fractions for the same primary and scatter spectra arriving at the detector. Detectors more typical of those used in portal imaging, such as the copper plate/Gd_2O_2S or lead plate/film detector, have flatter response characteristics and thus result in intermediate scatter fractions.

4.3.6 Estimating the effect of scatter on image quality

The impact of x-ray scatter on image quality is dependent upon the noise characteristics and display properties of the imaging system. Imaging systems which are quantum noise limited will have added noise injected by the scatter fluence, and for systems with a fixed display contrast, the scatter signal will reduce the contrast of objects in the image.

A typical portal film imaging system (metal plate/film), which is not quantum noise limited[28] and, which has a fixed display contrast, will have a loss in contrast due to the added scatter signal. The reduction in contrast is equal to the scatter fraction (Sec. 4.2.4). Figure 4.13(a) shows that, for the 800 μm lead plate/Kodak AA film detector and a 6 MV beam, the scatter signal can reduce the contrast by as much as 25% depending on field size (17 cm PMMA, 6 MV, 20 cm air gap). Under more extreme conditions, such as a 40 cm thick scattering slab and a 10 cm air gap, the contrast can be reduced by 50% (Fig. 4.13(b)). Considering the low primary contrast of objects in megavoltage imaging, such a loss may place these objects below the visibility threshold.

For quantum noise limited portal imaging systems, the scatter fluence will introduce additional x-ray quantum noise into the images, thereby, reducing the DSNR. We have calculated the loss in DSNR for the Compton recoil-electron detector and the copper/Gd_2O_2S detector for a range of field sizes (Fig. 4.13(c)). In addition, the SCF [Eq. 4.10] has also been calculated for the same geometry (Fig. 4.13(d)). The SCF is the factor by which the dose to the patient must be increased in order to maintain a specified DSNR. The Compton recoil-electron detector predicts that the effect of scatter on the DSNR is limited, particularly for the 24 MV beam. The copper/Gd_2O_2S detector results predict that the influence of scatter is more important; it is necessary to increase the dose to the patient by 30 percent to compensate for the increased noise associated with the scatter fluence (Fig. 4.13(c)). The reason for this difference is because the Compton recoil-electron detector responds most efficiently to the higher energy (i.e., primary) photons, while the copper plate/phosphor screen detector responds much more than the Compton recoil-electron detector to lower energy (i.e., scattered) photons (see Fig. 4.11).

While there are no x-ray quantum noise limited portal imaging systems available, large area, amorphous silicon, flat panel, light sensors[29] may offer this level of performance eventually. These light sensors are more likely to be used with a phosphor screen detector. Therefore, for (future) x-ray quantum noise limited imaging systems, x-ray scatter will have a moderate effect on image quality.

For the TV camera-based portal imaging systems that are currently available, the effect of scatter on image quality will be quite variable depending upon the characteristics of the imaging system. The performance of the TV camera portal imaging systems can be limited because either: (i) the "quantum sink" is at the stage where photoelectrons are produced in the TV camera (i.e. inefficient optical light collection), or (ii) additional noise is added in the pre-amplifier of the TV camera. In case (i) the effect of scatter would be identical to an x-ray quantum limited imaging system (i.e. up to 20 % change in DSNR). However, in case (ii) the effect of scatter would be negligible because the additional x-ray quantum noise added by the scatter fluence would be small compared to that added by the TV camera. For a portal imaging system such as that characterized by Bissonnette et al.[30], the effect of x-ray scatter on image quality would be expected to be negligible. Therefore, for currently available TV camera-based portal imaging systems, the effect of scatter may range from negligible to moderate depending on the light collection efficiency of the optical chain, as well as the quantum efficiency and noise characteristics of the T.V. camera.

4.4 Summary and Conclusions

The magnitude of the scatter fractions at megavoltage energies (0.1 - 0.6) has

been found to be much lower than those found at diagnostic energies (0.3 - 0.93) for similar geometries.[3] This is a result of the considerable increase in primary transmission associated with the higher energy x-rays. While the scatter fluence is still largely the result of Compton scattering at the higher energies, the order of the scatter is reduced compared to that found in diagnostic beams. In addition, as the incident x-ray energy is increased above approximately 1 MeV, bremsstrahlung and positron annihilation processes become more prevalent. These produce x-rays which contribute to the low energy component of the scatter spectrum. For a 20 MeV monoenergetic beam, bremsstrahlung and positron annihilation photons originating from within the scattering slab produce 73 percent of the scatter fluence detected (0 cm air gap, 30 x 30 cm^2 field, 17 cm of PMMA). In contrast, for a 24 MV clinical spectrum under the same geometry, bremsstrahlung and annihilation photons account for only 25 percent of the scatter. Unlike the Compton scattered photons, the contamination photons are concentrated at the lower energies. Considering only energies below 750 keV, these photons account for 40 percent of the scatter fluence generated by a 24 MV incident x-ray spectrum. Thus, the bremsstrahlung and positron annihilation quanta reduce the average energy of the scatter fluence.

At megavoltage energies, the scatter spectrum is of significantly lower energy than that of the primary component. This is important when considering the energy response (energy deposited/incident photon) of different portal imaging detectors. For a specific geometry, the SF_{signal} (Eq. 4.5) values of five different detectors ranged from 0.2 to 0.9 depending on the response of the detector to the lower-energy x-rays in the scatter spectrum. Detectors which had a thick (~1 mm) lead plate on the entrance face were found

to minimize scatter signal, because of the preferential filtering of the low-energy scatter fluence. Failure to introduce such a filtering plate results in very high scatter fractions.

Scatter will moderately influence image quality, depending on the display and noise characteristics of the detector. The most dramatic effect of scatter will be to reduce contrast in imaging systems with fixed display contrast, such as portal films. The amount of contrast loss depends heavily on geometry. Under extreme conditions, the contrast of objects in the image will be reduced by 50%. The effect of x-ray scatter on the quality of images produced by currently available on-line systems will range from negligible to moderate (20% loss in DSNR) depending upon the light collection efficiency and noise characteristics of the TV camera. The development of large area, amorphous silicon, light sensors may make quantum noise-limited portal imaging systems feasible. For such systems, the noise introduced by the added scatter fluence will reduce the DSNR by 10-20% for typical imaging geometries.

References

1. H-P. Chan and K. Doi, "The validity of Monte Carlo simulation in studies of scattered radiation in diagnostic radiology," Phys. Med. Biol., **28**(2), 109-129 (1983).

2. M.J. Yaffe and P.C. Johns, "Scattered Radiation in Diagnostic Radiology: Magnitudes, Effects, and Methods of Reduction," J. Appl. Photo. Eng., **9**, 184-195 (1983).

3. C.E. Dick, C.G. Soares and J.W. Motz, "X-ray scatter data for diagnostic radiology," Phys. Med. Biol., **23**(6), 1076-1085, (1978).

4. R.T. Droege and B. E. Bjarngard, "Influence of metal screens on contrast in megavoltage x-ray imaging," Med. Phys., **6**(6), 487-493 (1979).

5. G. Barnea and C.E. Dick, "Coupled electron/photon Monte Carlo calculations of X-ray scattering with application to industrial radiography," NDT International, April, 111-115 (1987).

6. W. Swindell, E.J. Morton, P.M. Evans, and D.G. Lewis, "The design of megavoltage projection imaging systems: Some theoretical aspects," Med. Phys., **18**(5), 855-866 (1991).

7. D.W.O Rogers and A.F. Bielajew ,"Monte Carlo Techniques of Electron and Photon Transport for Radiation Dosimetry," Chapter 5 in Vol. III of *The Dosimetry of Ionizing Radiation*, edited by K.R. Kase, B.E. Bjarngard and F.H. Attix, (Academic Press, 1989), p. 481-521.

8. F.H. Attix, *Introduction to Radiological Physics and Radiation Dosimetry*, (John Wiley & Sons, New York, 1986), p. 5-17.

9. **The EGS4 Code System**, W.R. Nelson, H. Hirayama, and D.W.O. Rogers, Stanford Linear Accelerator Center Report, SLAC-265, (1985).

10. A.F. Bielajew and D.W.O. Rogers, "PRESTA - The Parameter Reduced Electron-Step Transport Algorithm for Electron Monte Carlo Transport," Nuc. Instr. and Meth., **B18**, 165-181 (1989).

11. **Improved bremsstrahlung photon angular sampling in the EGS4 code system**, A.F. Bielajew, R. Mohan, and C-S. Chui, National Research Council of Canada, Division of Physics Report, PIRS-0203, (1989).

12. **Use of ICRU-37/NBS Radiative Stopping Powers on the EGS4 System**, D.W.O. Rogers, S. Duane, A.F. Bielajew, and W.R. Nelson, National Research Council of Canada, Division of Physics Report, PIRS-0177, (1989).

13. **Use of ICRU-37/NBS Collision Stopping Powers on the EGS4 System**, S. Duane, A.F. Bielajew, and D.W.O. Rogers, National Research Council of Canada, Division of Physics Report, PIRS-0173, (1989).

14. Reference 9, p. 492-496.

15. S. Kubsad, R. Mackie, B. Gehring, D. Misisco, B. Paliwal, M. Mehta, and T. Kinsella, "Monte Carlo and Convolution Dosimetry for Stereotactic Radiosurgery," Int. J. Radiat. Oncol. Biol. Phys., **19**, 1027-1035 (1990).

16. R. Mohan, C. Chui and L. Lidofsky, "Energy and angular distributions of photons from medical linear accelerators," Med. Phys., **12**(5), 592-597 (1985).

17. G. Luxton and M.A. Astrahan, "Output factor constituents of a high-energy photon beam," Med. Phys., **15**(1), 88-91 (1988).

18. H.E. Johns and J.R. Cunningham, *The Physics of Radiology* (Charles C. Thomas, Springfield, 1983), p.372.

19. Reference 8, p. 20-30.

20. Reference 18, p. 226

21. Reference 8, p. 353.

22. Reference 8, p. 561.

23. G. Barnea and A. Ginzburg, "High energy x-ray film response and the intensifying action of metal screens," IEEE Trans. Nucl. Sc., **NS-34**(6), 1580-1585 (1987).

24. G. Barnea. E. Navon, A. Ginzburg, J. Politch, H. Roehrig, C.E. Dick, and R.C. Placious, "Use of storage phosphor imaging plates in portal imaging and high-energy radiography: The intensifying effect of metallic screens on the sensitivity," Med. Phys., **18**(3), 432-438 (1991).

25. H. Kanamori and M. Matsumoto, "Information spectra for radiographs modified by scatter," Phys. Med. Biol., **32**(6), 667-673 (1987).

26. Reference 8, p. 127.

27. E.J. Morton, W. Swindell, D.G. Lewis, and P.M. Evans, "A linear array, scintillation crystal-photodiode detector for megavoltage imaging," Med. Phys. **18**(4), 681-691 (1991).

28. P. Munro, J.A. Rawlinson, and A. Fenster, "Therapy imaging: a signal-to-noise analysis of metal plate/film detectors," Med. Phys. **14**(6), 975-984 (1987).

29. L.E. Antonuk, J. Boudry, W. Huang, D. L. MacShan, E. J. Morton, and J. Yorkston, "Demonstration of megavoltage and diagnostic x-ray imaging with hydrogenated amorphous silicon arrays," Med. Phys. **19**(6), 1455-1466 (1992).

30. J.P. Bissonnette, D.A. Jaffray, A. Fenster and P. Munro, "Physical characterization and optimal magnification of a portal imaging system," SPIE **1651**, 182-188 (1992).

Chapter 5. MONTE CARLO STUDIES OF X-RAY ENERGY ABSORPTION AND QUANTUM NOISE IN MEGAVOLTAGE TRANSMISSION RADIOGRAPHY[a]

[a] This chapter is to be submitted to *Medical Physics* under the title of "Monte Carlo studies of x-ray energy absorption and quantum noise in megavoltage transmission radiography" by D.A. Jaffray, J.J. Battista, A. Fenster, and P. Munro.

5.1 Introduction

In an ideal imaging system, each primary x ray transmitted through the patient is counted equally by the detector. However, most imaging systems do not count photons, but rather record a signal which is related to the energy deposited within the detector. X rays interacting within a radiographic imaging detector, such as a phosphor screen, typically deposit only a fraction of their energy. Because of the stochastic nature of energy deposition by x-rays, this fraction is not identical for each interacting x-ray (i.e. not deterministic). This random nature effectively introduces a "noisy gain (or conversion) stage" into the imaging system. For the low x-ray energies used in diagnostic radiology (10 to 100 keV), photoelectric absorption is the dominant x-ray interaction process. In a photoelectric interaction all of the x-ray energy is *transferred* to the detector, however, the amount of energy *absorbed* varies depending on the escape of characteristic x-rays (K-fluorescence) from the phosphor.

The amount of noise introduced by variability in energy absorption has been both calculated and measured for diagnostic energy x rays (10-100 keV) and typical diagnostic imaging detectors.[1,-6] Swank[1] has reported theoretical calculations which predict this variability for thin phosphors. Chan and Doi used Monte Carlo techniques to simulate radiation transport and absorption within several commercial phosphors.[3] Their Monte Carlo technique allowed Chan and Doi to score energy absorption events for each incident x ray; they report good agreement with the results of Swank.[2] Both of these studies examined x-ray absorption noise and quantum noise, ignoring the influence of any optical processes. Dick and Motz,[4] and more recently Ginzburg and Dick,[6] report measurements of the light pulse distributions emitted from typical diagnostic imaging phosphor screens.

These results include not only quantum noise and x-ray absorption noise, but also noise due to variations in light production and transport within the phosphor. In all of these studies, only diagnostic energy x rays were considered. The results of these studies show that the combined noise introduced by variations in x-ray absorption and light emission can reduce the detective quantum efficiency (DQE) of diagnostic imaging systems by 20 to 50 percent, depending on x-ray energy and phosphor thickness, with a large amount of this reduction being due to x-ray absorption noise.

In megavoltage transmission radiography, where incident x-ray energies are on the order of 1-10 MeV, the dominant interaction process is no longer photoelectric, but rather Compton scattering or pair production. In a Compton interaction, the fraction of energy transferred to the recoil-electron within the detector is much more variable than in a photoelectric interaction. Furthermore, the range of the scattered photon (10s of cm in water) and recoil-electron (several cm in water) can be much larger than the detector dimensions, allowing a fraction of the transferred energy to escape. In pair production, the range of both the electron and positron can become significant compared with the detector thickness. Therefore, at megavoltage energies the variance in the fraction of energy absorbed is expected to become large compared with the variations seen at diagnostic energies. Despite the reduction in DQE expected with this increase in variance at megavoltage energies, no information can be found in the literature regarding this phenomenon.

In this article, we present Monte Carlo calculations (Electron Gamma Shower, Version 4) which examine the magnitude of the x-ray absorption noise for megavoltage (100 keV - 20 MeV) x-rays and typical portal imaging detectors (metal plate/phosphor

screen). To confirm that our Monte Carlo technique is valid, we have compared the Monte Carlo results to measured pulse-height spectra for non-imaging applications. Our Monte Carlo calculations yield the absorbed energy distribution (AED) (pulse-height spectra of energy deposition) within the sensitive volume of a variety of imaging detectors. From the absorbed energy distributions, we calculate the influence of x-ray energy absorption noise on the detective quantum efficiency (DQE) of these imaging detectors. These results describe an upper limit on the DQE of typical megavoltage transmission radiography imaging systems.

5.2 Theory

The information content of an x-ray image can be described by the signal-to-noise ratio per resolution element[7]. The ability of an imaging system to transfer this image information is described by its DQE. The DQE is defined as,[4]

$$DQE = \frac{SNR^2_{out}}{SNR^2_{in}}. \qquad (5.1)$$

where SNR_{in} and SNR_{out} refer to the input and output signal-to-noise ratios, respectively. Swank has shown that the DQE of an x-ray imaging system can also be written as,[1]

$$DQE = \epsilon I = \epsilon I_{xi} \qquad (5.2)$$

where ε is the quantum absorption efficiency of the detector and describes the quantum

noise associated with the interacting photon fluence. I is referred to as the statistical factor and it describes the degradation in DQE due to a noisy gain stage in the system (see Appendix D). In this study, we restrict our investigation to the loss in DQE due solely to the variations in energy absorption per interacting x ray, and thus, define the statistical factor for this noisy gain stage as I_x.

The statistical factor, I_x, describes the variations in energy absorption per interacting x ray. This factor is calculated from the absorbed energy distribution (AED), A(E,E_i), for a given detector. The AED describes the probability that an incident x-ray of energy E_i will deposit an amount of energy E in the sensitive volume of the detector (eg. phosphor). The AED is best estimated by Monte Carlo techniques, since it cannot be measured directly. Measurements would require a method of direct detection of the energy pulse deposited in a detector for a single interacting x ray. Approximate AEDs can be determined from the light pulses produced within a scintillator exposed to x ra. However, such pulse-height spectra would include the variations in light production and transport within the scintillator and electronics noise, in addition to the variations in energy absorption which we want to determine.

Swank has shown that the statistical factor for a specific detector and incident x-ray energy can be calculated from the moments of the absorbed energy distribution,

$$I_x(E_i) = \frac{M_1^2(E_i)}{M_0(E_i)\,M_2(E_i)}, \qquad (5.3)$$

where, the moments of the distribution are calculated in the usual manner as:

$$M_j(E_i) = \int_0^{E_i} E^j A(E, E_i)\, dE. \qquad (5.4)$$

Therefore, we write the DQE as,[1,3]

$$DQE(E_i) = \epsilon(E_i)\, I_x(E_i) = \frac{M_1^2(E_i)}{M_2(E_i)}, \qquad (5.5)$$

where, the quantum absorption efficiency, $\varepsilon(E_i)$, is also determined from the absorbed energy distribution. Provided the distribution has been normalized to the number of incident photons used to generate the AED, the quantum absorption efficiency is $M_0(E_i)$, which is equal to the area under the AED. This quantity (Eq. - 5.5) would be the DQE for a detector which was capable of detecting the absorbed energy directly, without the additional noise introduced by the conversion to, and transport of, light quanta. The DQE for quantum noise and x-ray energy absorption noise is also referred to in the literature as the noise-equivalent absorption (NEA).[1,3]

We have limited the scope of this chapter to a study of the influence of quantum noise and x-ray absorption noise on the DQE of typical megavoltage imaging detectors. We do not examine the influence of light production and transport within the phosphor, nor do we address the spatial distribution of the energy deposited within the detector. The DQE of a complete system will definitely be further influenced by optical processes. However, once the DQE has been deteriorated by the quantum absorption efficiency and x-ray absorption noise, it cannot be recovered. Therefore, the results presented in this study represent an upper limit on the DQE of any system which employs the types of x-

ray detectors examined here. Considering the influence of the spatial distribution of the energy deposited by the interacting x-ray has been addressed by other authors[8] for diagnostic energies but is beyond the scope of this paper. Ignoring the spatial distribution of the energy deposited within the detector restricts our study to a 'zero-frequency' analysis of the x-ray absorption noise.

5.3 Materials and Methods

5.3.1 Monte Carlo calculations of absorbed energy distributions, $A(E,E_i)$

5.3.1.1 Monte Carlo code

The Electron Gamma Shower (EGS4) code system,[9] which has been tested extensively over the energy range under consideration here,[10,11] is used to determine the absorbed energy distribution (energy pulse-height spectra) for megavoltage x-rays incident on typical portal imaging detectors. Our user code (RZ_PHS) simulates coupled photon-electron(positron) transport within a plane-cylindrical geometry and scores the amount of energy deposited within the detector volume for each photon history.

The EGS4 code is used in its standard configuration[9] with the following modifications. We include the Parameter Reduced Electron Step Transport Algorithm (PRESTA)[12] with the correction recommended by Malamut et al.[13] PRESTA makes the transport of charged particles less dependent on user-selected parameters and decreases calculation times while retaining an accurate model of the physics involved. The RZ_PHS code also uses the improved sampling of the bremsstrahlung photon angular distribution,

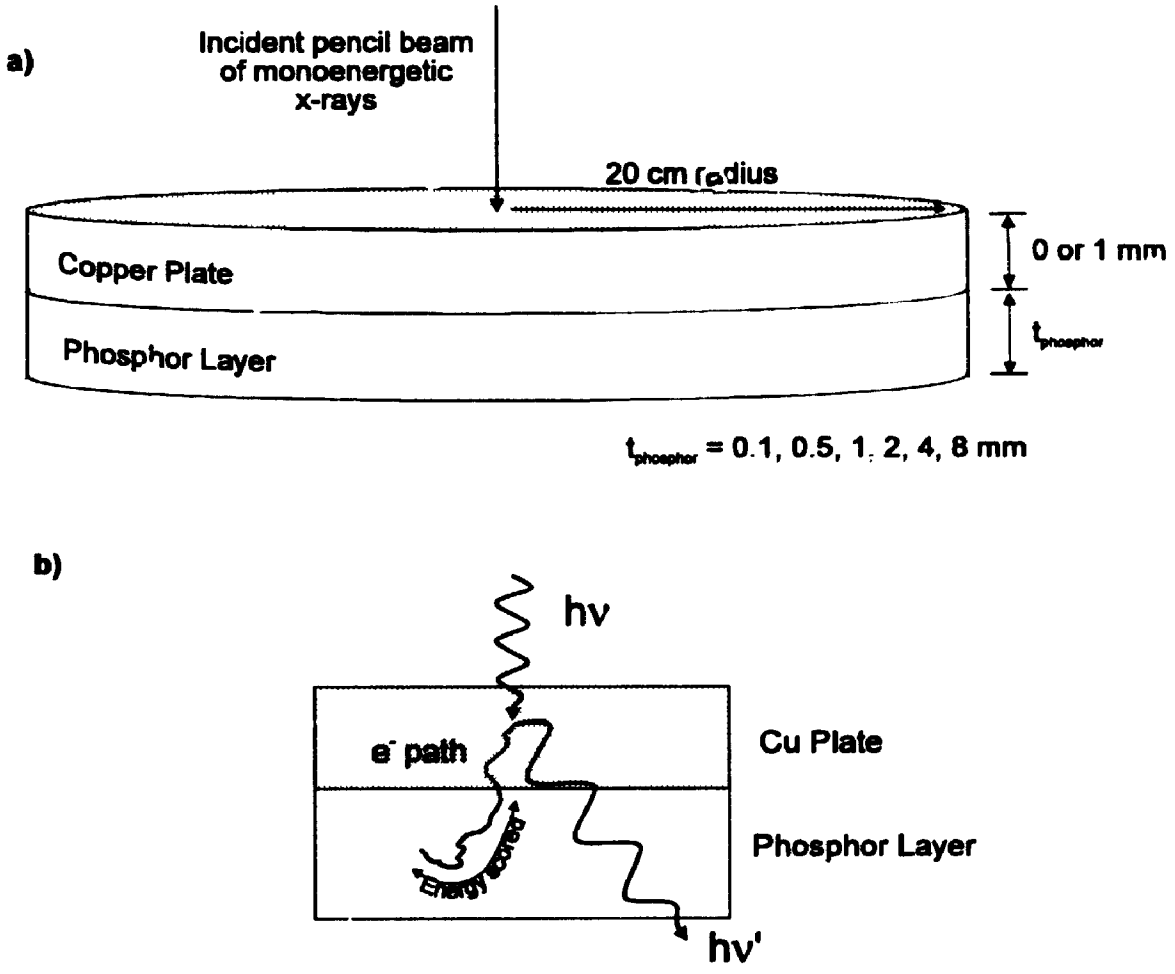

Figure 5.1 (a) Diagram of the Monte Carlo geometry used in determining the absorbed energy distributions (AEDs). (b) Illustration of energy scoring in phosphor layer only

as developed by Bielajew et al.[14], as well as the improved radiative and collision stopping powers.[15,16] In addition, the density effect corrections were included in the collisional stopping powers of all materials for which the correction data were available.[16] The process of K-fluorescence production was *not* treated in these simulations; K-fluorescence is not significant at the high x-ray energies investigated here.

The EGS4 Monte Carlo code has a number of parameters which control the transport of charged particles. PCUT and ECUT represent the minimum total energy (kinetic plus rest-mass) of photons and electrons which are transported. AP and AE represent the energy thresholds for creation of secondary photons and electrons (δ rays), respectively. For the simulations reported in this article, we set PCUT=AP=10 keV and ECUT=AE=521 keV. These values were chosen to allow accurate modelling of charged particle transport within the detector volumes. The user-adjustable parameters for the PRESTA algorithm were left at their default values.

5.3.1.2. Detector geometry

The modelled geometry, shown schematically in Fig. 5.1, consists of a pencil beam of photons (infinitesimal width) perpendicularly incident on a planar imaging detector (40 cm diameter). Two types of detectors were modelled in our study: (i) a detector which consisted of a phosphor screen alone; and (ii) a detector which consisted of a 1 mm copper plate in contact with a phosphor screen. Different phosphor screens were considered, ranging in thickness between 0.1 and 8.0 mm. For all screens, the phosphor layer was modelled as pure gadolinium oxysulfide (Gd_2O_2S) with a density of 3.67 g.cm^2. This is roughly half the actual density of Gd_2O_2S. The density was reduced in order to

account for the polymer binder and small air pockets within the phosphor layer.

5.3.1.3 Scoring the absorbed energy distributions (AED)

The absorbed energy distribution is very similar to a pulse-height spectrum and is calculated from the Monte Carlo simulations by scoring the amount of energy deposited (pulse-height) by each incident x ray (history) and, over a large number of histories, scoring the frequency with which each pulse-height occurs. The AEDs reported in this study were scored with an energy resolution of 10 keV per bin. The AED was determined for each detector, and for 10 monoenergetic incident x-ray energies, ranging from 100 keV to 20 MeV. In all simulations, the number of histories was sufficient to reduce the statistical uncertainty in the reported AEDs to less than 10% in each bin. Typically, this required in excess of 1 million incident photon histories. The statistical uncertainties were estimated by dividing all simulations into 10 batches and computing the variance in the mean.[11] The simulations required 6 to 72 hours of CPU time on a workstation (Sparcstation 2, Sun Microsystems, Sunnyvale, CA), depending on the energy of the incident photon beam and the thickness of the detector.

5.3.2 Confirmation of Monte Carlo results

The EGS4 code has been used extensively for scoring radiation dose deposited by ionizing particles in a variety of geometries.[10] Rogers has also shown that EGS is accurate in estimating the absorbed energy distribution in large detectors. He reports good agreement between EGS Monte Carlo estimates of the AED and experimental results for 6.13 MeV γ-rays incident upon a (5"x4") NaI crystal.[17] One limitation of this

comparison is that the large size of the detector minimizes the effects of charged particle transport because most charged particles would be fully stopped in such a large detector.

For the high x-ray energies (>100 keV) and relatively thin detectors used in megavoltage imaging, charge particle transport begins to play an important role in energy deposition. Therefore, accurate modelling of the electron transport within these detectors is necessary to obtain reliable estimates of the absorbed energy distributions. Berger et al. have measured the pulse-height spectrum of 500 keV electrons impinging on a thin (191 μm) layer of silicon.[18] The ionization pulse produced by an electron as it traversed the silicon layer was scored with a multi-channel analyzer. The resulting spectra were then calibrated at the full absorption peak in the distribution (500 keV). To allow direct comparison between these results and their own Monte Carlo generated AEDs, their Monte Carlo results were first broadened by the intrinsic resolution of the detector (~15.4 keV FWHM gaussian). Berger et al. reported good agreement between their measurements and their "broadened" Monte Carlo estimates.

To ensure that the electron transport algorithm employed by EGS4 properly models electron transport in the small detector volumes under consideration, we compared the AED generated by the RZ_PHS code with pulse-height distributions measured by Berger et al. Using the RZ_PHS code, we determined the AED produced by 500 keV electrons incident on a 191 μm layer of silicon. The resulting distributions were broadened using the techniques described by Berger et al. to account for the intrinsic resolution of their silicon detector. The results of our Monte Carlo calculations are compared with those obtained experimentally by Berger et al.

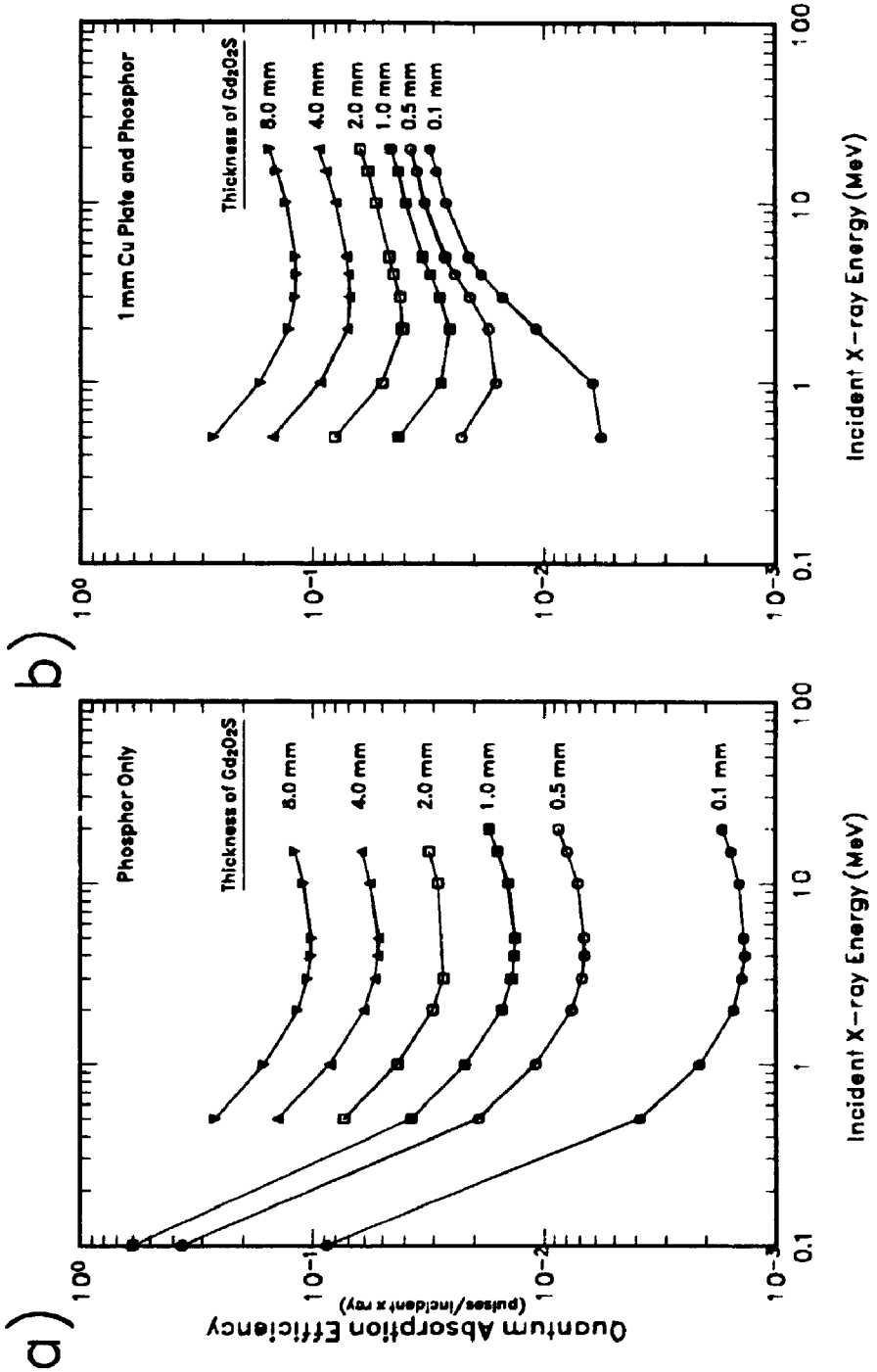

Figure 5.2 Quantum absorption efficiency (QAE) versus x-ray energy for (a) phosphor and (b) copper/phosphor detector. The QAE is the number of pulses produced in the phosphor per incident x-ray.

5.4 Results

A number of quantities, such as the quantum absorption efficiency, detector response, and the statistical factor, can be calculated from our Monte Carlo estimates of the AEDs. These quantities are summarized in the following sections.

5.4.1 Quantum absorption efficiency, $\varepsilon(E_i)$

The quantum absorption efficiency is shown in Fig. 5.2 for a phosphor screen (a) without and (b) with a copper plate. The quantum absorption efficiency is the fraction of *incident x-rays* which deposit energy in *the phosphor layer*. (Only x rays which deposit energy in the phosphor layer are considered because only these x rays can generate the light signals which are detected by a light sensor.) For the phosphor screen alone, the quantum absorption efficiency is high at low energies; declines rapidly to a minimum and then rises slowly due to the increasing cross-section for pair-production in the high atomic number phosphor (Fig. 5.2(a)). As shown in Fig. 5.2b, the copper plate alters the quantum absorption efficiency. At low x-ray energies the copper plate attenuates the low-energy x rays, preventing them from even reaching the phosphor (i.e., it acts as an x-ray filter). At higher energies the copper plate generates a high-energy electron fluence which enters the phosphor (i.e. acts as a "build-up" layer).

For an x-ray detector which consists of a phosphor screen alone, every interacting x ray will deposit energy in the phosphor layer. Therefore, there is a one-to-one correspondence between the number of x-rays *interacting* in the detector and the number of energy pulses produced in the phosphor. However, the introduction of a copper plate changes this one-to-one correspondence since an x ray which interacts in the copper plate

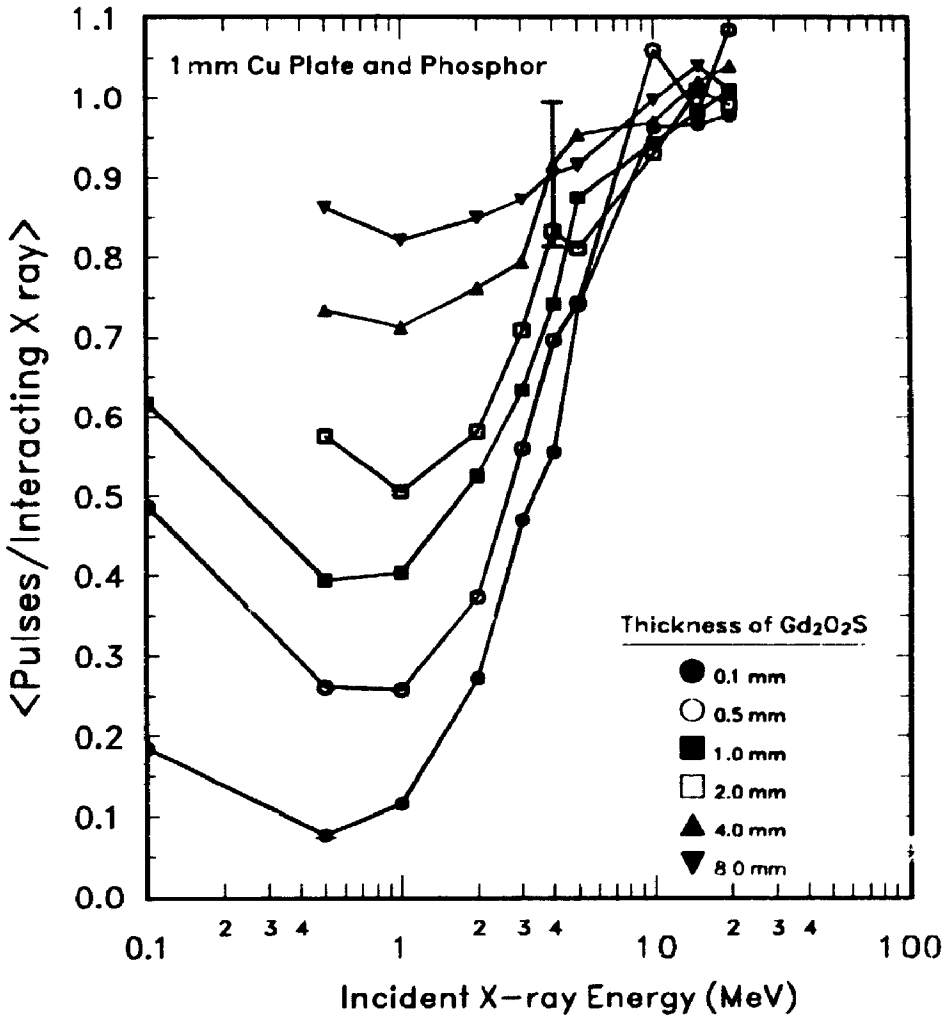

Figure 5.3 Probability that an interacting x ray will deposit energy in the phosphor of a Cu plate/phosphor screen detector Values greater than 1 0 are due to statistical uncertainties in the data

does not necessarily result in energy being deposited in the phosphor layer. Figure 5.3 shows the mean number of pulses produced in the phosphor layer per *interacting* x ray when the copper plate is in place. At low x-ray energies, where the photoelectric interaction process is dominant, the mean number of pulses per interacting x ray is significantly less than one (i.e., many x rays interact in the copper plate but do not generate a signal in the phosphor screen). This corresponds to the ratio of the photoelectric cross-section for the phosphor layer to that of the entire detector (phosphor layer and copper plate). As x-ray energy is increased, the Compton cross-section starts to dominate, resulting in a larger fraction of the x-rays interacting in the copper plate. This reduces the probability that an interacting x ray will deposit energy in the phosphor screen. As the x-ray energy exceeds 1 MeV, the range of the Compton recoil electrons (and eventually electron-positron pairs) generated in the copper plate becomes large enough to escape the copper plate and deposit energy in the phosphor, thereby, increasing the probability that an interacting x ray will deposit energy in the phosphor screen. Eventually, the number of pulses per interacting x ray approaches unity - every x ray that interacts in the copper plate/phosphor detector deposits *some* of its energy in the phosphor layer. (The ratio plotted in Fig. 5.3 should not exceed 1.0, however, the datapoints shown in Fig. 5.3 were calculated from two separate Monte Carlo runs and statistical uncertainties in the two simulations resulted in ratios greater than 1.0.) Figure 5.3 shows that for a typical portal imaging x-ray detector (1 mm copper plate/1 mm phosphor screen) and for a typical therapy x-ray beam (2 MeV monoenergetic ≈ 6 MV) only half of the x-ray photons interacting in the detector deposit energy in the phosphor screen. Thus, half of the x rays which interact in the detector do not generate a measurable signal.

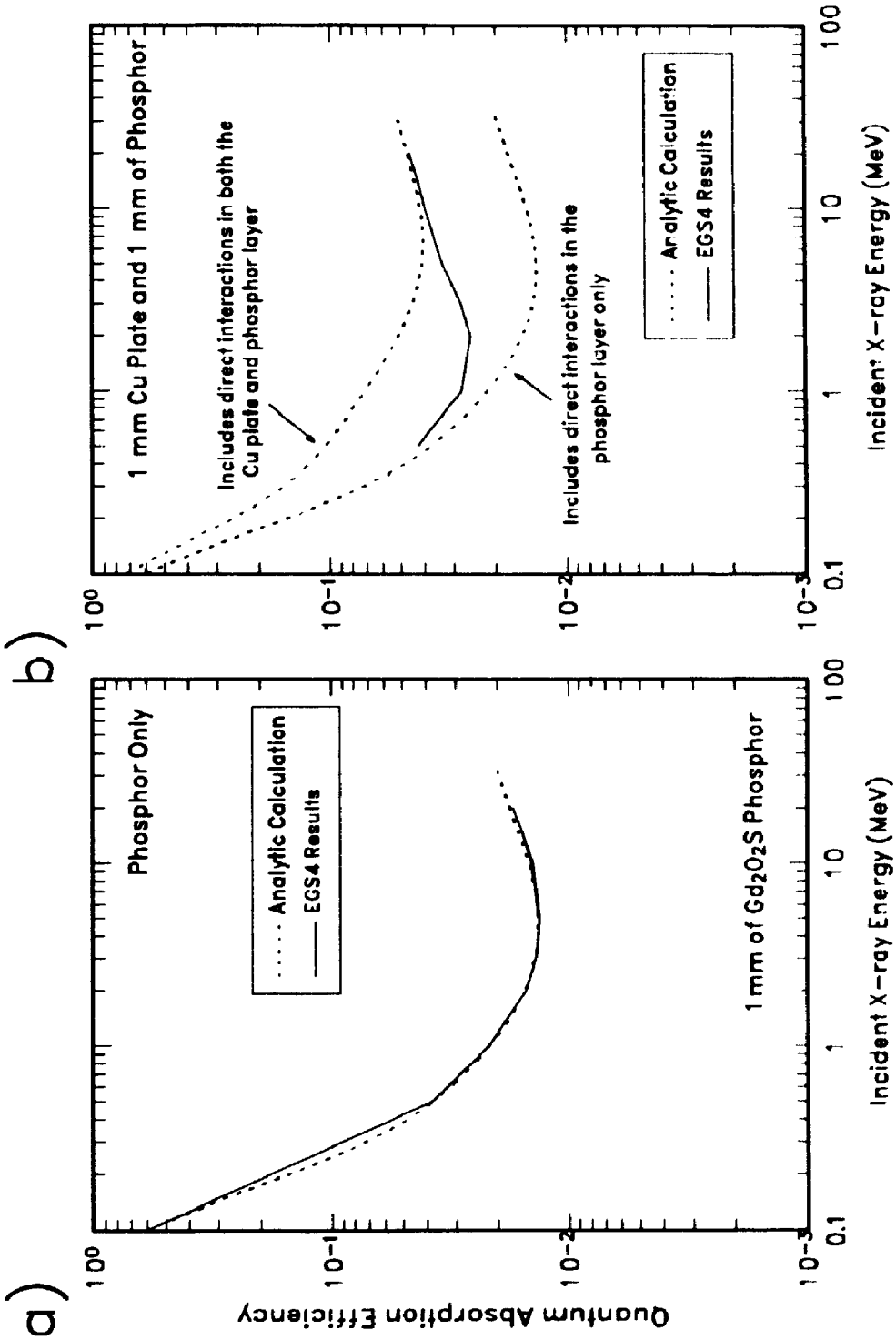

Figure 5.4 Comparison of Monte Carlo estimates of the QAE with those calculated from simple attenuation calculations for both (a) the phosphor and (b) the Cu plate/phosphor detector

To further illustrate the importance of including secondary particle transport in the calculations, we have estimated the quantum absorption efficiency for both a phosphor screen alone and a metal plate/phosphor screen assuming no electron transport (i.e., only x-rays which interact directly in the phosphor screen contribute to the quantum absorption efficiency) or assuming "efficient" electron transport (i.e., all interacting x rays contribute to the quantum absorption efficiency). The results of these estimates are compared to the Monte Carlo generated results in Fig. 5.4. For the phosphor screen alone (Fig. 5.4a), the Monte Carlo results are in excellent agreement with the primary attenuation calculations. However, for the copper plate/phosphor screen (Fig. 5.4b), the analytic calculations do not agree with the Monte Carlo generated results over the entire x-ray energy range. At low x-ray energies (< 500 keV), the Monte Carlo results agree with the no electron transport calculations while at high x-ray energies (> 10 MeV) the Monte Carlo results agree with the "efficient" electron transport calculations. However, at the energies of most interest in therapy imaging (approximately 2 MeV), only the Monte Carlo calculations give an accurate estimate of the quantum absorption efficiency. Clearly, care must be taken in estimating the quantum absorption efficiency for detector geometries and x-ray energies where the range of the charged particles generated in the detector is comparable to the dimensions of the detector.

5.4.2 Detector Response: energy deposited per incident x ray

While the quantum absorption efficiency counts the number of photons that interact with the x-ray detectors, what is of greater importance in imaging is the energy deposited by these x rays. The detector response, which is the average energy deposited in the

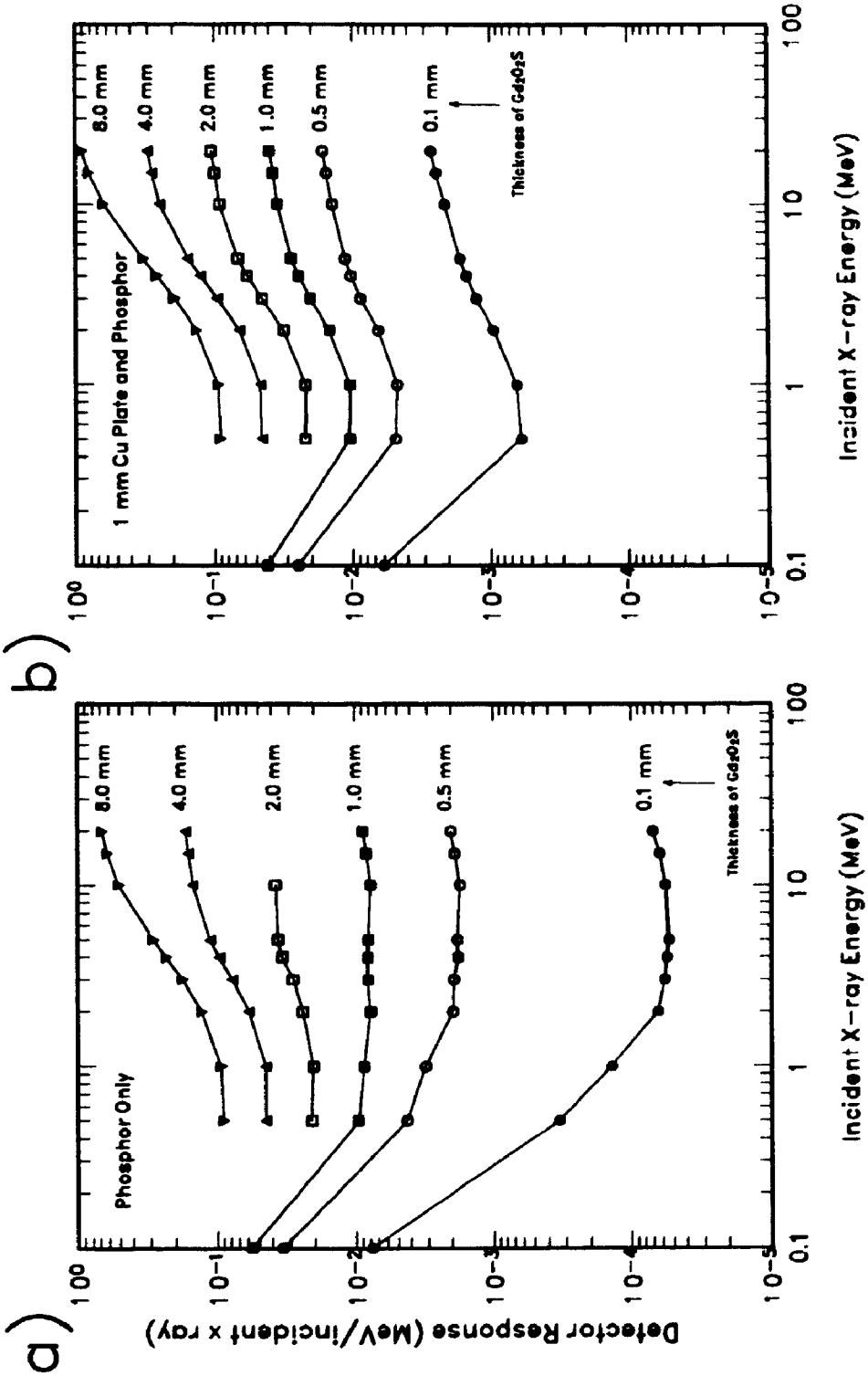

Figure 5.5 Detector response versus x-ray energy for (a) the phosphor alone and (b) the copper plate/phosphor combinations.

phosphor screen per incident x ray (MeV/incident x-ray), is shown in Fig. 5.5. Comparing the quantum absorption efficiencies and detector responses of these detectors, it is clear that the increased energy deposited by the higher energy x rays compensates somewhat for the decreasing number of interactions.

The presence of the copper plate enhances the detector response of the phosphor screens, particularily for the thinner phosphors and higher x-ray energies. For example, the copper plate enhances the response of the 0.1 mm thick phosphor layer by 10 to 16 times at x-ray energies above 2 MeV, while for a 1 mm thick phosphor screen the enhancement is only 2 to 4 times. Clearly, the copper plate will increase the light signal produced by these screens by large factors. This explains why typical portal imaging detectors are commonly composed of metal plate/phosphor screen combinations.

5.4.3 Absorbed energy distributions (AEDs)

Before the AEDs for fluoroscopic imaging detectors were calculated, the accuracy of the electron transport mechanisms used in EGS4 were tested by simulating the experiments performed by Berger et al.,[18] who measured the distribution of charge pulses liberated (proportional to energy deposited) within a thin (191 μm) silicon layer by a 500 keV electron beam. Figure 5.6 compares our Monte Carlo calculations with the results measured by Berger et al.. The low-energy peak seen in the EGS4 results corresponds to the "straight through" passage of electrons depositing approximately 70 keV of energy ($t_{silicon} \times S/\rho \times \rho = 0.0191$ cm $\times$ 1.63 MeV·cm^2/g $\times$ 2.32 g/cm^2 = 72 keV). It is near this low-energy peak where the only discrepancy occurs. Berger et al. noted a similar discrepancy

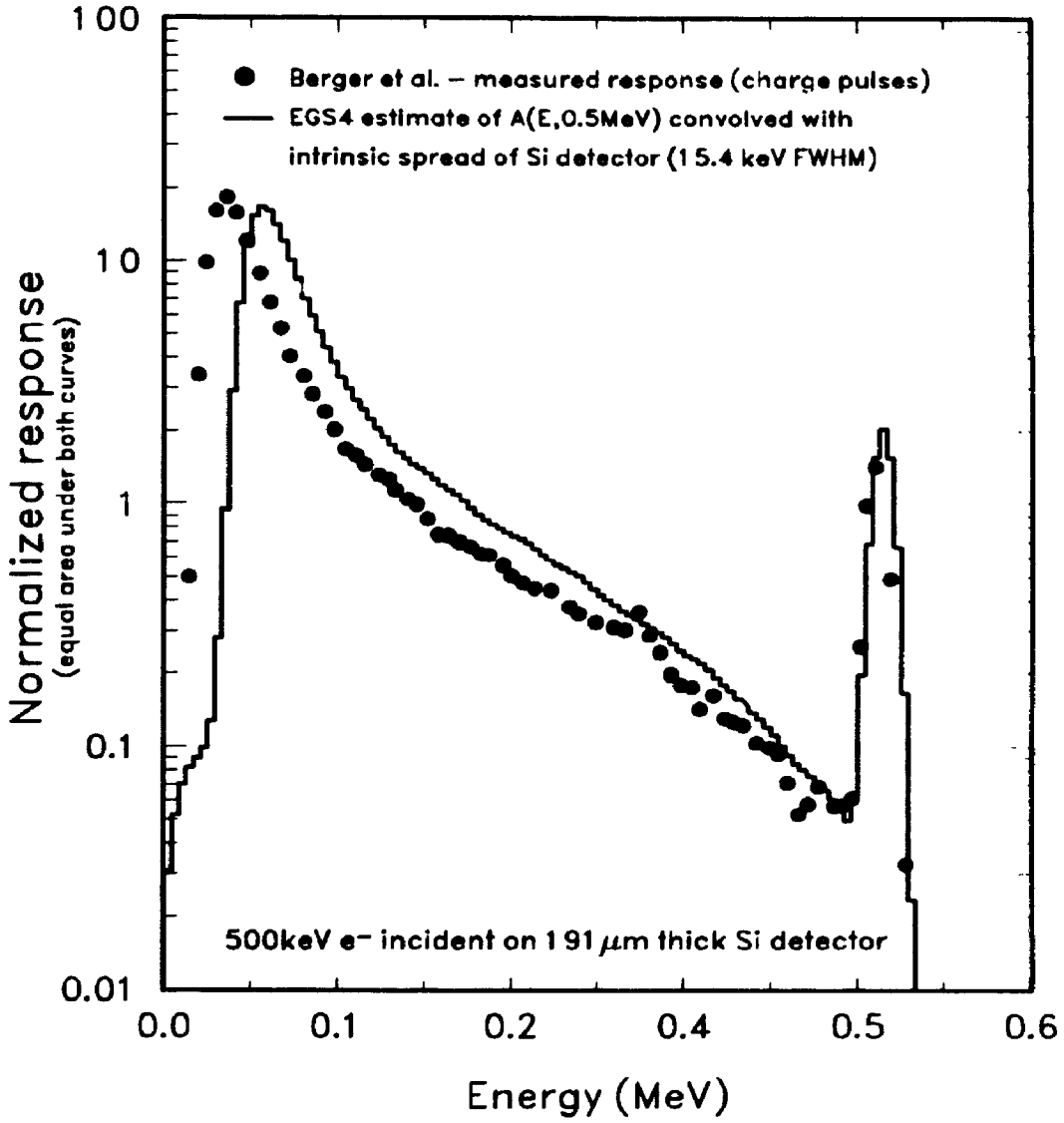

Figure 5.6 The accuracy of our Monte Carlo code was assessed by comparing the absorbed energy distribution (AED) calculated by the RZ_PHS code with a measured pulse-height spectrum

between the measurements and their Monte Carlo calculations and hypothesized that it was due to 'channeling effects' in the silicon. We suspect, however, that the difference between the measured and the Monte Carlo generated distributions is the result of a simplification in the electron transport algorithm of both EGS4 and Berger's Monte Carlo code. Both of these codes assume a mean stopping power for each electron transport step, where each electron step includes many (10's) of inelastic collisions. If one examines the single-collision energy loss distribution, it is clear that the mean is a poor representation of the actual distribution.[19] The single collision energy loss distribution is skewed toward lower energy-loss events. For a high energy electron (i.e., $\beta \approx 1$, $E_{kinetic} > 100$ keV), the mean energy loss per collision in silicon is roughly 1 keV while the most probable energy loss per collision is only 0.016 keV. Since EGS4 is essentially forcing the energy loss in every collision to be higher (1 keV) than the most probable (0.016 keV), the AED is skewed toward higher energy loss events. Correcting this would require extension of the EGS4 Monte Carlo code to include single-collision energy loss. Nevertheless, our comparisons show that, with the exception of the discrepency at low energies, the Monte Carlo generate AEDs agree well with experimental measurements.

The AEDs for the phosphor screens alone (i.e., no copper plate) are shown are shown in Fig. 5.7. From these AEDs, the statistical factors can be derived using Eq. 5.3. Each AED shown in Fig. 5.7 has been scaled (horizontally and vertically) to fill the frame, thereby allowing comparison of the shape of each AED. Plotting the AEDs in this fashion hides the quantum efficiency and detector response information contained within each AED. However, since the statistical factor depends only on the relative shape of the AED, these plots give us insight into how the statistical factor is influenced by incident x-ray

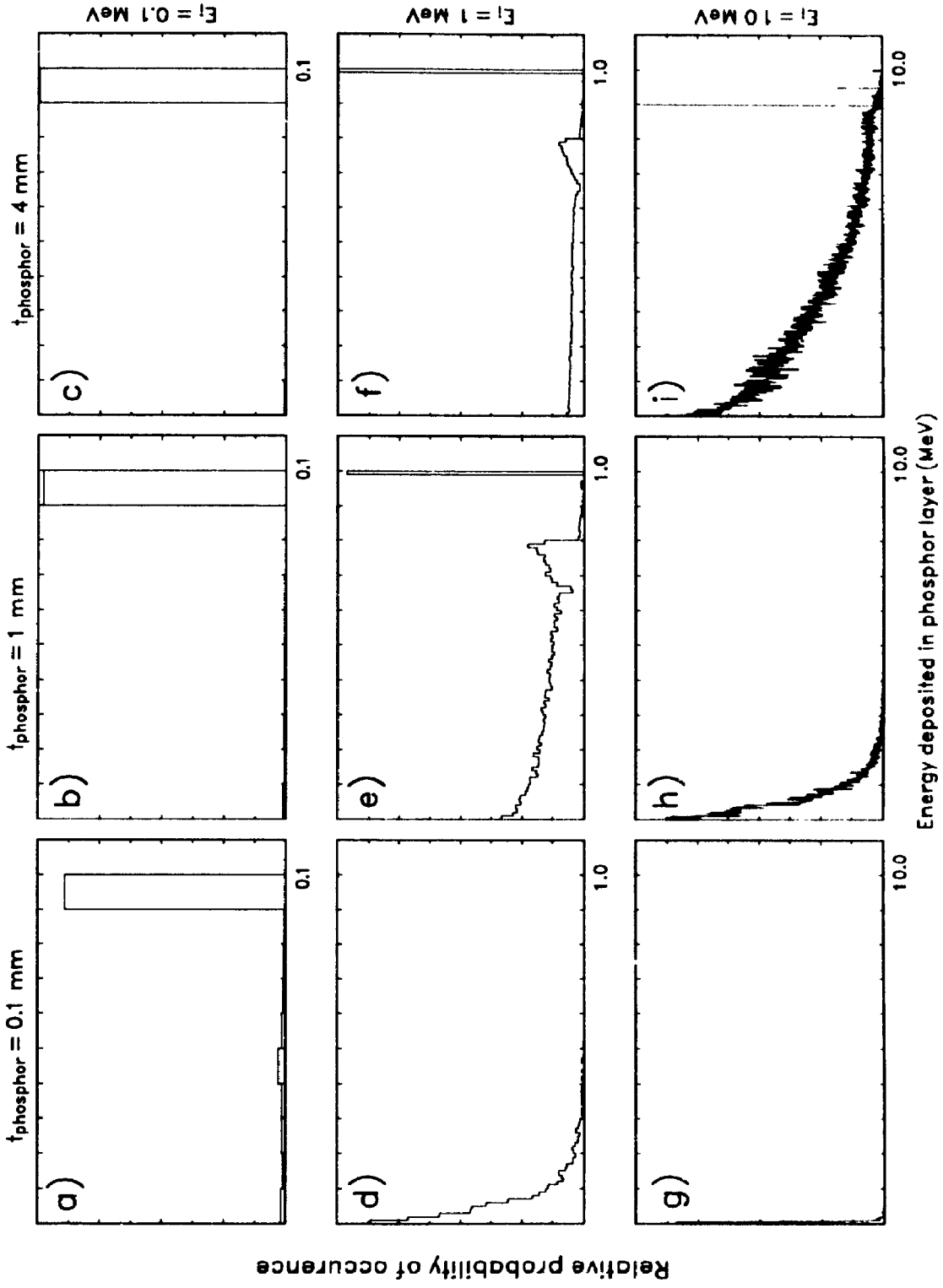

Figure 5.7 Absorbed energy distributions (AEDs) for phosphor screen alone (no Cu plate) The shape of the AED is strongly influenced by the phosphor thickness and x-ray energy

energy and the thickness of the phosphor.

At the low x-ray energies (E_i = 0.1 MeV), the AED is dominated by the photopeak because of photoelectric absorption in the high atomic number phosphor (Z_{eff} for Gd_2O_2S is approximately 47). Increasing the thickness of the phosphor layer has little influence on the AED at these low energies. As x-ray energy is increased further (E_i = 1 MeV), Compton scattering becomes the dominant interaction process, and the Compton continuum becomes a major feature in the AED. Because the Compton recoil electrons are responsible for depositing the energy, the AED becomes very sensitive to the phosphor thickness. For the thin phosphor layer ($t_{phosphor}$ = 0.1 mm), most of the recoil-electrons deposit only a fraction of their energy before they escape the phosphor, resulting in the AED shown in Fig. 5.7d. The Compton edge becomes easier to distinguish when the phosphor thickness is increased to 1 mm (Fig. 5.7e). This is the result of Compton recoil-electrons depositing all of their energy in the phosphor layer, while the Compton scattered x-ray escapes. The small peak in the Compton continuum at 0.8 MeV is the result of Compton scattering kinematics; as the energy of the incident x-ray increases, not only does the fraction of energy transferred to the Compton recoil electron increase, but so does the likelihood of achieving maximum energy transfer.[20] Thus, the electron spectrum produced in the phosphor is weighted towards high energy electrons. Increasing the thickness of the phosphor layer (1 mm and 4 mm) increases the probability of fully absorbing these high energy electrons (Fig. 5.7e&f). If the energy of the incident x-ray beam is increased to 10 MeV, pair production becomes the dominant interaction process. The change from Compton scattering to pair production does not influence the AEDs for the thin (0.1-1.0 mm) phosphors. As can be seen, the AED in Fig. 5.7h is very similar to

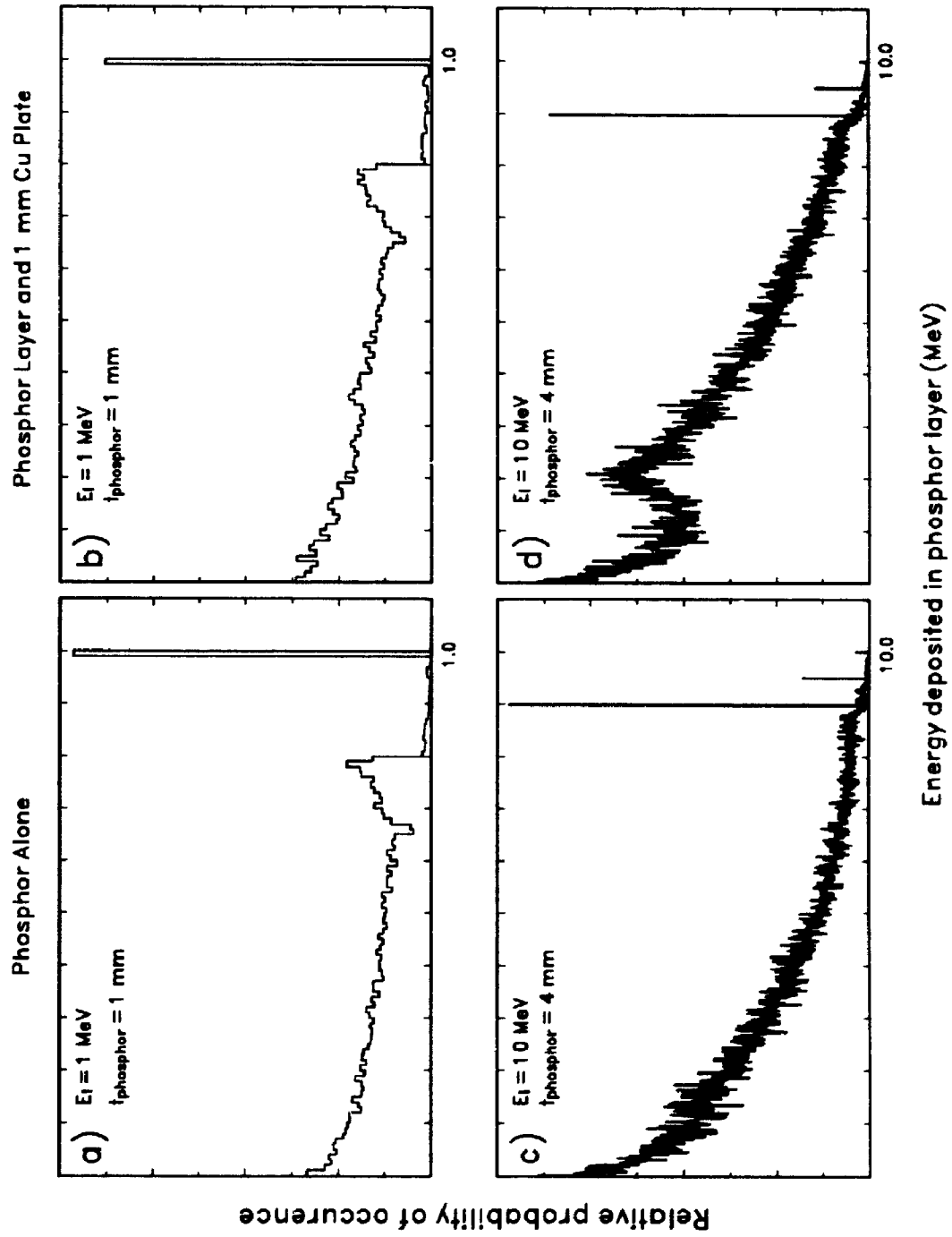

Figure 5.8 The presence of the Cu plate alters the AEDs of the phosphor layer, particularly at higher x-ray energies, where charged particles exit the plate and deposit their energy in the phosphor

that shown in Fig. 5.7d where only a small fraction of the electron's (or positron's) energy is deposited in the phosphor layer. However, for the 4 mm thick phosphor layer, pair production results in several peaks in the AED. At this thickness, it is possible to have the charged particles (positrons and electrons) deposit all of their kinetic energy. However, when the positron annihilates, two 0.511 MeV annihilation quanta are emitted and carry away 1.022 MeV of energy. If both escape the phosphor, a maximum of 10 MeV minus 1.022 MeV of energy is deposited, and if one escapes, a maximum of 10 MeV minus 0.511 MeV is deposited. The three peaks corresponding to no-escape, single-escape and double-escape of annihilation photons can be seen in Fig. 5.7i.

Figure 5.8 shows the influence of the copper plate on the AEDs of the x-ray detectors. Comparing the AEDs in Figs. 5.8a and 5.8b shows that the copper plate does not significantly alter the shape of the AED for 1 MeV incident x-rays. However, at higher energies (E_i = 10 MeV) the presence of the copper plate results in a peak in the AED at approximately 2 MeV (Fig. 5.8c,d). This peak is the result of high energy electrons (up to 9 MeV of kinetic energy) exiting the copper and traversing the phosphor layer. The energy of the peak corresponds to the thickness of the phosphor times the electron stopping power of the phosphor at these energies ($t_{phosphor} \times S/\rho \times \rho$ = 0.4 cm × 1.3 MeV·cm^2/g × 3.67 g/cm^3 = 1.9 MeV).

5.4.4 Statistical factor, I_x

The statistical factor, which describes the loss in DQE due to the variablity in energy absorption per interacting x ray, has been calculated using Eq. 5.3. The results of these calculations are shown in Fig. 5.9. As stated before, the shape of the AED

determines the statistical factor, I_x. Before examining the results in Fig. 5.9, it is instructive to consider how changes in the shape of the AED influence the statistical factor. From Eq. 5.3 we can see that the statistical factor decreases if the variance becomes large and it approaches unity if the variance becomes small. The variance is *minimized* if the all peaks in the AED are close to the mean of the distribution. One way to achieve this is to have only a single peak in the AED. This distribution is similar to that shown in Fig. 5.7c. Alternatively, the variance will be *maximized* if all the peaks in the AED are far from the mean of the distribution. One way to acheive this would be to have two peaks in the AED with the (energy weighted) mean of the distribution half way between the two peaks. In order for the (energy weighted) mean to be half way between the two peaks, each peak must contain equal energy. This implies a distribution which consists of a large peak at low energies and a small peak at high energies. This is similar to the distribution shown in Fig. 5.7e. Thus our simple analysis suggests that AEDs similar to those shown in Fig. 5.7c and 5.7d will generate large and small statistical factors, respectively.

Figure 5.9 shows clearly that the statistical factor is influenced strongly by phosphor thickness, the energy of the incident x-ray beam, and the presence of the copper plate (Fig. 5.9b). Overall, there are three energy-dependent trends in Fig. 5.9. Between 0.1 and 1 MeV, the statistical factor decreases with increasing energy, regardless of whether the copper plate is present or not. This is due to the escape of energy from the detector through Compton scattered photons and recoil-electrons (Fig. 5.7d,e,f). As a result the AED becomes broadly distributed, resulting in an increased variance in the distribution. Secondly, depending on the thickness of the phosphor, the

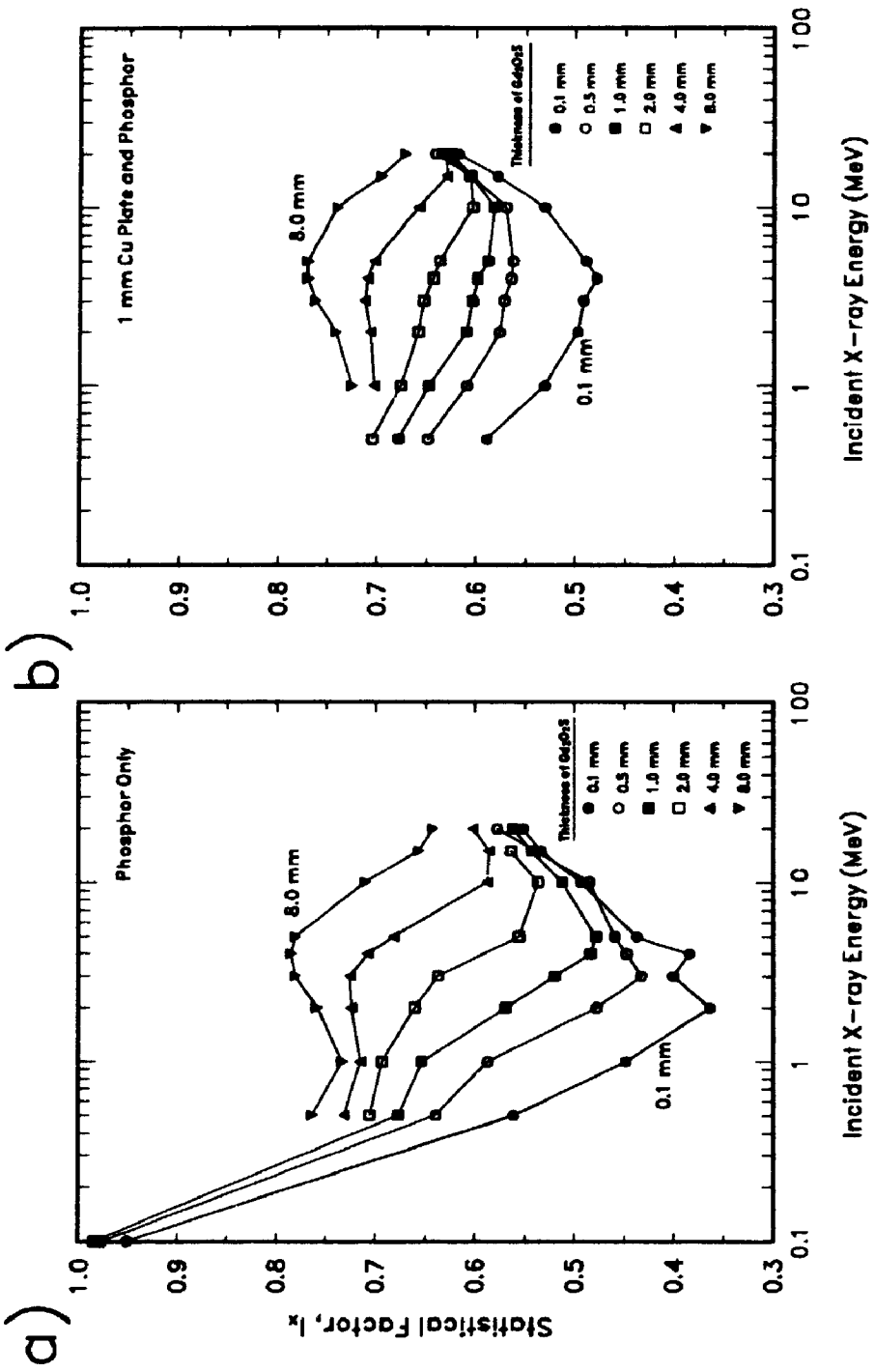

Figure 5.9 Statistical factor versus x-ray energy Compton scattering and enlarged electron ranges at megavoltage energies increase the variability in energy deposition per interacting x-ray.

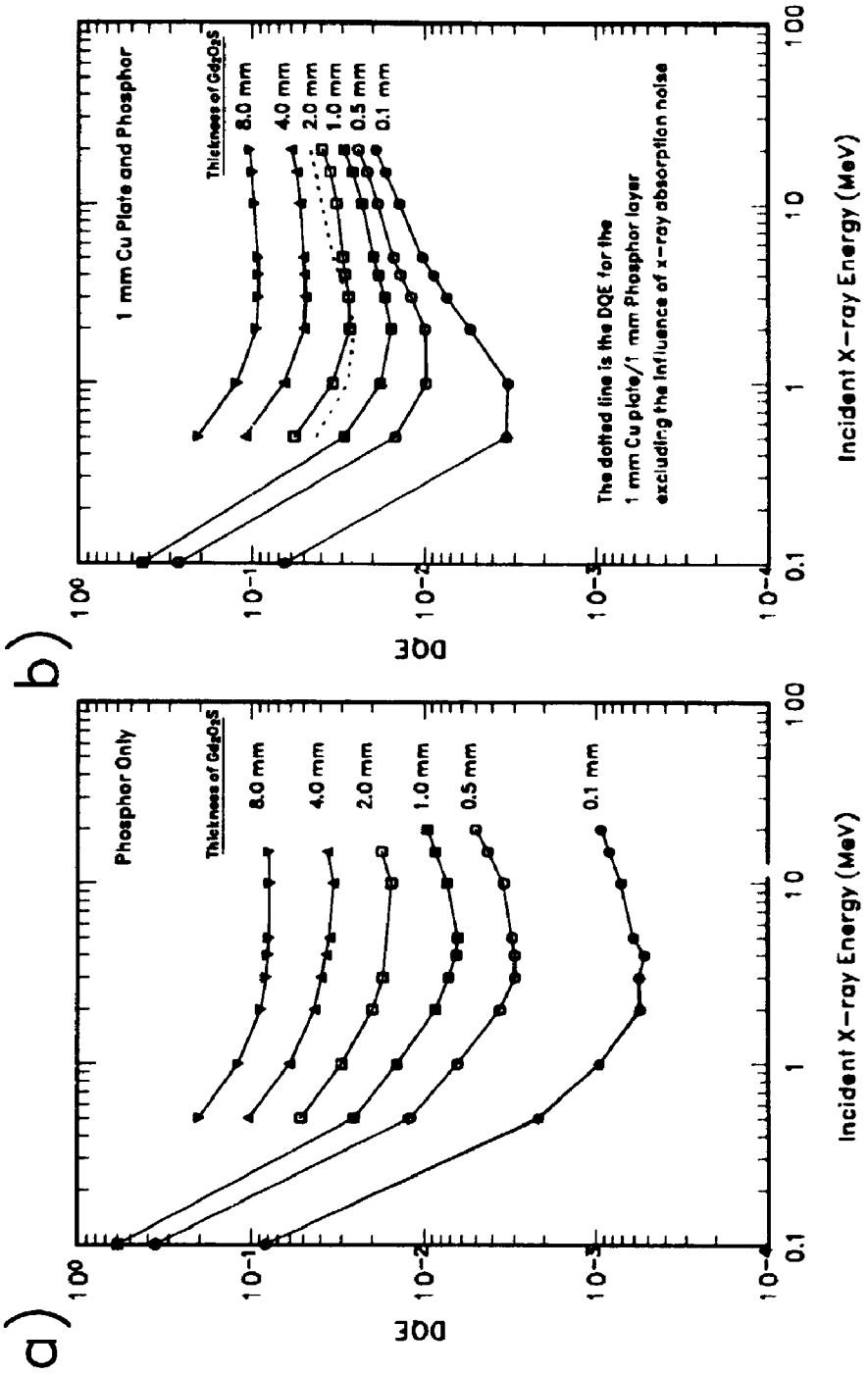

Figure 5.10 Detective quantum efficiency (DQE) versus x-ray energy The DQE includes the influence of both the QAE and the statistical factor The Cu plate increases both the QAE and I,

statistical factor may start to increase at x-ray energies above 1 MeV. This is the result of an increased fraction of the x-ray's energy being transferred to charged particles at higher x-ray energies and the increased probability of full-absorption in the thicker phosphor layers. Only the 4 and 8 mm thick phosphor screens demonstrate an increase in the statistical factor at energies below 2 MeV. At energies greater than 2 MeV, the range of the charged particles exceeds the phosphor thickness, and as a result, the statistical factor decreases. Finally, for the phosphor thicknesses considered here, the statistical factor converges to approximately 0.65 at the higher x-ray energies. This is the result of three effects. First, at high x-ray energies, the x-ray detector does not attenuate the x-ray beam significantly, hence charged particle generation is uniform throughout the entire volume of the detector. Second, because these charge particles are strongly forward directed, they can be assumed to follow a straight-line path from the point of generation to the exit surface of the phosphor screen. Third, since the collisional stopping power is nearly constant at these energies, the amount of energy deposited will be proportional to the distance travelled through the phosphor. The result is a rectangularly shaped AED. It can be shown that the I_x value for a rectangular AED is 0.75, however, the statistical factors shown in Fig. 5.9 converge to only 0.65 because other processes, such as, in-flight positron annihilation, bremsstrahlung production, and multiple scattering, are occuring within the detector and increase the variance in the AED.

Surprisingly, the presence of the copper plate can either increase or decrease the statistical factor. The presence of the copper plate decreases the statistical factor slightly at low x-ray energies (1 MeV) by generating electrons which deposit only a small fraction of their energy in the phosphor screen and increase the variance in the AED. However,

at higher x-ray energies (10 MeV) the copper plate can increase the statistical factors, particularily for detectors with thin (~1 mm) phosphor screens. At high x-ray energies, Compton scattering tends to produce an electron fluence in the copper plate which is weighted towards high energy electrons.[20] Many of these electrons have sufficient energy when they exit the copper plate to traverse the phosphor screen completely. These electrons produce a peak in the AED close to the mean of the distribution (see Fig. 5.8d; 1.9 MeV peak) which reduces the variance in the AED and hence increases the statistical factor.

Clearly, the influence of many factors on the statistical factor cannot be predicted *a priori* and must be determined by accurate simulations.

5.4.5 Detective quantum efficiency (DQE)

Figure 5.10 shows the DQE of both the phosphor screen and copper plate/phosphor screen detectors as a function of x-ray energy. These estimates of DQE, which were calculated using Eq. 5.4, include only quantum noise and x-ray absorption noise (i.e., do not include any optical effects). Our results show that the DQEs of the detectors decreases significantly at megavoltage energies compared to those found at diagnostic x-ray energies.

The low DQE at megavoltage energies is primarily due to the low quantum absorption efficiency - at megavoltage energies only a small fraction of the x-ray beam interacts with the detector and not all of these interacting photons generate measurable signals (see Fig. 5.3). Part of the loss in DQE, however, is due to the excess noise generated by fluctuations in x-ray energy absorption. Figure 5.10(b) shows that the DQE

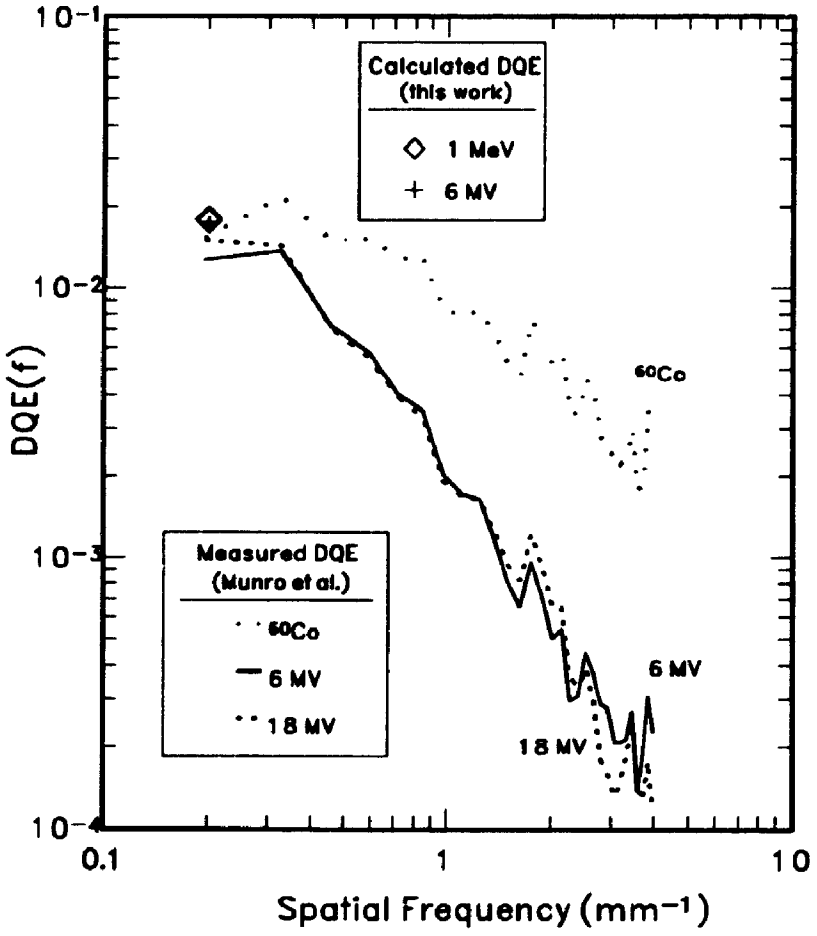

Figure 5.11 Comparison of our zero-frequency estimates of DQE with those reported by Munro et al. The zero-frequency results have been plotted at 0.2 cycles/mm to allow comparison.

calculated for a 1 mm copper plate/1mm phosphor screen is reduced by a factor of 2 by x-ray absorption noise. Clearly, x-ray absorption noise is an important factor in determining the DQE of megavoltage imaging detectors.

5.4.6 Comparison with the literature

Munro et al.[21] report the DQE of a megavoltage imaging system that consists of a copper plate(1 mm)/phosphor screen(400 mg/cm^2) detector and Kodak ortho-M film. They present the DQE as a function of spatial frequency and incident x-ray energy (^{60}Co, 6- and 18-MV). We have modelled the geometry of their detector and generated the AED for both a 1 MeV monoenergetic (~^{60}Co) and a 6 MV polyenergetic x-ray beam. The 6 MV spectrum was taken from the work of Kubsad et al.[22] Since this study does not examine the spatial distribution of the energy deposited in the phosphor layer, our results apply to zero spatial frequency only. Figure 5.11 shows the spatial frequency dependent DQE(f) reported by Munro et al. and the zero-frequency DQE calculated from our Monte Carlo generated AEDs. We have plotted our zero-frequency estimates at 0.2 cycles/mm to allow comparison. The agreement between the measured DQE and our Monte Carlo result is excellent. Munro's results include other sources of noise which are not included in our Monte Carlo estimate of the DQE. These are the influence of variations in light production and transport within the phosphor and film noise. Munro et al. estimate the noise introduced by the film to be only 5% of the total noise power in the system; the other 95% is attributed to x-ray quantum noise, x-ray absorption noise, and, light conversion and transport noise. The excellent agreement between our Monte Carlo results and the experimentally measured results of Munro et al. suggests that the low-

frequency DQE of this system is not influenced significantly by light production and transport within the phosphor.

5.5 Discussion

We have examined the impact of quantum noise and x-ray absorption noise on the DQE of typical fluoroscopic imaging detectors used in megavoltage imaging. The low x-ray interaction cross-sections at megavoltage energies result in low quantum absorption efficiencies. Furthermore, we have shown that x-ray absorption noise becomes a significant source of noise at megavoltage energies, reducing the DQE of typical fluoroscopic detectors by an additional 50%. Since both quantum noise and x-ray absorption noise are intrinsic to the use of these detectors at megavoltage energies, the DQEs reported in this article are the *maximum* DQEs that can be obtained by imaging systems using these detectors.

All of the results presented in this paper have been calculated for monoenergetic x-ray beams (excluding the 6-MV comparison with Munro et al.). One would expect the variance of the AED for a polyenergetic beam to be greater (and hence the statistical factor would be smaller) than that for a monoenergetic x-ray beam. Indeed, this has been demonstrated by Tapiovaara et al.[23] for diagnostic x-ray beams. We have calculated the statistical factor for a 6-MV polyenergetic spectra incident on a 1 mm copper plate/1 mm thick phosphor layer detector to be 0.41. For comparison, the statistical factor for a 2-MeV monoenergetic x-ray beam incident on the same detector is only 0.5. These calculations suggest that the DQE of these detectors, when used with polyenergetic x-ray beams, may be even lower than the results presented here. Clearly, x-ray absorption

noise and the added variance due to a polyenergetic x-ray spectrum can have a significant effect on the performance of portal imaging systems.

Nevertheless, care should be taken not to over interpret our results. Figures 5.9 and 5.10 show that the statistical factors and the DQEs increase as the thickness of the phosphor screen increases. The simple interpretation would be that image quality is best with the thicker detectors. As noted earlier, these results were calculated for zero spatial frequency - the effect of energy spread and light spread on the DQEs have been ignored. Therefore, the results presented here cannot be used on their own to predict an optimal thickness of x-ray detector to be used in portal imaging.

Overall, our results show that the zero-frequency DQE of a 1 mm thick copper plate/ 1 mm thick phosphor screen commonly used in T.V. camera based portal imaging systems is approximately 0.017 for a 6 MV x-ray beam. Current T.V. camera based systems which use such detectors have DQEs much lower (factor of 4) than this because of noise introduced to the image by other noise sources in the system, such as preamplifier noise and secondary quantum (optical) noise.[21] While the development of new optical sensors, such as the amorphous silicon flat panel arrays,[24] will decrease the magnitude of these noise sources dramatically, the DQE of these imaging systems will still not exceed the upper limit imposed by quantum and x-ray absorption noise.

The only way to improve the DQE is to increase the fraction of the incident x-ray fluence that interacts and generates a measurable signal. One approach is to use very thick scintillators.[25,26] The challenge behind these systems is to create a detector where optical spread is minimized even for very thick scintillators. In principle, this should give the ideal situation where increased quantum absorption efficiency does not sacrifice

spatial resolution. However, we believe that while these approaches may be successful, great care will have to be taken in the design of these systems. Imagine an imaging detector similar in thickness to that reported by Morton et al.[25] (25 mm thick $ZnWO_4$ crystals), but, with a pixel size of 1 mm x 1 mm. Thus, the aspect ratio of each detector element is 25:1. For such a detector, the variance in the AED might be very large because of the lateral escape of energy from the detector element. Therefore, the gains in quantum absorption efficiency resulting from the increased thickness may be counteracted by an increase in x-ray absorption noise due to the lateral escape of energy. Therefore, estimating the optimal thickness (aspect ratio) of such a detector will have to consider the effects of x-ray absorption noise.

5.6 Summary and Conclusions

We have used Monte Carlo techniques to estimate the absorbed energy distributions (AED) for phosphor screen and copper plate/phosphor screen imaging detectors. The AEDs have been confirmed with comparison to measured AEDs from non-imaging geometries. The AEDs were found to be extremely dependent on incident x-ray energy and detector geometry. The physical processes responsible for this dependence are also described. The results of our study allow us to draw a number of conclusions.

Because of the low x-ray interaction cross-sections at megavoltage energies, the x-ray quantum absorption efficiency of these detectors is extremely poor (0.1-10%) at megavoltage energies. Furthermore, we have shown that x-ray absorption noise becomes a significant source of noise at megavoltage energies, reducing the DQE by an additional 50%. Our study also illustrates the importance of including secondary particle transport

in determining the quantum absorption efficiency and detector response of multi-layer detectors such as the copper plate/phosphor layer detectors used in megavoltage therapy imaging. Using simple analytical models to estimate the quantum absorption efficiency can result in large inaccuracies, particularly when the range of the charged particles generated within the detector is comparable to the dimensions of the detector. We also find that a metal 'conversion' plate used in conjunction with the phosphor layer can dramatically enhance the quantum absorption efficiency of the phosphor layer at megavoltage x-ray energies. In addition, the copper plate also serves to decrease the amount of x-ray absorption noise.

While our results demonstrate an upper limit on the DQE of imaging systems which use these detectors, a comparison with the DQE of a fluoroscopic imaging system suggests that there is significant room for technical improvement in fluoroscopic imaging systems. Improving the DQE of megavoltage imaging systems beyond the values presented here will require innovations in the design of x-ray imaging detectors.

References

1. R. Swank, "Absorption and noise in x-ray phosphors," J. Appl. Phys., **44**(9) 4199-4203 (1973).

2. R. Swank, "Measurement of absorption and noise in an x-ray image intensifier," J. Appl. Phys., **45**(8), 3673-3678 (1974).

3. H-P. Chan and K. Doi, "Studies of x-ray energy absorption and quantum noise properties of x-ray scareens by use of Monte Carlo simulation," Med. Phys., **11**(1), 37-46 (1984).

4. C.E. Dick and J.W. Motz, "Image information transfer properties of x-ray fluorescent screens," Med. Phys., **8**(3), 337-346 (1981).

5. J.A. Rowlands and K.W. Taylor, "Absorption and noise in cesium iodide x-ray image intensifiers," Med. Phys., **10**(6) 786-795 (1983).

6. A. Ginzburg and C.E. Dick, "Image information transfer properties of x-ray intensifying screens in the energy range from 17 to 320 keV," Med. Phys., **20**(4), 1013-1021 (1993).

7. J.W. Motz and M. Danos, "Image information content and patient exposure," Med. Phys., **5**(1), 8-22 (1978).

8. C.E. Metz and C.J. Vyborny, "Wiener spectral effects of spatial correlation between the sites of characteristic x-ray emission and reabsorption in radiographic screen-film systems," Phys. Med. Biol., **28**(5) 547-564 (1983).

9. **The EGS4 Code System**, W.R. Nelson, H. Hirayama, and D.W.O. Rogers, Stanford Linear Accelerator Center Report, SLAC-265, (1985).

10. D.W.O. Rogers and A.F. Bielajew, "Monte Carlo Techniques of Electron and Photon Transport for Radiation Dosimetry,", Chapter 5 in Vol. III of *The Dosimetry of Ionizing Radiation*, (Academic Press, 1989), p. 481-521.

11. D.W.O. Rogers, "Low energy electron transport with EGS," Nuc. Instr. and Meth., **227**, 165-181 (1989).

12. A.F. Bielajew and D.W.O. Rogers, "PRESTA - The Parameter Reduced Electron-Step Transport Algorithm for Electron Monte Carlo Transport," Nuc. Instr. and Meth., **B18**, 535-548 (1984).

13. C. Malamut, D.W.O. Rogers, and A.F. Bielajew, "Calculation of water/air stopping-power ratios using EGS4 with explicit treatment of electron-positron differences," Med. Phys. **18**(6), 1222-1228 (1991).

14. **Improved bremsstrahlung photon angular sampling in the EGS4 code system**, A.F. Bielajew, R. Mohan, and C-S. Chui, National Research Council of Canada, Division of Physics Report, PIRS-0203, (1989).

15. **Use of ICRU-37/NBS Radiative Stopping Powers on the EGS4 System**, D.W.O. Rogers, S. Duane, A.F. Bielajew, and W.R. Nelson, National Research Council of Canada, Division of Physics Report, PIRS-0177, (1989).

16. **Use of ICRU-37/NBS Collision Stopping Powers on the EGS4 System**, S. Duane, A.F. Bielajew, and D.W.O. Rogers, National Research Council of Canada, Division of Physics Report, PIRS-0173, (1989).

17. D.W.O. Rogers, "More realistic Monte Carlo calculations of photon detector response functions," NIM, **199**, 531-548 (1982).

18. M.J. Berger, S.M. Seltzer, S.E. Chappel, J.C. Humphreys, and J.W. Motz, "Response of silicon detectors to monoenergetic electrons with energies between 0.15 and 5.0 MeV," Nuc. Instr. and Meth. **69**, 181-193 (1969).

19. G. Hall, "Ionisation energy loses of highly relativistic charged particles in thin silicon layers," NIM, **220**, 356-362 (1984).

20. F.H. At · *Introduction to Radiological Physics and Radiation Dosimetry*, (John Wiley & ˛ ons, New York, 1986), p. 5-17.

21. P. Munro, J.A. Rawlinson, and ˙.. Fenster, "Therapy Imaging: A signal-to-noise analysis of fluoroscopic imaging system for radiotherapy localization," Med. Phys., **17**(5), 763-772 (1990).

22. S. Kubsad, R. Mackie, B. Gehring, D. Misisco, B. Puliwal, M. Mehta, and T. Kinsella, "Monte Carlo and Convolution Dosimetry for Stereotactic Radiosurgery," Int. J. Radiat. Oncol. Biol. Phys., **19**, 1027-1035 (1990).

23. M.J. Tapiovaara and R.F. Wagner, "SNR and DQE analysis of broad spectrum imaging," Phys. Med. Biol. **30**(6), 519-529 (1985)

24. L.E. Antonuk, J. Boudry, W. Huang, D.L. MacShan, E.J. Morton, and J. Yorkston, "Demonstration of megavoltage and diagnostic x-ray imaging with hydrogenated amorphous silicon arrays," Med. Phys. **19**(6), 1455-1466 (1992)

25. E.J. Morton, W. Swindell, D.G. Lewis, and P.M. Evans, "A linear array, scintillation crystal-photodiode detector for megavoltage imaging," Med. Phys. **18**(4), 681-691 (1991)

26. H. Roehrig, "High performance, real-time portal imaging," presented at the Second International Workshop on Electronic Portal Imaging, Newport Beach, CA (1991)

6.1 Summary

The purpose of this thesis was to determine the factors which reduce the quality of radiographic images produced with megavoltage energy x-rays. This was achieved by examining several components in the therapy imaging chain: the size and shape of the x-ray source, x-ray interactions within the patient, and finally, x-ray interactions with the x-ray detector.

Our source size investigations revealed two unexpected aspects of radiotherapy radiation sources. In our study of the ^{60}Co source, we found that the small pellets that comprise the source assume a ring-like packing configuration, resulting in a concentric ring pattern in the source distribution. While these sources have been in use throughout the world for over 40 years, this concentric ring packing was unknown to both the manufacturer and the medical physics community. Another interesting observation developed from our study of x-ray sources in medical linear accelerators. While our study of the focal spots of medical linear accelerators was aimed, and succeeded, at determining the influence of the source size on spatial resolution, the results also revealed a large extra-focal source component of the x-ray source. This observation has important implications for radiotherapy. Based on this observation, we propose a novel treatment planning algorithm which is based on a two-source model: a small focal component surrounded by a large extra-focal component. This physical model provides improved estimates of radiation beam penumbra and predicts changes in output with field size and shape; two aspects of radiotherapy treatment planning which are currently separated. The unifying and physical nature of this model makes it extremely attractive to the radiotherapy community.

While our focal spot investigations addressed some of the concerns of spatial resolution, a great deal of the work in this thesis was directed towards noise. The low contrasts at therapeutic energies require that the noise introduced into the image be much lower than that in diagnostic imaging. X-ray scatter can introduce significant amounts of additional noise into the radiographic image. We used Monte Carlo techniques to examine x-ray scatter at megavoltage energies. Our study revealed that while the term "scatter" is accurate at diagnostic energies, changes in interaction cross-sections at megavoltage energies make "scatter-bremsstrahlung-annihilation" a better description. Not only do the components of the scatter fluence change at megavoltage energies, so do their relative energy spectra. Unlike diagnostic beams, the energy spectrum of the scatter fluence generated by a megavoltage beam can be significantly different from the incident spectrum. This shift in energy between the primary and scatter fluences makes the energy response of the imaging detector very important in determining the impact of scatter on image quality.

Another important factor influencing noise in a megavoltage image is the interaction of x rays in the imaging detector. Proper determination of the primary quantum noise requires good estimates of the interacting x-ray fluence. In Chapter 5, we used Monte Carlo techniques to determine the quantum absorption efficiency and x-ray absorption noise for typical phosphor screen x-ray detectors used in therapy imaging. This study demonstrates that simple attenuation estimates of the quantum absorption efficiency of a metal plate/phosphor screen overestimate the quantum absorption efficiency by a factor of 2. Furthermore, such calculations cannot predict the magnitude of x-ray absorption noise. We demonstrate that the additional noise introduced to the

image by variations in x-ray energy absorption reduces the detective quantum efficiency of typical therapy imaging detectors by as much as 50% at megavoltage energies. Clearly, the use of simple models can lead to large inaccuracies in predicting the signal-to-noise of megavoltage images (see Appendix E).

Most of the differences in image quality between the simulator and therapy images shown in Fig. 1.3 are explained by our investigations. We have illustrated that the loss in contrast of the bony anatomy is due to the fall of the photoelectric cross-section. Because of the low atomic number of air, the contrast of air pockets does not decrease as rapidly with increasing x-ray energy, making the air passages of the body more visible in the therapy image. The therapy image also has a noisier appearance than the diagnostic image. We have demonstrated that this lower SNR is the result of many factors including, lower contrasts, lower quantum absorption efficiencies, x-ray scatter, and increased x-ray absorption noise found at megavoltage energies. However, the blurry appearance of the therapy radiograph is not explained by our study of x-ray source sizes (excluding ^{60}Co). We found that the focal spot sizes in modern accelerators should not influence significantly the spatial resolution of therapy images. In addition, it has been shown that the spatial resolving power of the metal plate/portal film detector used to acquire the image in Fig. 1.3b is better than the phosphor screen detectors used to acquire the simulator image.[1] These two factors suggest that the spatial resolution of the therapy and diagnostic images in Fig. 1.3 should have comparable spatial resolution; clearly, this is not the case. This poses the question: "What other factor(s) could be degrading the spatial resolution of the megavoltage image?"

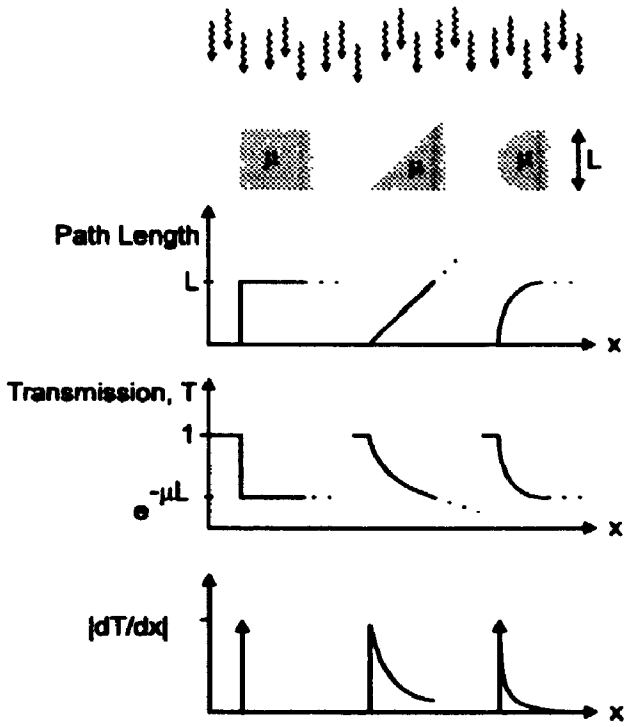

Figure 6.1 Transmission profiles for a step edge, ramp edge and a cylinder edge. The transmission gradient is the first derivative of the transmission profile with respect to x

This question can be answered, at least in part, by examining how the x-ray transmission profile through a bone-like object changes with x-ray energy.

6.2 Transmission gradients and x-ray energy

It can be argued that the most important pieces of information carried by the transmitted x rays is the position of the edge of a structure within the patient. The edges are the most 'spatial frequency rich' structures in an image. It is from these structures that the spatial detail or 'crispness' of an image is judged. Figure 6.1 contains three edge shapes: a step edge, a ramped edge, and the edge of a cylinder. We can use these three simple shapes to illustrate a fundamental dependence of edge detectability on x-ray

energy.

First, consider the step edge. The transmission profile of the step edge is

$$T_s(x) = 0 \qquad x<0$$
$$= e^{-\mu(E)L} \qquad x\geq 0 \qquad (6.1)$$

where μ(E) is the x-ray attenuation coefficient of the edge material and L is the thickness of the step forming object. To examine the frequency content of the edge, we can examine the change of the transmission profile per unit change in position, we refer to this as the *contrast or transmission gradient.* It is the first derivative with respect to x of the transmission profile, $T_s(x)$:

$$\frac{d T_s(x)}{dx} = 0 \qquad 0<x<0$$
$$= -\delta(0) \qquad x=0. \qquad (6.2)$$

As shown in Eq. 6.2, the rate of change of the radiographic edge for a step edge contained within a patient is independent of the attenuation coefficient of the material, and therefore, independent of energy. Now consider the ramp edge. The transmission profile is given by

$$T_r(x) = 0 \qquad x<0$$
$$= e^{-\mu(E)x} \qquad x\geq 0 \qquad (6.3)$$

and the transmission gradient is given by

$$\frac{dT_r(x)}{dx} = 0 \qquad x<0$$
$$= -\mu'(E)e^{-\mu(E)x} \qquad x\geq 0. \qquad (6.4)$$

Unlike the case for the step function, the rate of change of the edge is dependent on the attenuation coefficient of the edge forming material, and therefore, dependent on energy! This simple geometry illustrates how the edge profile and its slope depends on x-ray energy. A more realistic demonstration is to consider the edge of a cylinder which represents a bone. The expression for the transmission profile is given by (Fig. 6.2a):

$$T_c(x) = 0 \qquad x<0$$
$$= e^{-\mu(E)2\sqrt{2xR-x^2}} \qquad x\geq 0 \qquad (6.5)$$

and the transmission gradient is

$$\frac{dT_c(x)}{dx} = 0 \qquad x<0$$
$$= -\delta(0) \qquad x=0$$
$$= -\frac{2\mu(E)(R-x)}{\sqrt{2xR-x^2}} e^{-2\mu(E)\sqrt{2xR-x^2}} \qquad x>0. \qquad (6.6)$$

Like the expression for the ramped edge, this expression is also dependent upon the attenuation coefficient of the object. The dependence alters the shape of the transmission profile across the cylinder edge.

Figure 6.3 illustrates the change in the contrast and shape of the edge of a cylindrical object (2 cm diam, solid cortical bone). The plots shown in Fig. 6.3a demonstrate how the transmission profile of the edge changes with increasing energy, however, the most obvious feature is the change in contrast. By rescaling these curves, such that they all have equal contrast range (Fig. 6.3b), the change in the *shape* of the edge with x-ray energy becomes quite visible. As x-ray energy is increased, the bone edge is "softened" by the lower attenuation coefficients. To illustrate this point further, we have calculated the distance past the edge of the bone at which the attenuation is 90% of its maximum attenuation (X_{90}). The X_{90} value represents the half-width-to-the-maximum of the bone edge (Fig. 6.2b) and is plotted as a function of x-ray energy in Fig. 6.4. The X_{90} values for 30 keV, 100 keV and 2 MeV are 1.3, 5.0, and 5.5 mm for a 20 mm diameter bone cylinder. There is a dramatic change in the position of the X_{90} value at low x-ray energies. These results indicate that the edge of a 20 mm diameter bone goes from

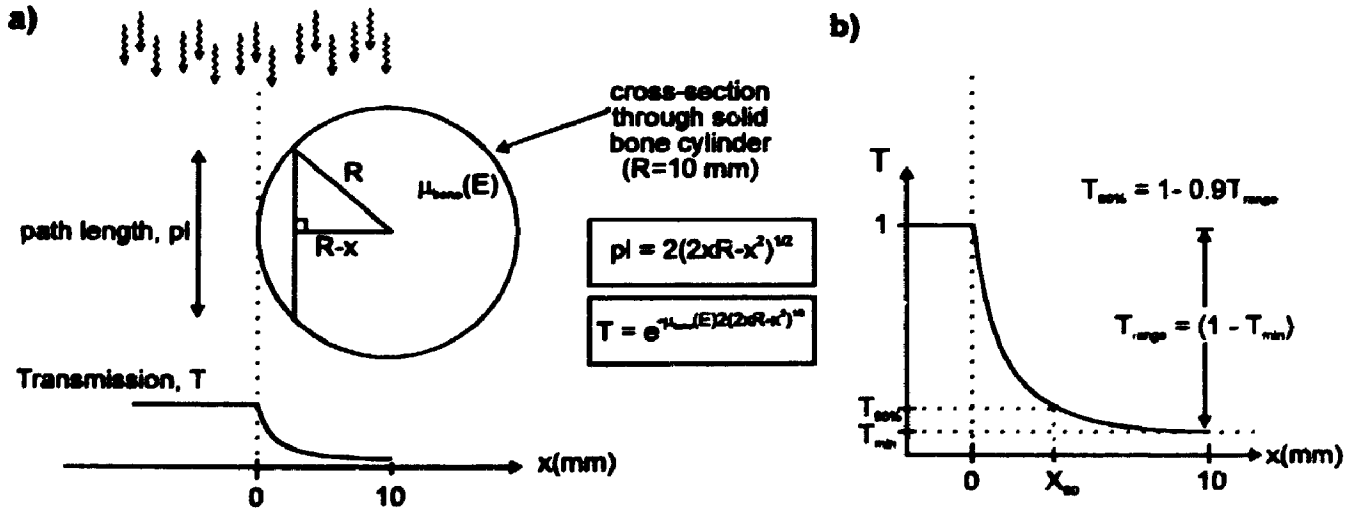

Figure 6.2 The transmission profile of a cylindrical edge. (a) The expression for the transmission profile and (b) a schematic that demonstrates the concept of X_{90}

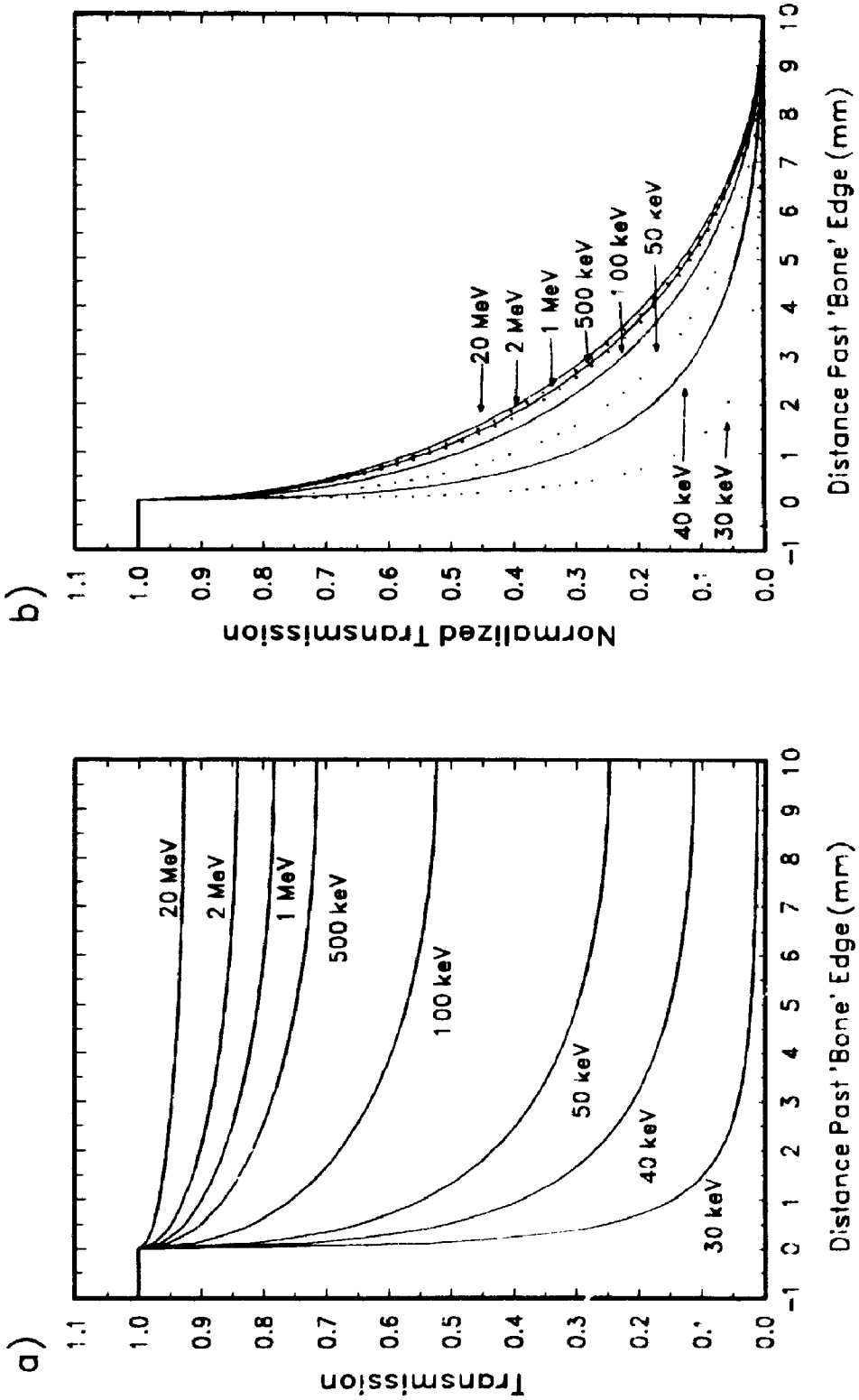

Figure 6.3 (a) The transmission profile across a cylinder edge (bone) (b) Rescaling these profiles to range from 0 to 1 shows how the shape of the transmission profile changes with x-ray energy

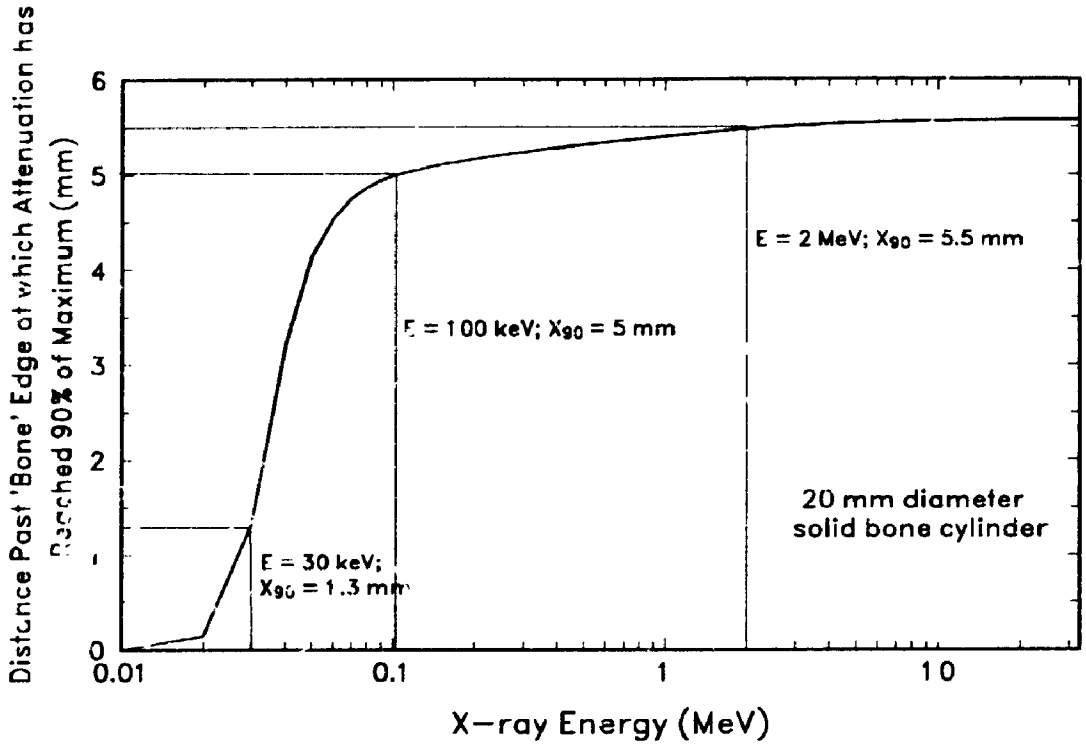

Figure 6.4 X_{90} versus x-ray energy At 30 keV, the bone contrast reachs 90% of maximum within 1 3 mm of the geometric edge This increases to 5.5 mm at 2 MeV.

being 1.3 mm wide at 30 keV, to being over 5 mm wide at energies above 100 keV. From these results, it is expected that the sharpness of bony edges will be significantly reduced at megavoltage energies compared to that at diagnostic energies.

Using this model, we have illustrated that increasing x-ray energy beyond 100 keV introduces a fundamental and intrinsic change in the edge information carried by the transmitted x rays. The example demonstrates how the edge of a bone-like structure can be extended over several millimetres, independent of the x-ray detector used. The distribution of the edge profile will definitely cause a "softening" of the appearance of the edge in the image. We hypothesize that this effect is responsible for the significant reduction in spatial detail observed in the megavoltage radiograph shown in Fig. 1.3b

6.3 Future Work

This thesis has investigated many of the fundamental factors limiting the quality of megavoltage images, in addition, the work presented here has stimulated investigations into other aspects of radiotherapy. The following sections describe some avenues for future work.

6.3.1 Extra-focal source and radiotherapy planning

The study of x-ray sources presented in Chapter 3 reveals the presence of a second, *extra-focal*, x-ray source component in the head of a medical linear accelerator. While the influence of this observation on image quality is minor, it has significant implications for radiotherapy treatment planning. As stated in Chapter 3, we recommend that an improved method of modelling photon dose distributions in radiotherapy could be developed if one uses a two source model consisting of a small focal spot surrounded by a field-size dependent extra-focal component. An algorithm based on this concept is capable of reducing and centralizing many of the steps in the radiotherapy planning process, as well as removing some of the inaccuracies and physical inconsistencies from current empirical practice. There are two major advantages to an algorithm based on this concept.

Firstly, in some dose calculation algorithms, a compromise has to be made in modelling dose profiles for both the large and small field sizes. Arriving at a representative beam profile requires manipulating source parameters to artificial proportions (e.g. source size of several cm's for a linear accelerator). We suspect that a more physical model, which includes an extra-focal component in the x-ray source will

yield a better estimate of the beam profiles at all field sizes. Secondly, it is conventional practice to attribute the change in output (cGy/Monitor Unit) of the accelerator with field size to changes in 'collimator scatter'. We suggest that the change in accelerator output with field size setting is, for the large part, not due to collimator scatter, but rather, due to changes in the fraction of the extra-focal source 'seen' from a point at the isocentre. Using the two-source model, the change in accelerator output with field size is a natural consequence of the model. Therefore, ancillary procedures, such as, measurement of output factors (except for verification) and dose-to-monitor unit conversions could be considerably simplified. In addition, with the arrival of multi-leaf collimation systems, this algorithm would eliminate the task of estimating or measuring output factors for complex field shapes.

6.3 2 Frequency content vs. x-ray energy

As illustrated in the discussion, not only does the contrast information contained within the transmitted x-rays of an x-ray beam vary with x-ray energy, but so does the spatial information. While the simple model described above illustrates this concept, it requires further development. One method of making these concepts more general would be to use the linear systems formalism currently used in imaging system analysis. This would require an examination of the spatial frequencies carried by the x-ray shadowgram. Given the spatial frequencies carried by the shadowgram, the imaging system would be designed to transfer those frequencies. In addition to being of importance in megavoltage imaging, these concepts may play an important role in choosing optimal x-ray energies for diagnostic imaging procedures, such as, angiography.

6.3.3 Single collision energy loss in EGS4

In Chapter 5 a discrepancy was found between the absorbed energy distribution predicted by the EGS4 simulation and the measured results of Berger et al. We hypothesize that this discrepancy is the result of not including single collision energy loss in EGS4. In collaboration with J. McLellan, we have performed the necessary modifications to the EGS4 Monte Carlo code to allow single-collision energy loss. The changes to the EGS4 code resulted in a 5-fold increase in calculation time. This was due to the fact that the single collision energy loss distribution must be sampled for every soft electron collision. These preliminary results are encouraging. The discrepancy in the position of the low-energy peak was reduced by a factor of two with this modification. It is expected that adding a random variability to the number of collision per electron step would further improve agreement between Monte Carlo and measurement.

6.3.4 Verifying field placement with low-energy x-rays

This thesis has demonstrated the many challenges of producing radiographs with megavoltage energy x-rays: very low subject contrasts for bony anatomy; air pockets produce distractingly high contrast signals; a lower SNR than that obtained at diagnostic energies, despite the significantly higher patient doses allowed in therapy imaging; a further reduction in DQE due to the statistical variations in x-ray energy absorption; and the softening of bone edges due to lower attenuation coefficients at megavoltage energies. These factors serve to reduce image quality and hinder the detection of the bony landmarks needed for verification of field placement. Rather than devising methods to combat these problems, several authors have declined the challenge and developed field

placement verification systems which use diagnostic energy x-rays. One method of obtaining diagnostic localisation images is to mount an x-ray tube on the head of the accelerator at a fixed angle to the beam axis.[2] A diagnostic and therapy energy beam are both acquired at the treatment angle - the diagnostic exposure shows the anatomy and the therapy exposure indicates the treatment field. This method has not achieved clinical acceptance largely due to the delay in setup due to movement of the gantry between the diagnostic and therapy imaging exposures.

Ideally, the diagnostic energy x-ray beam would be generated by the accelerator itself, such that the therapy and diagnostic sources are co-positional. Galbraith et al.[3] have pursued the development of such a system and have demonstrated its feasibility. However, the alterations to the accelerator are quite invasive. Clinical implementation of these developments would require the cooperation of the accelerator manufacturer, and little progress has been made in this regard. Investigating other, possibly less invasive, methods of generating low-energy x-rays with a medical linear accelerator may result in the development of a technique which is feasible and attractive to accelerator manufacturers.

Overall, this thesis describes the fundamental factors limiting the quality of megavoltage radiographs and provides an upper bound on the quality of radiographs that can be produced with a megavoltage beam. It is expected that our results will allow the designers of megavoltage imaging systems to identify feasible areas for improvement in their imaging system. By either preventing wasteful attempts at improving the quality of megavoltage images beyond what is physically achievable, or by encouraging alternative

approaches for verifying radiation field placement, the results of our investigations will lead to improvements in field placement verification, and ultimately, improved local tumour control and reduced probability of normal tissue complications.

References

1. P. Munro, J. Rawlinson, and A. Fenster, "Therapy imaging: A signal-to-noise analysis of metal plate/film detectors," Med. Phys. **14**(6), 975-984 (1987)

2. P.J. Biggs, M. Goitein, and M.D. Russell, "A diagnostic x-ray field verification device for a 10 MV linear accelerator," Int. J. Radiat. Oncol. Biol. Phys., **11**, 635-643 (1985)

3. D. M. Galbraith, "Low-energy imaging with high-energy bremsstrahlung beams," Med. Phys., **16**(5), 734-746 (1989)

Appendix A. METHOD OF INCLUDING EXTRA-FOCAL RADIATION IN THE SOURCE MTF

The influence of a broadly distributed extra-focal component on the source MTF is easily calculated if (1) the fraction of the total source strength contained in the focal source, F_{focal}, is known, and (2) it can be shown that the extra-focal source is large enough that it can pass only spatial frequencies well below those of interest (in our case <0.05 mm^{-1}). If these two criteria can be satisfied, the source MTF at the object plane can be shown to be

$$MTF_{source}(f_o) = MTF_{focal}(f_o) \cdot F_{focal} \qquad f_o > 0.05 mm^{-1}. \quad (A.1)$$

This is shown in the following derivation.

Let us consider the case in which the x-ray source of our imaging system can be decomposed into two source distributions, g(r) and h(r). These two distributions are not neccesarily normalized, that is,

$$G = \int_0^\infty g(r) \cdot 2\pi r \cdot dr$$
$$H = \int_0^\infty h(r) \cdot 2\pi r \cdot dr \qquad (A.2)$$

where G and H are the relative intensities of the two source distributions. The line spread function at the object plane for this two-component source is given by the Abel transform of the two source distributions,

$$LSF(x_o) = \int_{|x_d|}^{\infty} \frac{(g(r_o\{\frac{M}{M-1}\}) + h(r_o\{\frac{M}{M-1}\})) \cdot r_o}{(r_o^2 - x_o^2)^{1/2}} \cdot dr_o$$

$$= LSF_g(x_o) + LSF_h(x_o) \qquad (A.3)$$

where M is the radiographic magnification and the distributive property of the Abel transform has been applied. The unnormalized transfer function (OTF) for the entire source is determined by calculating the Fourier transform of these LSFs,

$$OTF_{source}(f_o) = \int_{-\infty}^{\infty} (LSF_g(x_o) + LSF_h(x_o)) \cdot e^{-2\pi i x_o f_o} dx_o$$

$$= \mathcal{F}\{ LSF_g(x_o) \} + \mathcal{F}\{ LSF_h(x_o) \}$$

$$= OTF_g(f_o) + OTF_h(f_o) \qquad (A.4)$$

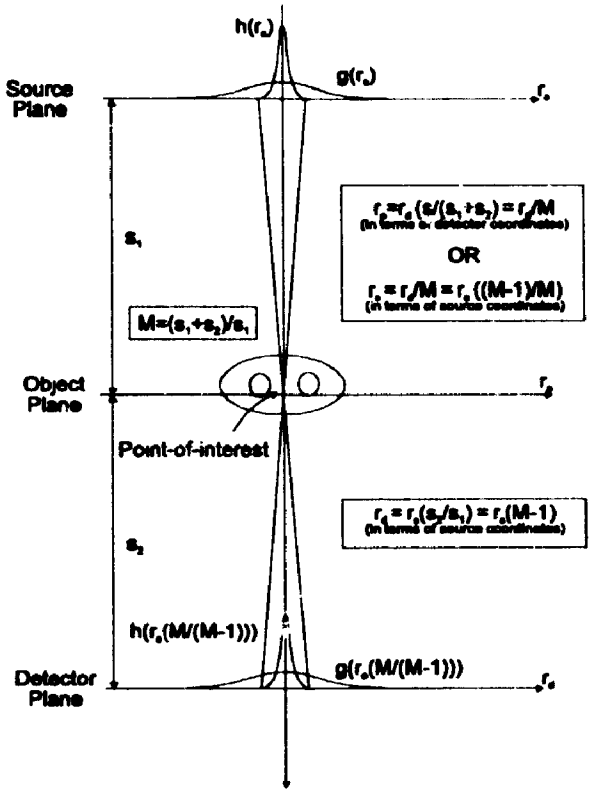

Figure A.1 The scale relation between x-ray source size and blurring at the object plane The x-ray source is projected to the detector plane, then related back to the object plane

where the distributive property of the Fourier transform allows the OTFs of the two components to be separated. The source modulation transfer function (MTF_{source}) is equal the OTF normalized to the area under the total LSF, or equivalently, the zero frequency value of the OTF. Therefore,

$$MTF_{source}(f_o) = \frac{OTF_g(f_o) + OTF_h(f_o)}{OTF_g(0) + OTF_h(0)}. \qquad (A.5)$$

Since the zero-frequency value of the OTF is equal to the area under the LSF for a given source distribution, it is obvious that it is also equal to the volume under the source distribution itself. That is,

$$OTF_g(0) = G \quad and \quad OTF_h(0) = H \qquad (A.6)$$

where G and H are the relative strengths of the two source distributions g(r) and h(r). The source MTF can now be written as

$$MTF_{source}(f_\sigma) = \frac{OTF_g(f_\sigma) + OTF_h(f_\sigma)}{G + H}. \qquad (A.7)$$

This is a general expression for the MTF of a two component source.

Consider the case of an x-ray source which consists of a small focal component (g(r)) surrounded by a large extra-focal component (h(r)), where the focal component has

a source intensity of G and the extra-focal component has a source intensity of H. If it can be shown that the spatial extent of extra-focal source is sufficiently large, such that the $OTF_h(f_o)$ for the extra-focal source falls to zero at the frequencies of interest (>0.05 mm^{-1} in our case), then the expression for the source MTF in Eq. A.7 reduces to:

$$MTF_{source}(f_o) = \frac{OTF_g(f_o)}{G + H} \qquad f_o > 0.05 mm^{-1}. \qquad (A.8)$$

Dividing the numerator and denominator by G results in Eq. A.1,

$$MTF_{source}(f_o) = \frac{\frac{OTF_g(f_o)}{G}}{1 + \frac{H}{G}}$$

$$= MTF_g(f_o) \cdot \frac{G}{G + H}$$

$$= MTF_g(f_o) \cdot F_{focal} \qquad f_o > 0.05 mm^{-1}. \qquad (A.9)$$

where F_{focal} is the fraction of the source strength attributed to the focal component. This expression characterizes the concept of a "low-frequency drop"; the broader distribution does not influence the shape of the source MTF at frequencies above a certain threshold (0.05 mm^{-1} for example), but rather influences the normalization of the source MTF.

Appendix B. INFLUENCE OF SCATTER ON CONTRAST AND DIFFERENTIAL SIGNAL-TO-NOISE FOR A PHOTON COUNTER

In transmission radiography, the x-ray fluence reaching the detector plane consists of photons which have come directly from the radiographic source (primary) and those which have been scattered from their original course (scatter). The influence of these

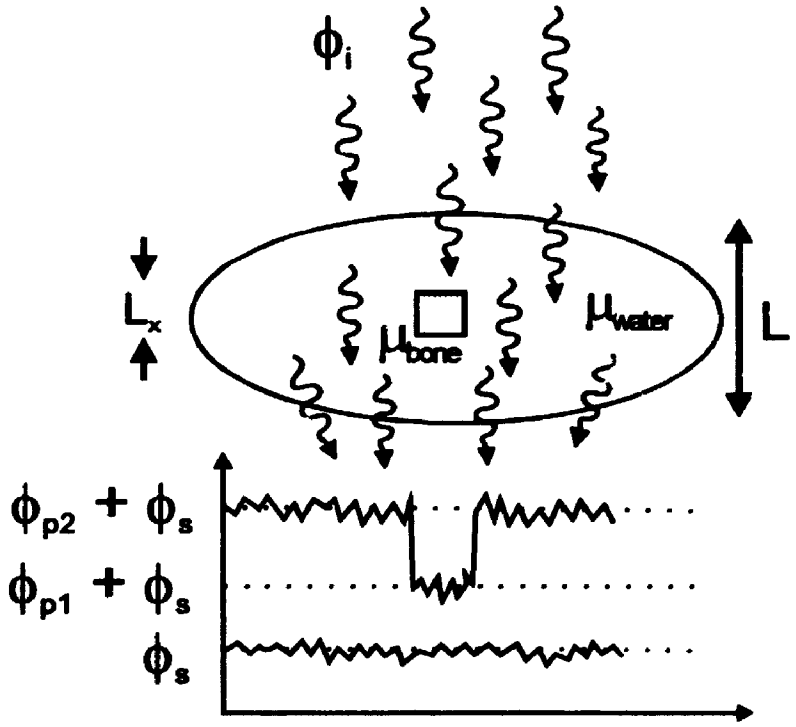

Figure B.1 The detection of a bone object within a water phantom. The scatter fluence reduces contrast and adds noise.

scattered photons on image quality is two-fold. They (1) reduce contrast in imaging systems with fixed display contrast (like film) and (2) reduce the signal-to-noise ratio (SNR) in quantum noise-limited systems.

the detector, and $A_w|_E$ is a correction for the wall of the detector. Since the mass of the detector is constant and the ratio of mass stopping powers vary only slightly (assumed to be constant) over the energy range of interest[20] , they are not important for the final calculations, as they will be cancelled out when the scatter fraction is calculated.

The total response for the ion chamber depends upon two competing effects. The mass energy absorption coefficient represents the fraction of energy deposited in the chamber walls per unit incident energy fluence, which decreases with increasing energy over the range studied here. The wall correction, A_w, accounts for the attenuation (and scattering) of incident photons in the wall/cap of the ion chamber. Its value increases with increasing energy. A_w is calculated using the mass-energy absorption coefficient as an approximation of the broad-beam attenuation coefficient.[21] An estimate of the response of our ionization chamber with a 4 cm diameter PMMA buildup cap is shown in Fig. 4.3b. The coefficients used in calculating the response function are from tabulated data[22].

Employing this estimate of ion chamber (diode) response, the primary and scatter signals were calculated from the Monte Carlo estimated fluences, $\overline{\Phi'(E)}$, using Eq. 4.3. The resulting scatter fractions were calculated as:

$$SF_{signal} = \frac{\overline{Q_s}}{\overline{Q_s} + \overline{Q_p}}. \qquad (4.5)$$

In this way, the scatter fractions calculated using the EGS4 Monte Carlo code could be compared directly with those measured using the ionization chamber and diode.

A simple imaging situation is shown in Fig. B.1. The fluence scatter fraction (Eq. B.1) describes the relative magnitudes of the scatter and primary fluences reaching the detector.

$$SF_{fluence} = \frac{\phi_s}{\phi_s + \phi_p} \qquad (B.1)$$

These fluences are calculated by integrating over the differential fluences,

$$\phi = \int_0^{E_{max}} \phi'(E) \cdot dE, \qquad (B.2)$$

where $\phi'(E)$ is the differential x-ray fluence in units of photons/unit area/unit energy bin width (photon/cm^2/MeV). Contrast is defined by Motz and Danos to be:[1]

$$C = \frac{image\ signal}{carrier\ signal} = \frac{difference}{mean}. \qquad (B.3)$$

In the no-scatter case, the contrast will be

$$C_{ns} = \frac{\phi_{p1} - \phi_{p2}}{(\phi_{p1} + \phi_{p2})/2}. \qquad (B.4)$$

For the case shown in Fig. B.1, with a scatter fluence striking the detector, the contrast will be

$$C_s = \frac{\phi_{p1} - \phi_{p2}}{(\phi_{p1} + \phi_{p2} + 2 \cdot \phi_s)/2}. \qquad (B.5)$$

The ratio of these two expressions shows the loss in contrast in the scatter case,

$$\frac{C_s}{C_{ns}} = \frac{\dfrac{\phi_{p1} - \phi_{p2}}{(\phi_{p1} + \phi_{p2} + 2 \cdot \phi_s)/2}}{\dfrac{\phi_{p1} - \phi_{p2}}{(\phi_{p1} + \phi_{p2})/2}} = \frac{(\phi_{p1} + \phi_{p2})}{(\phi_{p1} + \phi_{p2} + 2 \cdot \phi_s)}. \qquad (B.6)$$

This expression can be simplified if one assumes the contrast is small, that is, $\phi_{p1} \cong \phi_{p2} = \phi_p$. If this is the case, the contrast expression reduces to

$$\frac{C_s}{C_{ns}} = \frac{(2 \cdot \phi_p)}{(2 \cdot \phi_p + 2 \cdot \phi_s)} = \frac{\phi_p}{\phi_p + \phi_s}. \qquad (B.7)$$

The right side of Eq. B.7 is the ratio of primary to total fluence reaching the detector, this

is called the *primary fraction* and is therefore one minus the *scatter fraction*. Therefore, we can right the loss in contrast due to a scatter fluence in terms of the scatter fraction:

$$\frac{C_s}{C_{ns}} = \frac{\phi_p}{\phi_p + \phi_s} = 1 - SF. \qquad (B.8)$$

This expression shows the influence of scatter on contrast. Scatter does not only influence the contrast of objects in an image, it also adds noise to an image, thereby reducing the differential signal-to-noise ratio (DSNR). The DSNR is defined as:[1]

$$DSNR_{ns} = \frac{signal}{noise} = \frac{\phi_{p1} - \phi_{p2}}{\sqrt{(\phi_{p1} + \phi_{p2})}}. \qquad (B.9)$$

The addition of a scatter fluence does not increase the differential signal, but it does increase the noise. Giving an expression for DSNR in the presence of scatter as

$$DSNR_s = \frac{signal}{noise} = \frac{\phi_{p1} - \phi_{p2}}{\sqrt{(\phi_{p1} + \phi_{p2} + 2 \cdot \phi_s)}}. \qquad (B.10)$$

We can express the loss in DSNR due to the presence of scatter by the ratio of these two expressions:

$$\frac{DSNR_s}{DSNR_{ns}} = \frac{\dfrac{\phi_{p1}-\phi_{p2}}{\sqrt{(\phi_{p1}+\phi_{p2}+2\cdot\phi_s)}}}{\dfrac{\phi_{p1}-\phi_{p2}}{\sqrt{(\phi_{p1}+\phi_{p2})}}}$$

$$= \sqrt{\frac{2\cdot\phi_p}{2\cdot\phi_s+2\cdot\phi_p}}$$

$$= \sqrt{1-SF}\,. \qquad (B.12)$$

These two results are a simplification of the real situation because we have assumed that our detector is a photon counter, that is, that each x-ray striking the detector plane is counted equally, regardless of its energy.

References

1. J.W. Motz and M. Danos, "Image information content and patient exposure," Med. Phys., 5(1), 8-22 (1978)

Appendix C. INFLUENCE OF SCATTER ON CONTRAST AND DSNR FOR POLYENERGETIC X-RAY BEAMS AND AN ENERGY DEPENDENT IMAGING DETECTOR

In Appendix B the loss of contrast and reduction in DSNR is shown for a photon counter, in the following section, the loss in contrast and DSNR is shown for a polyenergetic fluence (primary and scatter) incident on a detector with an energy dependent response. In this treatment, the contrasted primary fluences, as well as the scatter fluences, are polyenergetic and are represented by $\phi'_{p1}(E)$,$\phi'_{p2}(E)$ and, $\phi'_{s}(E)$. Conceptually, signal production in the imaging detector by an incident x-ray can be divided into two steps, (1) the likelihood of x-ray interaction, and (2) the amount of signal generated in the detector by such an interaction. Swindell et al.[1] refer to these stages as the effiiciency and responsivity of a detector and shows that the signal, Q, generated by an incident x-ray fluence, $\phi'(E)$, is calculated as

$$Q = A \cdot \int_0^{E_{max}} R(E) \cdot \eta(E) \cdot \phi'(E) \cdot dE, \qquad (C.1)$$

where $\eta(E)$ and $R(E)$ are the efficiency and responsivity of the detector to an incident

x-ray with energy E. The efficiency describes the fraction of incident photons that interact in the detector ($N_{interacting}/N_{incident}$) and the responsivity describes the amount of signal (in arbitary units - Swindell chose Q to be in units of charge in his treatment) produced in the detector per interacting photon. A is the area of the detector element.

From this estimate of signal, we can calculate the contrasts in the scatter and no-scatter cases. The reduction in contrast due to scatter can be written as,

$$\frac{C_s}{C_{ns}} = \frac{\dfrac{Q_{p1}-Q_{p2}}{(Q_{p1}+Q_{p2}+2\cdot Q_s)/2}}{\dfrac{Q_{p1}-Q_{p2}}{(Q_{p1}+Q_{p2})/2}}$$

$$= \frac{(Q_{p1}+Q_{p2})}{(Q_{p1}+Q_{p2}+2\cdot Q_s)}$$

$$= 1 - SF_{signal} \qquad (C.2)$$

where we have defined the ratio of *scatter signal* to *total signal* as the signal scatter fraction, SF_{signal}. This result is identical in form for the result for the photon counter (Appendix B).

The noise associated with a signal, Q, can also be calculated. Assuming the

responsivity of the detector is deterministic, the only source of noise in the imaging process is the quantum noise due to the interacting x-rays. The variance in Q, σ_Q^2, is equal to the sum of the variances in the number of interacting quanta (i.e. the number of interacting x-rays for a Poisson distribution) times the signal per interacting x-ray squared:

$$\sigma_Q^2 = A \cdot \int_0^{E_{max}} R^2(E) \cdot \eta(E) \cdot \phi'(E) \cdot dE. \qquad (C.3)$$

Given the signal and noise (square root of the variance), we can determine the loss in DSNR due to the presence of scattered x-rays. The derivation is shown here:

$$\frac{DSNR_s}{DSNR_{ns}} = \frac{\dfrac{Q_{p1}-Q_{p2}}{\sqrt{(\sigma^2_{Q_{p1}}+\sigma^2_{Q_{p2}}+2\cdot\sigma^2_{Q_s})}}}{\dfrac{Q_{p1}-Q_{p2}}{\sqrt{(\sigma^2_{Q_{p1}}+\sigma^2_{Q_{p2}})}}}$$

$$= \sqrt{\frac{\sigma_p^2}{\sigma_s^2+\sigma_p^2}}$$

$$= \sqrt{1-\frac{\sigma_s^2}{\sigma_s^2+\sigma_p^2}}$$

$$= \sqrt{1-SF_{variance}} \qquad (C.4)$$

OR

$$= \frac{1}{\sqrt{1+\dfrac{\sigma_s^2}{\sigma_p^2}}}$$

$$= \frac{1}{\sqrt{1+SPR_{variance}}}. \qquad (C.5)$$

While these two expressions (C.4 and C.5) appear different from those calculated in the photon counter case (Appendix B, Eq. B.12), they are the same. Equation C.4 is the same as what would be found for the photon counter case, because for a photon counter

$$SF_{variance} = SF_{fluence} = \frac{\phi_s}{\phi_s + \phi_p}. \qquad (C.6)$$

Equation B.12 in Appendix B shows that the loss in DSNR is dependent on the ratio of scatter fluence (or signal) to total fluence (or signal) in the form of the SF, however, the DSNR is actually dependent on the ratio of variance in the scatter signal to the variance in total signal. The result in Appendix B, Eq. B.12 is the result of considering the special case of a photon counter which follows Poisson statistics where the mean signal (fluence) and the variance are identical quantities.

References

1. W. Swindell, E.J. Morton, P.M. Evans, and D.G. Lewis, "The design of megavoltage projection imaging systems: Some theoretical aspects," Med. Phys., **18**(5), 855-866 (1991).

Appendix D. DERIVATION OF THE STATISTICAL FACTOR, I_x

The detective quantum efficiency, DQE, of an imaging system describes that system's ability to transfer signal and noise. The DQE is defined as[1]

$$DQE = \frac{SNR_{out}^2}{SNR_{in}^2} \qquad (D.1)$$

where SNR_{in} and SNR_{out} are the input and output signal-to-noise ratios of the imaging system. To determine how the DQE of an imaging system is influenced by a noisy gain stage, we must examine how the SNR_{out}^2 is influenced by this stage.

In an x-ray transmission radiography imaging system, the SNR_{in} is described by the number of quanta available to an element (pixel) in the imaging system (i.e. incident quanta). Since the number of x-rays, N_o, arriving in an interval of time is Poisson distributed, It can be shown that

$$SNR_{in}^2 = N_o \qquad (D.2)$$

where N_o is the number of quanta incident on a detection element.

Before SNR_{out} can be calculated, the amplification and noise characteristics of the noisy gain stage must be known. For our study of x-ray absorption noise, these characteristics are described fully by the absorbed energy distribution or AED, $(A(E,E_i))$. The AED is a probability distribution which describes the likelihood of an amount of energy, E, being deposited by an incident photon of energy E_i. This distribution is normalized per *incident* photon. Given the AED for the noisy stage, we can determine the output signal-to-noise ratio. The signal, Q, is simply the number of quanta that deposit

E amount of energy multiplied by E and summed over all energies. This can be written as

$$Q = \int_E N_o \cdot A(E,E_i) \cdot E \cdot dE \qquad (D.3)$$

$N_o$is included in this expression because A(E,Ei) is defined to be per incident x-ray. This expression can also be written in terms of the first moment, M_1, of the AED.

$$Q = N_o \cdot M_1. \qquad (D.4)$$

The variance in the signal can be calculated as follows. The number of quanta which have produced a specific energy pulse, E, is equal to $N_oA(E,E_i)$. Assuming Poisson statistics, the variance in this number of quanta is equal to $N_oA(E,E_i)$. Since each energy pulse is of a different magnitude, E, the total variance in the signal, σ_Q^2, will be

$$\sigma_Q^2 = \int_E N_o \cdot A(E,E_i) \cdot E^2 \cdot dE. \qquad (D.5)$$

Like the expression for signal, this expression can be written in terms of the moments of the AED,

$$\sigma_Q^2 = N_o \cdot M_2 \qquad (D.6)$$

where M_2 is the second moment of the AED. Given the signal, Q, and its associated variance, σ_Q^2, we can calculate SNR_{out}^2 for the noisy stage described by the AED:

$$SNR_{out}^2 = \frac{Q^2}{\sigma_Q^2} = \frac{(N_o \cdot M_1)^2}{N_o \cdot M_2}$$
$$= \frac{N_o \cdot M_1^2}{M_2}. \qquad (D.7)$$

Now that we have SNR_{in}^2 and SNR_{out}^2 for this stage we can calculate the DQE,

$$DQE = \frac{SNR_{out}^2}{SNR_{in}^2}$$
$$= \frac{(N_o \cdot M_1^2 / M_2)}{N_o}$$
$$= \frac{M_1^2}{M_2} \qquad (D.8)$$

Comparatively, we can examine a perfect system which counts each x-ray quanta equally (no variations in gain). The DQE for such a system would be

$$DQE_{count} = \epsilon \qquad (D.9)$$

where ϵ is the quantum efficiency of the detector (the detective quantum efficiency becomes equivalent to the quantum efficiency in this case). We can calculate the relative loss in DQE by the noisy stage by taking the ratio of the true DQE to the ideal DQE,

$$\frac{DQE}{DQE_{count}} = \frac{M_1^2/M_2}{\epsilon} = \frac{1}{\epsilon}\cdot\frac{M_1^2}{M_2}. \qquad (D.10)$$

This can be written more elegantly if one recognizes that ϵ is the zeroth moment of $A(E,E_i)$,

$$\epsilon = M_o = \int_E A(E,E_i)\cdot dE. \qquad (D.11)$$

We define the statistical factor, I_x, to represent the loss in DQE due to the noisy gain stage. Therefore, the statistical factor can be written as

$$I_x = \frac{DQE}{DQE_{ideal}} = \frac{M_1^2}{M_2\cdot M_0}. \qquad (D.12)$$

This is the expression for I_x used in Chapter 5. This is also the expression described by Swank in his first article on absorption noise.[2] The statistical factor is often referred to as

the Swank factor.

References

1. J.W. Motz and M. Danos, "Image information content and patient exposure," Med. Phys., 5(1), 8-22 (1978).

2. R. Swank, "Absorption and noise in x-ray phosphors," J. Appl. Phys., 44(9) 4199-4203 (1973).

Appendix E. IMPROVED ESTIMATES OF THE SIGNAL-TO-NOISE RATIO

The investigations in chapters 4 and 5 yielded improved estimates of quantum absorption efficiency, demonstrated the importance of x-ray absorption noise, and provided realistic estimates of x-ray scatter at megavoltage energies. All these factors influence the simple SNR calculations presented in Chapter 1. In the following section the SNR calculations are revisited to include the findings of chapters 4 and 5.

As shown in Chapter 1, the reduction in the photoelectric cross-section at megavoltage energies significantly reduces the contrast of bony structures. Detection of low contrast objects requires that *all sources of noise* in the imaging system be kept to a minimum. As we have demonstrated in the previous chapters, there are several noise sources in megavoltage imaging. These include, among others, primary quantum noise, x-ray scatter quantum noise, and x-ray absorption noise.

Primary x-ray quantum noise results from the stochastic nature of x-ray detection. The random variation in the number of detected x-rays in a given collection interval produces noise in the image signal. The noise in the number of x-rays detected is the square root of the number of detected x-rays. Therefore, the primary quantum noise is dependent on the number of x-rays which pass through the patient and reach a detector element and the quantum absorption efficiency of that element. As described in Chapter 1, we have determined the typical number of x-rays used to form diagnostic and therapy images. However, the estimates of quantum absorption efficiency were based on a simple model, which did not include the influence of secondary particle transport within the detector. Chapter 5 presents Monte Carlo estimates of the quantum absorption efficiencies for typical therapy imaging detectors and demonstrates the inaccuracies

resulting from calculating the quantum absorption efficiency of a Cu plate/phosphor screen x-ray detector without including the influence of charged particle transport. Our estimate of the quantum absorption efficiency used in the introduction was based on x-ray attenuation in a 0.5 mm thick gadolinium oxysulfide (Gd_2O_2S) phosphor layer and was estimated to be 0.015 for 2 MeV x rays. Our Monte Carlo study of a more realistic x-ray detector, consisting of a 1 mm Cu plate and a 1 mm thick phosphor layer, determined a quantum absorption efficiency of 0.025. The higher value for the copper/phosphor x-ray detector is largely the result of including secondary particles, such as knock-on electrons, in our Monte Carlo calculations. Secondary particles exiting the Cu plate can deposit energy in the phosphor layer and thus increase the efficiency. Since the SNR is proportional to the square root of the number of detected quanta, increasing the quantum absorption efficiency from 0.015 to 0.025 increases the SNR by a factor of $\sqrt{(0.025/0.015)} = 1.3$. The SNR for the therapy imaging case has been recalculated using this improved estimate (see Table E.1).

Scattered x-rays that interact in the detector also contribute quantum noise. Our study of x-ray scatter at megavoltage energies has shown that the scatter fraction decreases with increasing x-ray energy. For example, the scatter fraction for a 30 cm x 30 cm field of 2 MeV x rays incident on a 20 cm thick slab of water and no air-gap is approximately 0.55 (i.e. 55% of the fluence reaching the detector has been scattered). Comparatively, for the same geometry, a diagnostic energy (50-100 keV) x-ray beam produces a scatter fraction of approximately 0.8-0.9. Excluding the use of anti-scatter grids, these scatter fractions reduce the SNR by 0.67 and 0.38, for the therapy and diagnostic cases, respectively. These factors have also been applied to our estimates of

SNR found in Table E.1.

X-ray absorption noise is another source of noise which can reduce the visibility of low contrast objects in an image. This source of noise results from using an energy detector, such as a phosphor screen, to detect the x-rays. Since the transmitted x-ray fluence is recorded by scoring the energy deposited in the detector by the interacting x rays, any variation in the amount of energy deposited by an x ray will introduce noise into the image. Our study of megavoltage x-ray interactions within typical (energy scoring) therapy imaging detectors has demonstrated a large variability in the fraction of energy deposited by an interacting x ray. The reduction in detective quantum efficiency (DQE) due to this additional noise source is represented by the statistical factor, I_x. We have shown that I_x falls from approximately 0.97 at 50 keV for a thin diagnostic screen[1] to 0.61 at 2 MeV for the 1 mm Cu plate/1 mm phosphor screen commonly used in therapy

SNR	X-ray Energy and Patient Dose			
	50 keV	2 MeV		
	0.05 cGy (50 mR)	1 cGy	10 cGy	55 cGy
result from simple model (see introduction)	71	4 8	15	35
with Monte Carlo estimate of the QAE	71	6 2	19	45
with x-ray absorption noise	70	4.8	15	35
with x-ray scatter	26	3 2	10	23

Table E.1 Improved estimates of the SNR for diagnostic and therapy imaging exposures We now include Monte Carlo estimates of the quantum absorption efficiency, the statistical factor, and x-ray scatter.

imaging. Since the SNR is proportional to the square root of I_x, this effect reduces the SNR by a factor of 0.99 and 0.78 for the diagnostic and therapy cases, respectively (see Table E.1). Clearly, this effect is more pronounced for megavoltage x-ray detection.

Considering these improved estimates of primary quantum noise, x-ray scatter noise, and x-ray absorption noise, we now have better estimates of the relative SNRs found in therapy and diagnostic images. The revised estimates of SNR are summarized in Table E.1. Considering these additional factors, the SNR for a therapy image produced with 10 cGy is almost three times lower than that for a diagnostic image produced with 0.05 cGy. This is an improvement over what was determined in Chapter 1 (five times lower). To maintain the same SNR as that found for the diagnostic beam, we have determined that a dose of greater than 55 cGy would be required. Unfortunately, such a dose is a very large fraction of the total dose to be delivered in a single daily treatment.

While we have considered some of the noise sources intrinsic to megavoltage transmission radiography, there are other sources of noise in the imaging system which make detection of the low-contrast bone signals difficult. In comparison to a diagostic energy imaging system, extra care must be taken to reduce all other sources of noise when designing a megavoltage imaging system. This requires: careful selection of imaging system components (preamplifiers, digitizer),[2] such that excessive quantities of noise are not injected into the image signal; maximizing the display contrast of the therapy image such that the noise in the human visual system does not reduce the visibility of low-contrast structures;[3] and finally, care must be taken to minimize the noise introduced into the image signal by secondary quantum statistics (optical quantum noise, for example).[2]

References

1. H-P. Chan and K. Doi, "Studies of x-ray energy absorption and quantum noise properties of x-ray screens by use of Monte Carlo simulation," Med. Phys., 11(1), 37-46 (1984).

2. J-.P. Bissonnette, D.A. Jaffray, A. Fenster, and P. Munro, "Optimal radiographic magnification for portal imaging," submitted to Med. Phys.

3. J.W. Motz and M. Danos, "Image information content and patient exposure," Med. Phys., 5(1), 8-22 (1978).